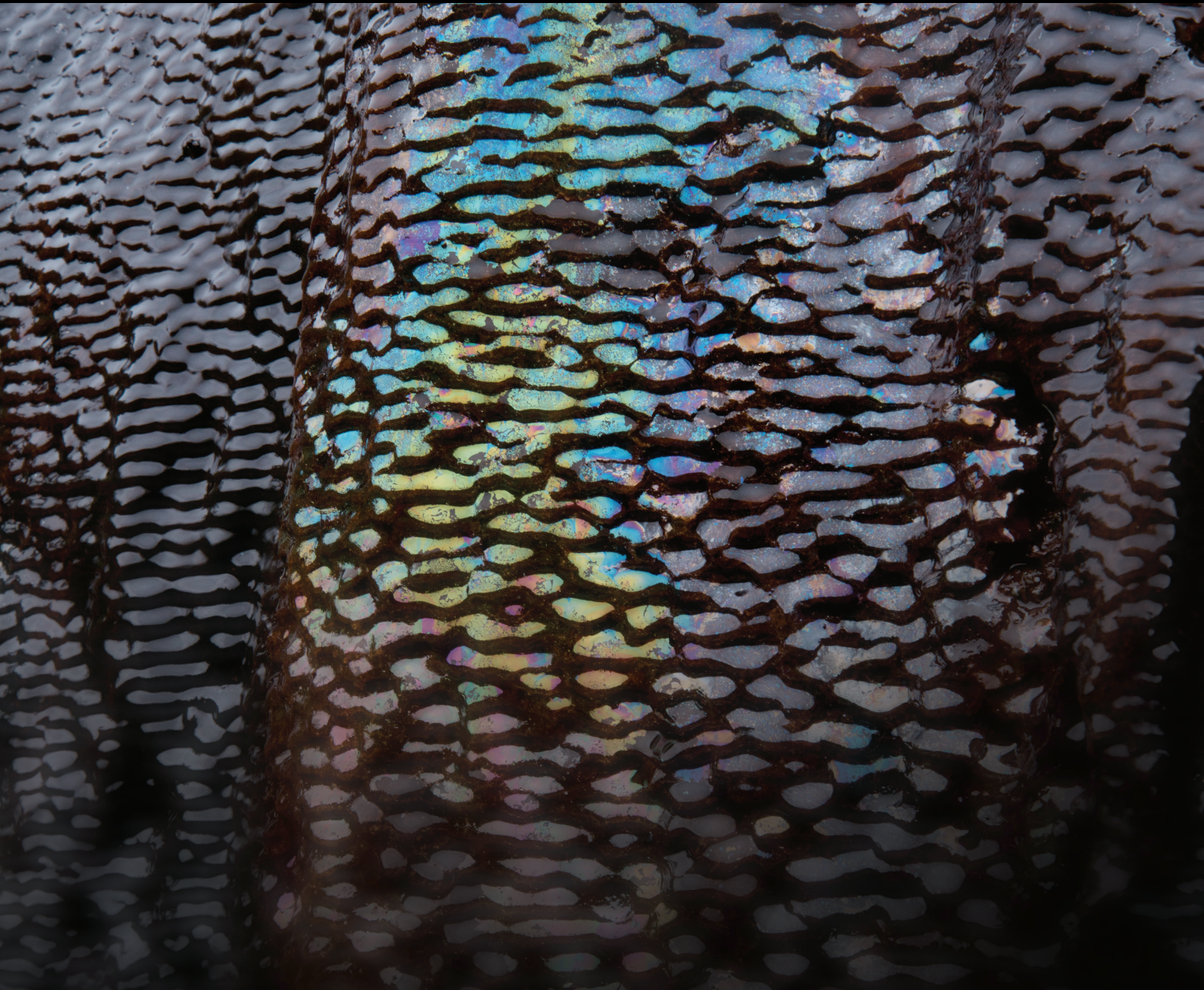


Petrophysics and Fluid Transport in Shales and Tight Reservoirs

Lead Guest Editor: Feng Yang

Guest Editors: Xiaohu Dong, Alexandra Amann-Hildenbrand, Ebrahim Fathi,
and Derek Elsworth





Petrophysics and Fluid Transport in Shales and Tight Reservoirs

Geofluids

Petrophysics and Fluid Transport in Shales and Tight Reservoirs

Lead Guest Editor: Feng Yang

Guest Editors: Xiaohu Dong, Alexandra Amann-Hildenbrand,
Ebrahim Fathi, and Derek Elsworth



Copyright © 2018 Hindawi. All rights reserved.

This is a special issue published in "Geofluids." All articles are open access articles distributed under the Creative Commons Attribution License, which permits unrestricted use, distribution, and reproduction in any medium, provided the original work is properly cited.

Editorial Board

Carmine Apollaro, Italy
Baojun Bai, USA
Maurizio Barbieri, Italy
Julien Bourdet, Australia
Andrea Brogi, Italy
David A. Butterfield, USA
Mauro Cacace, Germany
Isabelle Chambefort, New Zealand
Shengnan Nancy Chen, Canada
Paola Cianfarra, Italy
Daniele Cinti, Italy
Timothy S. Collett, USA
Nicoló Colombani, Italy
Mercè Corbella, Spain
Carlos R. De Souza Filho, Brazil
Henrik Drake, Sweden
Lionel Esteban, Australia
Cinzia Federico, Italy
Tobias P. Fischer, USA
Paulo Fonseca, Portugal
Francesco Frondini, Italy

Paolo Fulignati, Italy
Paola Gattinoni, Italy
Salvatore Inguaggiato, Italy
Francesco Italiano, Italy
Jaewon Jang, Republic of Korea
Luchao Jin, USA
Shinsuke Kawagucci, Japan
Karsten Kroeger, New Zealand
Cornelius Langenbruch, USA
Huazhou Li, Canada
Stefano Lo Russo, Italy
Constantinos Loupasakis, Greece
Lin Ma, USA
Paolo Madonia, Italy
Fabien Magri, Germany
Andrew H. Manning, USA
Micòl Mastrocicco, Italy
Lucie Mathieu, Canada
John A. Mavrogenes, Australia
Agnes Mazot, New Zealand
Jean-Luc Michelot, France

Ferenc Molnar, Finland
Julie K. Pearce, Australia
Daniele Pedretti, Finland
Marco Petitta, Italy
Christophe Renac, France
Reza Rezaee, Australia
Ali Saeedi, Australia
Mohammad Sarmadivaleh, Australia
Christian Siebert, Germany
Ricardo L. Silva, Canada
Ondra Sracek, Czech Republic
Andri Stefansson, Iceland
Richard E. Swarbrick, UK
Pietro Teatini, Italy
Svetlana G. Tessalina, Australia
Rene Therrien, Canada
Umberta Tinivella, Italy
Tivadar M. Tóth, Hungary
Zhenjiang You, Australia
Keni Zhang, China
Ling-Li Zhou, Ireland

Contents

Petrophysics and Fluid Transport in Shales and Tight Reservoirs

Feng Yang , Xiaohu Dong, Alexandra Amann-Hildenbrand, Ebrahim Fathi, and Derek Elsworth
Editorial (3 pages), Article ID 5691953, Volume 2018 (2018)

Apparent Permeability Model for Shale Gas Reservoirs Considering Multiple Transport Mechanisms

Shijun Huang , Yonghui Wu, Linsong Cheng, Hongjun Liu, Yongchao Xue, and Guanyang Ding
Research Article (18 pages), Article ID 2186194, Volume 2018 (2018)

A Mathematical Pressure Transient Analysis Model for Multiple Fractured Horizontal Wells in Shale Gas Reservoirs

Yan Zeng , Qing Wang , Zhengfu Ning, and Hongliang Sun
Research Article (16 pages), Article ID 8065949, Volume 2018 (2018)

Theoretical Modeling of Dielectric Properties of Artificial Shales

Tongcheng Han , Roman Beloborodov , Marina Pervukhina, Matthew Josh, Yanlin Cui, and Pengyao Zhi
Research Article (12 pages), Article ID 2973181, Volume 2018 (2018)

Experimental Characterization of Dielectric Properties in Fluid Saturated Artificial Shales

Roman Beloborodov, Marina Pervukhina, Tongcheng Han, and Matthew Josh
Research Article (8 pages), Article ID 1019461, Volume 2017 (2018)

Impact of Petrophysical Properties on Hydraulic Fracturing and Development in Tight Volcanic Gas Reservoirs

Yinghao Shen, Mianmo Meng, Tao Liu, Hongkui Ge, and Yuelei Zhang
Research Article (13 pages), Article ID 5235140, Volume 2017 (2018)

A Semianalytical Model for Multiple-Fractured Horizontal Wells with SRV in Tight Oil Reservoirs

Jiahang Wang, Xiaodong Wang, and Wenxiu Dong
Research Article (15 pages), Article ID 2632896, Volume 2017 (2018)

Editorial

Petrophysics and Fluid Transport in Shales and Tight Reservoirs

Feng Yang ¹, Xiaohu Dong,² Alexandra Amann-Hildenbrand,³ Ebrahim Fathi,⁴
and Derek Elsworth⁵

¹China University of Geosciences, Wuhan, China

²China University of Petroleum, Beijing, China

³RWTH Aachen University, Aachen, Germany

⁴West Virginia University, Morgantown, WV, USA

⁵Pennsylvania State University, University Park, PA, USA

Correspondence should be addressed to Feng Yang; fengyang@cug.edu.cn

Received 21 May 2018; Accepted 23 May 2018; Published 5 August 2018

Copyright © 2018 Feng Yang et al. This is an open access article distributed under the Creative Commons Attribution License, which permits unrestricted use, distribution, and reproduction in any medium, provided the original work is properly cited.

1. Motivation and Background

The development of horizontal drilling and hydraulic fracturing has enabled the extraction of hydrocarbons from fine-grained sedimentary rocks. This type of unconventional resource has gained much attention for most oil companies all over the world. Understanding petrophysics and the gas-water-rock interactions is essential in guaranteeing the effective recovery of hydrocarbons from shale and other tight reservoirs. But shales and tight rocks are commonly highly heterogeneous with behaviors tiered in multiple scales [1, 2]. Also, within the reservoir, the coexistence of micro-/nanopores and natural/hydraulic fractures further enhances the complexity of storage and transport spaces [3, 4]. During the last decade, the development of effective experimental and numerical methods to explore the petrophysics in shale and tight reservoirs has become a top priority for the exploitation of shale and tight reservoirs.

Fluid transport in such complex media cannot be easily determined with conventional techniques, which are successfully applied for reservoir rocks. At micro-/nanoscales, the interplay between fluids and the pore wall is no longer negligible. The mechanisms of diffusion, slip flow, and sorption all significantly affect the transport of geofluids [5, 6]. Moreover, such small diameter storage and transport

pores/fractures enhance the effect of pore confinement on the phase behavior of fluids [7, 8]. The bubble point pressure and phase envelop of reservoir fluids are changed. The focus of this special issue is therefore placed on an improved understanding of the phase behavior of geofluids, fluid transport mechanisms, and non-Darcy effects in nanopores of shales and other tight rocks. The purpose of this special issue is to collate high-quality research articles in petrophysics and fluid transport in unconventional reservoirs. The special issue addresses the most recent advances in physical experiments and numerical simulation techniques to study the petrophysics and gas-water-rock interactions of unconventional reservoirs across broad length and time scales.

2. Contents of the Special Issue

2.1. Dielectric Properties of Fine-Grained Sedimentary Rocks. As contemporary petroleum exploration activities have focused on unconventional resources, the traditional experimental methods and numerical simulation tools are sometimes no longer effective. We confront numerous challenges to accurately describe the petrophysics of fine-grained sedimentary rocks in unconventional tight and shale reservoirs.

R. Beloborodov et al. experimentally characterize the dielectric properties of fluid-saturated artificial shales.

Because of the high dielectric contrast between water and hydrocarbons, the producible layers of reservoir rocks and surrounding media can be effectively distinguished. In this paper, the authors investigate the frequency-dependent dielectric properties of artificial shale rocks prepared from silt-clay mixtures via mechanical compaction.

T. Han et al. present a theoretical model for the anisotropic dielectric properties of artificial shales. Their model is based on the theoretical assumption of differential effective medium models for any number of mineral grain components aligned in any directions and is shown to be independent of the mixing order. By incorporating a measured orientation distribution function of the clay particles and by inverting the dielectric properties of the artificial sample composed of clay and brine, their model is capable of modeling the frequency-dependent anisotropic dielectric properties of artificial shales.

2.2. Fluid Transport in Shales and Tight Reservoirs. Gas shales and tight reservoirs exhibit extremely low permeability. This low permeability makes it difficult to apply traditional transport modeling approaches, such as Darcy's law, to shales [9, 10]. Gas flow in organic matter, natural fractures, and hydraulic fractures occurs via different mechanisms: continuum flow, slip flow, and Knudsen diffusion. Adsorbed gas desorption from the organic matter also plays a role in gas transport [11]. It is challenging to develop a comprehensive model to describe the multiple mechanisms in the gas transport process.

S. Huang et al. proposed a comprehensive apparent permeability model to consider the multiple transport mechanisms in shale gas reservoirs. The specific mechanisms include viscous flow, slip flow, Knudsen diffusion, and surface diffusion. In their model, the pore diameter and mean free path of gas molecules are corrected by considering the adsorption layer and dense gas effect.

Y. Zeng et al. develop a modified apparent permeability model to describe gas flow in shale gas reservoirs. The apparent model integrates viscous flow, Knudsen diffusion, and gas desorption. They additionally consider a macroseepage model of multistage fractured horizontal wells accommodating multiple gas flow mechanisms to predict the dynamic pressure and production performance.

Hydrocarbon extraction from tight reservoirs is feasible using multiple-fractured horizontal wells. The technology to create multiple-fractured horizontal wells creates a complex stimulated reservoir volume (SRV) with induced fractures proximal to the hydraulic fractures. J. Wang et al. focus on the geometric properties of this stimulated reservoir volume in tight reservoirs and develop a new semianalytical model to analyze the well bottom pressure response. The calculations are helpful to understand the dynamic characteristics of multiple-fractured horizontal wells and the performance of the stimulated reservoir volume.

Hydraulic fracturing is one of the key methods for the effective development of unconventional reservoirs. In the process of hydraulic fracturing, a significant volume of fracturing fluid is injected into the reservoir. However, much of this fracturing fluid is retained in the formation after

flow-back [12]. Y. Shen et al. study the aqueous phase trapping phenomenon in volcanic reservoirs. Nuclear magnetic resonance (NMR) and pulse-decay permeability techniques are employed to monitor the spontaneous imbibition of the fracturing fluid. This work improves our understanding of transport mechanisms of hydraulic fracturing fluids in unconventional reservoirs.

Acknowledgments

We appreciate the significant contributions of the various authors to this special issue and their perseverance during the publication process. We also thank the many anonymous reviewers who helped evaluate and contribute to these papers.

Feng Yang
Xiaohu Dong
Alexandra Amann-Hildenbrand
Ebrahim Fathi
Derek Elsworth

References

- [1] J. B. Curtis, "Fractured shale-gas systems," *AAPG Bulletin*, vol. 86, no. 11, pp. 1921–1938, 2002.
- [2] F. Yang, Z. Ning, Q. Wang, R. Zhang, and B. M. Krooss, "Pore structure characteristics of lower Silurian shales in the southern Sichuan Basin, China: insights to pore development and gas storage mechanism," *International Journal of Coal Geology*, vol. 156, pp. 12–24, 2016.
- [3] A. Amann-Hildenbrand, A. Ghanizadeh, and B. M. Krooss, "Transport properties of unconventional gas systems," *Marine and Petroleum Geology*, vol. 31, no. 1, pp. 90–99, 2012.
- [4] Y. Gensterblum, A. Ghanizadeh, R. J. Cuss et al., "Gas transport and storage capacity in shale gas reservoirs – a review. Part A: transport processes," *Journal of Unconventional Oil and Gas Resources*, vol. 12, pp. 87–122, 2015.
- [5] I. Y. Akkutlu and E. Fathi, "Multiscale gas transport in shales with local kerogen heterogeneities," *SPE Journal*, vol. 17, no. 4, pp. 1002–1011, 2012.
- [6] E. Fathi and I. Y. Akkutlu, "Matrix heterogeneity effects on gas transport and adsorption in coalbed and shale gas reservoirs," *Transport in Porous Media*, vol. 80, no. 2, pp. 281–304, 2009.
- [7] X. Dong, H. Liu, J. Hou, K. Wu, and Z. Chen, "Phase equilibria of confined fluids in nanopores of tight and shale rocks considering the effect of capillary pressure and adsorption film," *Industrial & Engineering Chemistry Research*, vol. 55, no. 3, pp. 798–811, 2016.
- [8] X. Dong, H. Liu, W. Guo, J. Hou, Z. Chen, and K. Wu, "Study of the confined behavior of hydrocarbons in organic nanopores by the potential theory," *Fluid Phase Equilibria*, vol. 429, pp. 214–226, 2016.
- [9] K. Fan, M. Dong, D. Elsworth, Y. Li, C. Yin, and Y. Li, "A dynamic-pulse pseudo-pressure method to determine shale matrix permeability at representative reservoir conditions," *International Journal of Coal Geology*, vol. 193, pp. 61–72, 2018.
- [10] X. Cui, A. M. M. Bustin, and R. M. Bustin, "Measurements of gas permeability and diffusivity of tight reservoir rocks:

different approaches and their applications,” *Geofluids*, vol. 9, no. 3, 223 pages, 2009.

- [11] K. Wu, X. Li, C. Wang, W. Yu, and Z. Chen, “Model for surface diffusion of adsorbed gas in nanopores of shale gas reservoirs,” *Industrial & Engineering Chemistry Research*, vol. 54, no. 12, pp. 3225–3236, 2015.
- [12] J. Wang, D. Elsworth, and M. K. Denison, “Hydraulic fracturing with leakoff in a pressure-sensitive dual porosity medium,” *International Journal of Rock Mechanics and Mining Sciences*, vol. 107, pp. 55–68, 2018.

Research Article

Apparent Permeability Model for Shale Gas Reservoirs Considering Multiple Transport Mechanisms

Shijun Huang , Yonghui Wu, Linsong Cheng, Hongjun Liu, Yongchao Xue, and Guanyang Ding

College of Petroleum Engineering, China University of Petroleum, Beijing 102249, China

Correspondence should be addressed to Shijun Huang; hshj@cup.edu.cn

Received 11 April 2017; Revised 1 June 2017; Accepted 12 March 2018; Published 4 June 2018

Academic Editor: Alexandra Amann-Hildenbrand

Copyright © 2018 Shijun Huang et al. This is an open access article distributed under the Creative Commons Attribution License, which permits unrestricted use, distribution, and reproduction in any medium, provided the original work is properly cited.

Shale formation is featured in nanopores and much gas adsorptions. Gas flow in the shale matrix is not a singular viscous flow, but a combination of multiple mechanisms. Much work has been carried out to analyze apparent permeability of shale, but little attention has been paid to the effect of unique gas behavior in nanopores at high pressure and adsorbed layer on apparent permeability. This work presents a new model considering multiple transport mechanisms including viscous flow (without slip), slip flow, Knudsen diffusion, and surface diffusion in the adsorption layer. Pore diameter and mean free path of gas molecules are corrected by considering the adsorption layer and dense gas effect, respectively. Then the effects of desorption layer, surface diffusion, and gas behavior on gas apparent permeability in nanopores of shale are analyzed. The results show that surface diffusion is the dominant flow mechanism in pores with small diameter at low pressure and that the effect of adsorbed layer and dense gas on apparent permeability is strongly affected by pressure and pore diameter. From the analysis results, the permeability value calculated with the new apparent permeability model is lower than in the other model under high pressure and higher than in the other model under low pressure, so the gas production calculated using the new permeability model will be lower than using the other model at early stage and higher than using the other model at late stage.

1. Introduction

Much attention has been paid to shale due to the considerable volume of natural gas trapped in it. Over the past decades, technology advances in horizontal drilling and hydraulic fracturing have enabled profitable production of shale gas. However, because of the unique deposit character and flow mechanisms of shale gas, controversy still exists on how much gas can be produced from shale [1].

Compared with conventional reservoirs, shales are characterized with pores between 1 and 100 nm, of which the dominant diameter is in nanoscale [2], making it difficult to get accurate shale permeability. Both experimental methods and theoretical methods were proposed to solve the problem. Due to overlarge time consumption, constant-pressure steady-state-flow measurement is not applicable to shale [3]. As a result, other approaches such as TED [4] and crushed rock method [5] were commonly adopted. However,

flow regimes could not be well characterized with experimental methods. Therefore, different theoretical models were proposed to investigate gas flow behavior in shale, among which apparent permeability models are the most prevailing and can be divided into two categories. The first category is correcting intrinsic permeability with a function of Knudsen number. Empirical parameters are included in most of the models, and gas flow regimes (viscous flow, slip flow, transition flow, and Knudsen diffusion) in a single capillary are classified based on Knudsen number and viscous flow slip flow and diffusion are mutually exclusive. Beskok and Karniadakis [6] conducted many experiments and presented a correction factor, and Florence et al. [7] simplified the correction factor. Many other correlations are also provided in apparent gas permeability in tight porous media [8–11]. The second category is weighted models, in which flow and diffusion are not mutually exclusive and their weight in apparent permeability is different at different Knudsen

numbers. When the Knudsen number is small, collision between gas molecules is dominant and gas flow is characterized by viscous flow and slip flow. When the Knudsen number is large, however, collision between gas molecules and the pore surface becomes dominant and gas flow is characterized by transition flow or Knudsen diffusion. In most cases, these two regimes coexist in nanopore in shale and account for different weights. Ertekin et al. [12] provided the weights for slip flow and Knudsen diffusion; apparent permeability is calculated by a weighted average of slip flow and Knudsen diffusion. Many new weighted models are also proposed by Liu et al. [13], Javadpour et al. [14, 15], Darabi et al. [16], and Shahri et al. [17]. These models have a relatively comprehensive analysis of gas flow in nanopores with the pore scale effect; however, some other unique properties of shale affecting gas apparent permeability are not considered.

The first characteristic of shale formation affecting apparent permeability is that there are a lot of organics and clay minerals with much gas adsorption in the shale matrix [18]. Gas adsorption in shale is generally believed to be single-layer physical adsorption [19]. It is suggested by Akkutlu and Fathi [20] that surface diffusion exists in the adsorption layer, and it is driven by a concentration gradient. Experiments of core permeability tests, pressure decay tests, and numerical calculation show that the permeability measured and calculated with adsorptive gas is much larger than that with nonadsorptive gas and indicate that the high permeability is caused by surface diffusion of adsorptive gas [21–23]. Many theories have been presented to describe surface diffusion in porous media, in which the hopping model is most widely used for surface diffusion [24–27]. If enough energy is acquired by the adsorbed gas molecule and it bounces to the nearest adsorption site, activation process and surface diffusion happen. It is verified that it is reasonable to use Langmuir isotherms to study surface diffusion [28]. Wu et al. [29–31] proposed a surface diffusion model which takes account of coverage of adsorbed gas at high pressure. Although surface diffusion is incorporated in these models, the effect of the adsorbed layer on gas retention and flow capacity is often neglected, which is not negligible as the radius of shale nanopores is in the same order with that of methane molecules. Another impact factor of shale formation is that gas in shale nanopores is dense gas rather than rarefied gas [32]. In shale nanopores, the storage and transport space for gas molecules is in the same order with size of gas molecules and therefore makes the assumption of rarefied gas no longer valid and need correction. The intrinsic size of molecules and the interaction between molecules are negligible for ideal gas. Wang et al. [33, 34] build a multiscale scheme to capture both slip and nonideal gas effects and considered the Enskog equation to cover the dense gas effect in the nanochannel. However, the effects of the adsorption layer, surface diffusion, and dense gas in formation conditions are not all considered in most of the existing models, and an apparent permeability model is needed to incorporate all these impact factors.

This paper presents a comprehensive apparent permeability model in which all the flow mechanisms, including viscous flow, slip flow, Knudsen diffusion, adsorption layer,

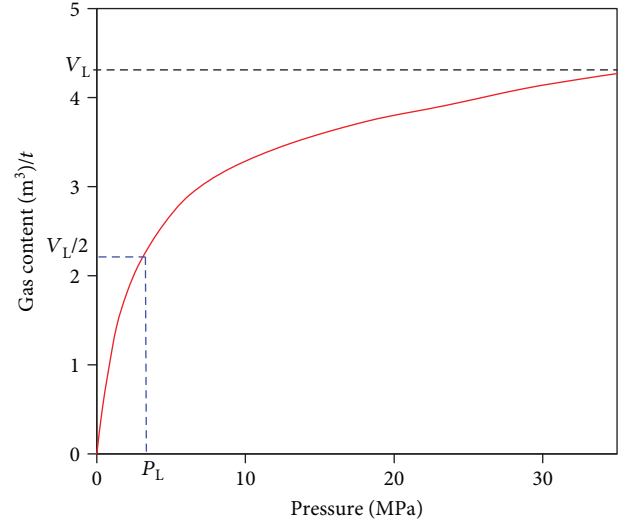


FIGURE 1: Langmuir adsorption isotherm.

surface diffusion, and dense gas effect, are taken into account. Then the effects of the desorption layer, surface diffusion, and dense gas in shale nanopores with different diameters are analyzed.

2. Apparent Permeability Model for Shale Nanopores

2.1. Adsorption Layer. The Langmuir isothermal adsorption equation is widely used to describe the adsorption and desorption of coal bed methane [32] and also introduced into the study of the transport regime of shale gas. It is based on instantaneous phase equilibrium; that is, adsorption or desorption due to pressure change is completed instantaneously. As the permeability of the shale matrix is extremely low, desorption time is negligible compared with gas flow in nanopores and the assumption made by Langmuir is also valid in shale gas reservoirs. The equation is as follows:

$$V = \frac{V_L \cdot p}{p_L + p}, \quad (1)$$

in which V is the volume of adsorbed gas per unit mass of shale, m^3/t ; V_L is the Langmuir volume, m^3/t , denoting the maximum adsorption capacity of the shale matrix at a certain temperature; and p_L is the Langmuir pressure, MPa, denoting the pressure at which the actual adsorption is half of the maximum adsorption on the adsorption isotherm, as shown in Figure 1.

As the radius of shale nanopores is in the same order with that of methane molecules, the effect of the adsorbed layer on gas retention and flow capacity is not negligible. For example, a pore whose diameter is 4 nm cannot allow 10 methane molecules at most to pass at the same time. In a single capillary, the adsorbed layer reduces the capacity of fluid flow, as shown in Figure 2. However, the effect of the adsorbed layer varies with different pore diameters: for pores whose diameter is larger than 100 nm, the effect

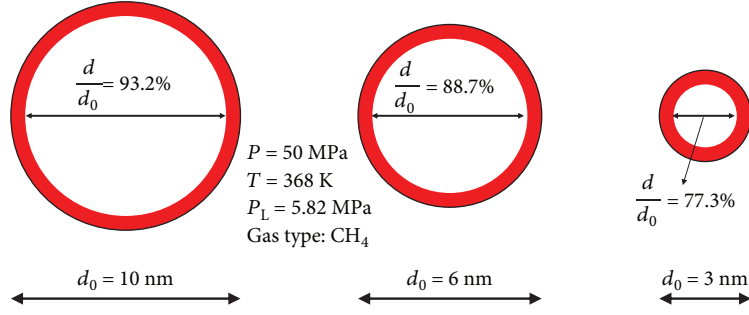


FIGURE 2: The effect of the adsorbed layer on the effective sectional flow area of pores of different diameters.

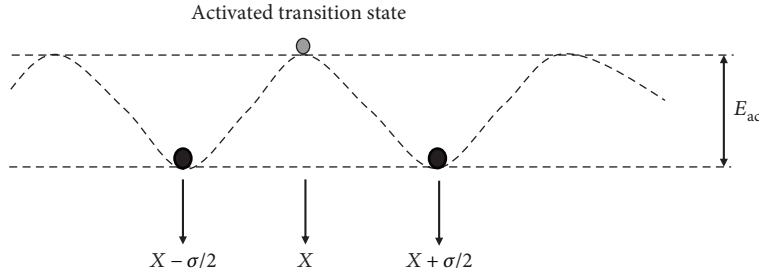


FIGURE 3: Hopping model for surface diffusion.

is negligible; for pores whose diameter is smaller than 10 nm, the adsorbed layer accounts for a large portion of the shale pores and narrows the flow channel significantly, as shown in Figure 2.

The adsorbed layer is taken into account in this paper with the assumption of single-layer adsorption. As adsorption molecules do not exist on all adsorption sites, coverage of adsorption molecules is introduced to calculate the thickness of the adsorbed layer; the effective pore diameter is [11]

$$d = d_0 - 2d_M\theta, \quad (2)$$

in which d_0 is the actual pore diameter, m; d_M is the diameter of gas molecules, m; and θ is the coverage of adsorbed gas based on (1), dimensionless, and it is defined as

$$\theta = \frac{p}{p_L + p}. \quad (3)$$

The effective pore radius is

$$r = \frac{d}{2}. \quad (4)$$

The hopping model is used in this paper to characterize surface diffusion in shale gas reservoirs, as shown in Figure 3. According to the hopping model, if enough energy is acquired by the adsorbed gas molecule and it bounces to the nearest adsorption site, activation process and surface diffusion happen. The surface diffusion model in this paper is based on the model of Wu et al. [29], and the assumptions are as follows:

- (1) A local equilibrium exists between bulk gas and adsorbed gas.

- (2) Surface transport takes place by activated diffusion, that is, site hopping.
- (3) The surface diffusion coefficient at higher pressure can be corrected by that at lower pressure with coverage of adsorbed gas defined in (3).

A surface diffusion coefficient at higher pressure is offered by correcting the coefficient at lower pressure, considering the effect of gas coverage on surface diffusion [26]:

$$D_s = D_s^0 \frac{(1 - \theta) + (\kappa/2)\theta(2 - \theta) + \{H(1 - \kappa)\}(1 - \kappa)(\kappa/2)\theta^2}{(1 - \theta + (\kappa/2)\theta)^2}, \quad (5)$$

in which D_s is the surface diffusion coefficient, m^2/s ; D_s^0 is the surface diffusion coefficient at low pressure, m^2/s ; $H(1 - \kappa)$ is the Heaviside function, dimensionless; θ is the coverage of adsorbed gas defined in (3), dimensionless; and κ is the ratio of the rate constant for blockage to the rate constant for forward migration, dimensionless. According to Xiong et al. [11], D_s^0 can be calculated with (6); $H(1 - \kappa)$ is defined in (7) and (8).

$$D_s^0 = (8.29 \times 10^{-7}) T^{0.5} \exp\left(-\frac{\Delta H^{0.8}}{RT}\right), \quad (6)$$

$$H(1 - \kappa) = \begin{cases} 0, & \kappa \geq 1, \\ 1, & 0 \leq \kappa \leq 1, \end{cases} \quad (7)$$

$$\kappa = \frac{\kappa_b}{\kappa_m}, \quad (8)$$

where T is the reservoir temperature, K; ΔH is the isosteric adsorption heat at the gas coverage of zero, J/mol; R is the

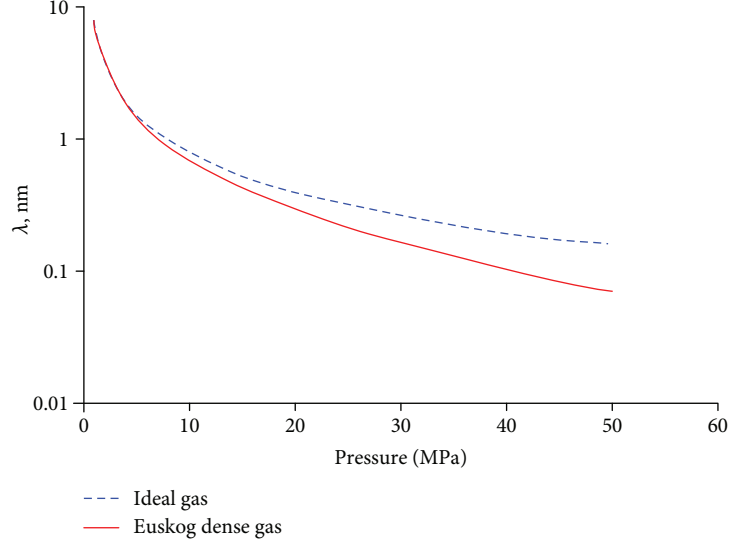


FIGURE 4: The effect of dense gas on the mean free path of gas molecules ($T = 360$ K).

gas universal constant, $8.314 \text{ J}/(\text{mol}\cdot\text{K})$; κ_m is the rate constant for forward migration, m/s; and κ_b is the rate constant for blockage, m/s. κ is set to 0.5 in this paper according to Wu et al. [29].

Eqs. (7) and (8) show that when $\kappa_m > \kappa_b$, there is a net forward movement even when the next site is occupied. When $\kappa_b > \kappa_m$, a nearly total blockage occurs. However, pore blockage cannot cause a negative movement; rather, the activated sorbate molecule stays at its original site.

2.2. Dense Gas Effect

2.2.1. Mean Free Path of Gas Molecules. The intrinsic size of molecules and the interaction between molecules are negligible for ideal gas. In this scenario, the mean free path of gas molecules can be expressed as [21]

$$\lambda = \frac{k_B T}{\sqrt{2} \pi P d_M^2}, \quad (9)$$

in which k_B is the Boltzmann constant, $1.3805 \times 10^{-23} \text{ J/K}$; T is the absolute temperature, K; P is the pressure, Pa; and d_M is the diameter of the gas molecule, m.

However, the size of the gas molecule is not negligible in actual shale formations. On the other hand, due to high pressure and short distance between gas molecules, the gas should be viewed as dense gas. According to the dense gas theory presented by Enskog [21], the mean free path of gas molecules is expressed as

$$\lambda = \frac{k_B T}{\sqrt{2} \pi \chi(\eta) P d_M^2}, \quad (10)$$

in which $\chi(\eta)$ is the collision correction factor defined by Cowling [33], dimensionless; η is a function of gas density

$$\eta = \frac{2}{3} \pi n d_M^3, \quad (11)$$

in which $n = P/k_B T$, which is the number of molecules.

2.2.2. Collision Correction Factor. According to the dense gas theory of Enskog [21], as the gas density increases, the percentage of gas molecules in the total volume is no longer negligible. Therefore, the gas molecules cannot be simplified as point particles any more, and the effect of molecular size on collision should be considered [33]

$$\Gamma' = \frac{\Gamma}{V'}, \quad (12)$$

in which $V' = 1 - 4\pi n d_M^3/3$, and Γ is the collision rate.

As the collision rate increases, a tertiary collision between molecules and the blocking effect are introduced. The rectified collision rate [33] is

$$\Gamma' = \chi(\eta) \Gamma \quad (13)$$

in which the collision correction factor [33] is

$$\chi(\eta) = \frac{1 - 11\pi n d_M^3/12}{1 - 4\pi n d_M^3/3} = \frac{1 - 11\eta/8}{1 - 2\eta}. \quad (14)$$

Eq. (12) is a function of η with first-order accuracy and is relatively accurate when $\eta < 0.03$. If a quaternary and higher collision is considered, a more accurate collision correction factor is acquired by numerical calculation [35]:

$$\chi(\eta) = 1 + 0.625\eta + 0.2869\eta^2 + 0.115\eta^3 + 0.0386\eta^4. \quad (15)$$

Figure 4 shows the variation of the mean free path of gas molecules of methane at formation pressure and a temperature of 360 K. We can see that the difference between the mean free path of gas molecules of the ideal gas and that of the dense gas effect is not significant at low pressure. However, as pressure increases, the difference becomes increasingly significant; that is, the dense gas effect is more significant at higher formation pressure. In addition, considering that nanopores are well developed

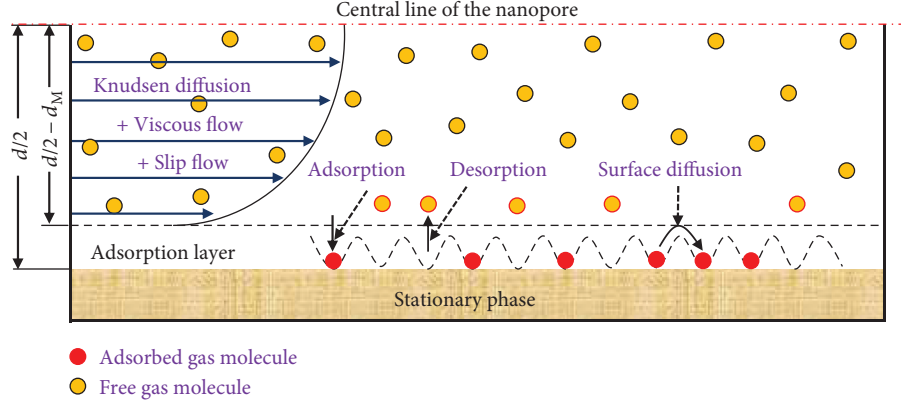


FIGURE 5: Three gas transport mechanisms in shale nanopores.

in the shale matrix and the fact that the diameter of gas molecules is in the same order as that of the pore diameter, methane molecules should not be viewed as point particles and the effect of intrinsic size of molecules should be considered.

2.3. Apparent Permeability Model. There are three transport mechanisms for gas flow in shale nanopores (see Figure 5): surface diffusion of adsorbed gas, viscous flow and slip flow caused by collision between bulk gas molecules, and Knudsen diffusion caused by collision between bulk gas molecules and the pore surface.

Based on the surface diffusion coefficient in 5, the surface diffusion permeability of the adsorbed phase in a single nanopore is acquired:

$$k_s^0 = -\frac{J_s \mu}{\rho_{\text{ads}} (\partial P / \partial x)} = \frac{D_s C_s \mu}{\rho_{\text{ads}} P}, \quad (16)$$

in which k_s^0 is the surface diffusion permeability of the adsorbed phase, mD; ρ_{ads} is the density of the adsorption gas, kg/m^3 , which is a fitting parameter of experiment data based on the Langmuir theory, which can be calculated with SLD models [36]; μ is the viscosity of the adsorption gas, mPa-s; P is the pressure; C_s is the concentration of the adsorbed gas, kg/m^3 ; and M is the gas molar mass, kg/mol .

According to Wu et al. [29], C_s can be calculated as

$$C_s = \frac{4\theta M}{\pi d_M^3 N_A}. \quad (17)$$

However, surface diffusion is the transport regime for adsorbed gas and is irrelevant to free gas in the bulk phase. Therefore, in order to get total apparent permeability, surface diffusion permeability of the adsorption layer should be corrected and combined with apparent permeability of the bulk phase. For surface diffusion, the flow section is made up by the molecules in the adsorption layer and should be converted to the effective flow section for the whole

pore, so the weighting coefficient of surface diffusion ζ_{ms} is introduced [30]:

$$\zeta_{ms} = \frac{\phi}{\tau} \left[\left(1 - \frac{d_M}{r} \right)^{-2} - 1 \right], \quad (18)$$

in which ϕ is the shale porosity and τ is the tortuosity.

In summary, surface diffusion permeability in a single capillary can be expressed as

$$k_s = \frac{\zeta_{ms} D_s C_s \mu}{\rho_{\text{ads}} P}. \quad (19)$$

For the viscous/slip flow and Knudsen diffusion of the bulk phase, the weighting coefficients are [31]

$$\bar{\omega}_v = \frac{1}{1 + \text{Kn}}, \quad (20)$$

$$\bar{\omega}_k = \frac{1}{1 + 1/\text{Kn}}, \quad (21)$$

in which Kn is the Knudsen number, which is defined as

$$\text{Kn} = \frac{\lambda}{d}. \quad (22)$$

For a single capillary, the viscous flow and slip flow permeability of the bulk phase can be expressed as

$$k_{\infty} = \frac{\phi r^2}{8\tau}. \quad (23)$$

Despite the fact that the generalized model cannot cover all the flow regimes, it is completely applicable to viscous flow and slip flow when $\text{Kn} \leq 1$. Therefore, the correction factor for permeability can be introduced to characterize the pressure-driven viscous flow and slip flow. The viscous flow or slip flow permeability of the bulk phase driven by pressure difference can be expressed as

$$k_v^0 = \frac{\phi r^2}{8\tau} f(\text{Kn}). \quad (24)$$

TABLE 1: Parameters for the validation case.

Parameter	Symbol	Unit	Value
Formation temperature	T	K	300
Porosity	ϕ	Dimensionless	0.048
Tortuosity	τ	Dimensionless	1.35
Gas type	CO ₂	—	—
Gas molecule diameter	d_M	m	4.64×10^{-10}
Gas molar mass	M	kg/mol	4.4×10^{-2}
Universal gas constant	R	J/(mol·K)	8.3145
Boltzmann constant	K_B	J/K	1.3805×10^{-23}
Molar volume of gas under standard condition	V_{std}	m ³ /mol	0.0224
Avogadro's constant	N_A	1/mol	6.02×10^{23}
Langmuir pressure	P_L	MPa	1.8
*Isosteric adsorption heat at the gas coverage of zero	ΔH	J/mol	203,000
*The ratio of the rate constant for blockage to the rate constant for forward migration	κ	Dimensionless	0.21
*Pore diameter	d_0	nm	2.8

The parameters highlighted with asterisk (*) are matched with the experimental data.

The viscous flow and slip flow permeability without considering the weighting coefficient can be expressed as [6]

$$k_v^0 = \frac{\phi r^2}{8\tau} [1 + \alpha \text{Kn}] \left[1 + \frac{4\text{Kn}}{1 + \text{Kn}} \right], \quad (25)$$

in which α is the rarefaction coefficient for ideal gas; its expression is shown in (26) by Beskok and Karniadakis [6] based on lots of experiments.

$$\alpha = \frac{128}{15\pi^2} \tan^{-1} [4\text{Kn}^{0.4}]. \quad (26)$$

The viscous flow and slip flow permeability in a single capillary driven by pressure difference considering the weighting coefficient defined in (20) is

$$k_v = \frac{\phi r^2}{8\tau} \frac{1 + \alpha \text{Kn}}{1 + \text{Kn}} \left[1 + \frac{4\text{Kn}}{1 + \text{Kn}} \right]. \quad (27)$$

The Knudsen diffusion permeability of the bulk phase is [16]

$$k_k^0 = \frac{2\phi}{3\tau} r V_{\text{std}} \mu \left(\frac{8}{\pi R T M} \right)^{0.5}, \quad (28)$$

in which V_{std} is the volume of a mole of gas under standard conditions, 0.0224 m³/mol.

The Knudsen diffusion permeability of the bulk phase, considering the weighting coefficient defined in (21), becomes

$$k_k = \frac{2\phi}{3\tau} r V_{\text{std}} \mu \left(\frac{8}{\pi R T M} \right)^{0.5} \frac{1}{1 + 1/\text{Kn}}. \quad (29)$$

The total apparent permeability of shale nanopore is

$$k_t = k_s + k_v + k_k. \quad (30)$$

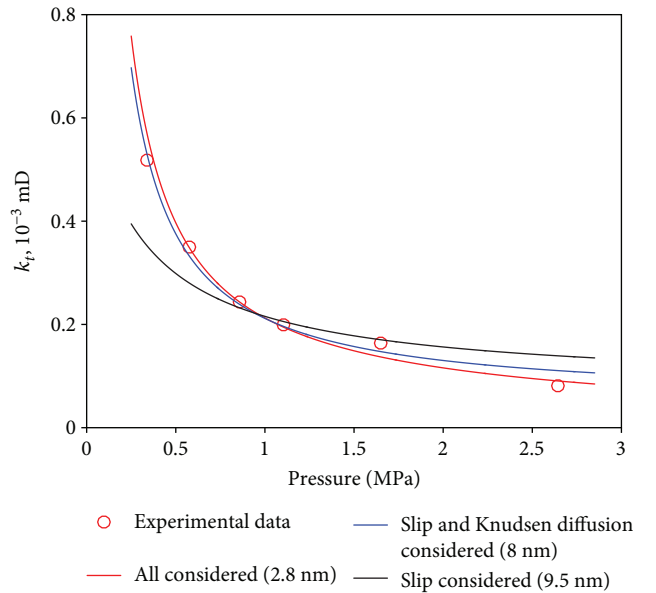


FIGURE 6: Validation of the proposed model with experimental data (from [37]).

In the apparent permeability model shown in (28), the permeability contribution of the bulk gas and the adsorption layer is calculated with an effective pore diameter, and viscous/slip flow and Knudsen diffusion are weighted as shown in (20) and (21), respectively.

3. Results and Discussion

3.1. Model Validation. To validate the model proposed in this paper, experimental data for CO₂ from [37, 38] is applied. This experiment used extremely accurate differential-pressure transducers to measure the flow of gas passing

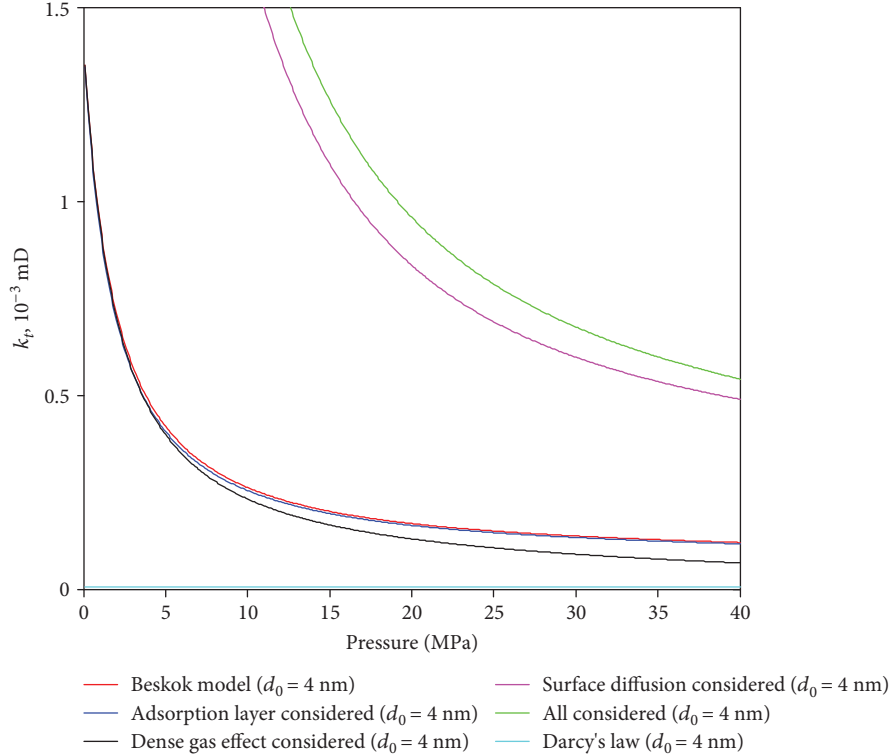


FIGURE 7: The effect of different factors on total apparent permeability (pore diameter = 4 nm).

through the core sample under in situ conditions. And the laboratory set-up is fully automated to avoid human error and maintain the temperature stable. In the experiments, organic-rich shale samples from Marcellus shale are used and CO_2 is used as absorbent gas. Therefore, the experiment data is applied to validate the model with surface diffusion considered in this study. The detail of the experiment is presented in [38].

The parameters are shown in Table 1, in which the parameters highlighted with asterisk (*) are matched with the experimental data. The density of bulk gas is calculated in (31); gas viscosity and the z -factor are calculated with the numerical approximate method proposed by Lee et al. [39] and Dranchuk and Abou-Kassem [40]. The density of adsorption gas can be a fitting parameter of experiment data based on the Langmuir theory; it can be calculated with SLD models [36] more accurately.

$$\rho = \frac{pM}{zRT}. \quad (31)$$

In this study, three models are used to match the experiment data as shown in Figure 6. In the first model, gas slippage is considered; we could find that the matching result is not good. In the second model, both slippage and Knudsen diffusion are considered; the result shows that this model has a better fit than the first model. In the third model, all the effects are considered, and we got the best fit here. On the other hand, we could find that the fitting average pore diameter differs from each other. If more flow mechanisms are considered, the fitting average pore diameter would be

smaller. At the same time, we could find that the fitting average pore diameter using the third model is far smaller than the other two models; this is because surface diffusion has a great impact on gas transport for this case (the pressure is quite low and the pore size is in nanoscale). The effects of different flow mechanisms and pore diameter on transient behavior will be discussed later in this study.

3.2. Applicability of the Model. The apparent permeability model of shale nanopores presented in this paper is compared with previous models, as shown in Figure 7. Parameters used in the model are shown in Table 2.

Figure 7 shows the total apparent permeability of shale (pore diameter = 4 nm) at different pressures, in which various factors are considered. We can see that the effect of the adsorption layer and dense gas on total apparent permeability is not significant, when compared with Beskok's model, while surface diffusion increases total apparent permeability considerably. As pressure increases, the improvement of total apparent permeability due to surface diffusion decreases, the dense gas effect reduces total apparent permeability, and the effect of the adsorption layer on total apparent permeability is still insignificant; therefore, the increment of total apparent permeability due to all three factors decreases with increased pressure.

Figure 8 shows total apparent permeability of shale (pore diameter = 50 nm) at different pressures, in which various factors are considered. We can conclude from the figure that the effect of the adsorption layer on total apparent permeability is still insignificant compared with Beskok's model [6]. In

TABLE 2: Parameters for modeling results and discussion.

Parameter	Symbol	Unit	Value
Formation temperature	T	K	368
Porosity	ϕ	Dimensionless	0.05
Tortuosity	τ	Dimensionless	3.5
Gas type	CH_4	—	—
Gas molecule diameter	d_M	m	3.8×10^{-10}
Gas molar mass	M	kg/mol	1.6×10^{-2}
Universal gas constant	R	J/(mol·K)	8.3145
Boltzmann constant	K_B	J/K	1.3805×10^{-23}
Molar volume of gas under standard condition	V_{std}	m^3/mol	0.0224
Avogadro's constant	N_A	1/mol	6.02×10^{23}
Langmuir pressure	P_L	MPa	5.82
Isosteric adsorption heat at the gas coverage of zero	ΔH	J/mol	16,000
The ratio of the rate constant for blockage to the rate constant for forward migration	κ	Dimensionless	0.5
Pore diameter	d_0	nm	2/4/10/20/50/100/200

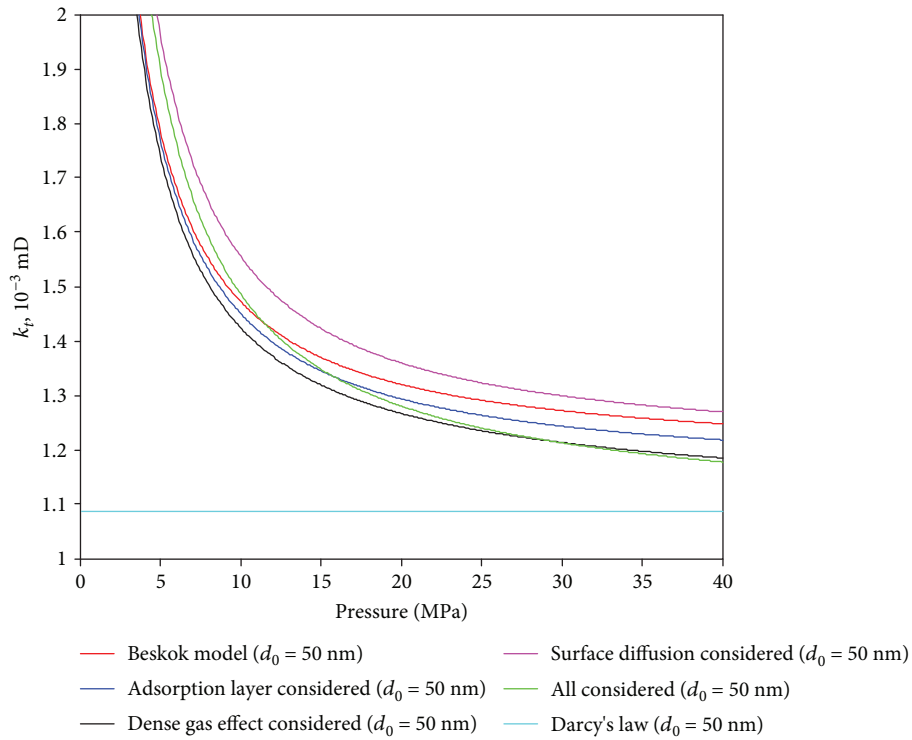


FIGURE 8: The effect of different factors on total apparent permeability (pore diameter = 50 nm).

addition, surface diffusion is smaller at high pressure, when compared with Figure 7.

3.3. Composition of Apparent Permeability. Parameters used in this section are shown in Table 2. Figure 9 shows surface diffusion permeability and its percentage in total apparent permeability at different pressures. We can see that surface

diffusion permeability is higher at low pressure and contributes more to total apparent permeability, and it considerably decreases with increasing pressure, because the desorption of the adsorbed phase reduces the coverage rate and thus decreases the concentration of adsorbed gas, which is unfavorable for surface diffusion; however, the decrement of the coverage rate increases the vacancy rate of adsorption sites,

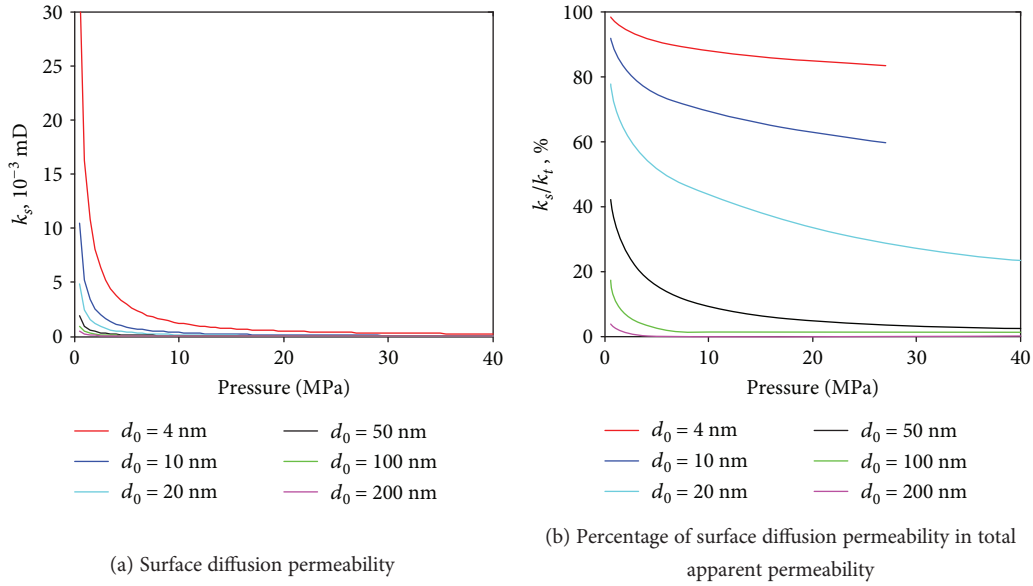


FIGURE 9: Surface diffusion permeability and its percentage in total apparent permeability.

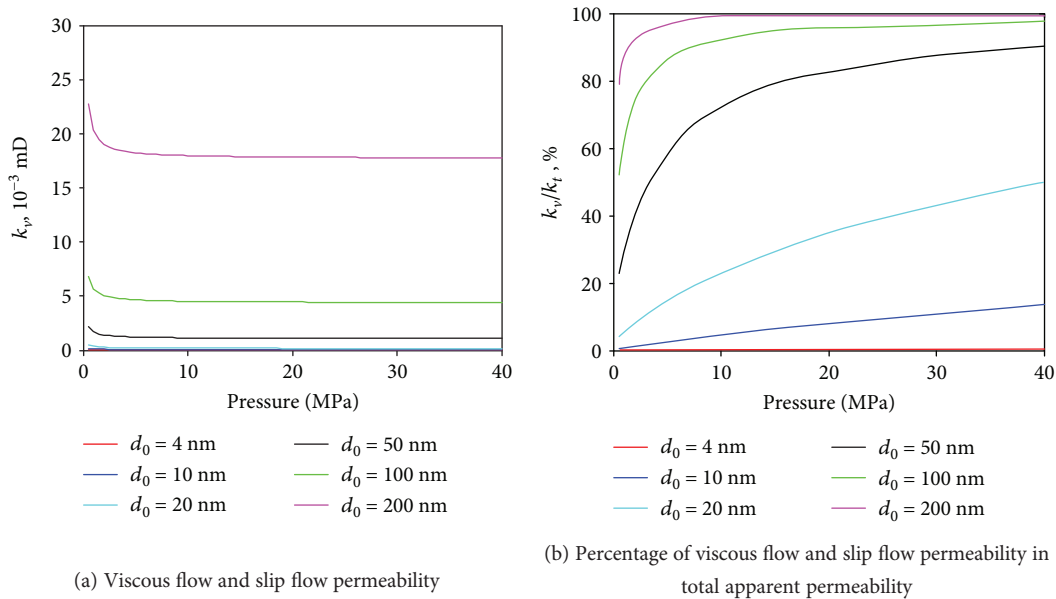


FIGURE 10: Viscous flow and slip flow permeability and their percentage in total apparent permeability.

which is favorable for adsorbed gas molecules to jump from one adsorption site to another. Consequently, surface diffusion permeability at low pressure is larger.

Meanwhile, in smaller pores, the percentage of the adsorption layer in pore space is larger and the surface diffusion effect is more significant: when the pore diameter is no more than 10 nm, the contribution of surface diffusion to total apparent permeability is more than 60% even when formation pressure is up to 40 MPa; when the pore diameter is more than 50 nm, the percentage of surface diffusion permeability is smaller than 10% even when pressure is as low as 5 MPa.

Figure 10 shows viscous flow and slip flow permeability driven by pressure difference and its percentage in total

apparent permeability at different pressures. From the figure, we can see that the viscous flow and slip flow permeability are higher at lower pressure and decrease with increasing pressure. The explanation is that as pressure increases, the mean free path of gas molecules and the Knudsen number increase, the correction factor of permeability becomes smaller, the transport mechanism transits from slip flow to viscous flow, the gas slip effect becomes weaker, and apparent permeability driven by pressure difference approaches a constant.

The viscous flow and slip flow permeability and surface diffusion permeability are in the same magnitude and decrease with increasing pressure, but the decline rate of the former is significantly smaller than that of the latter,

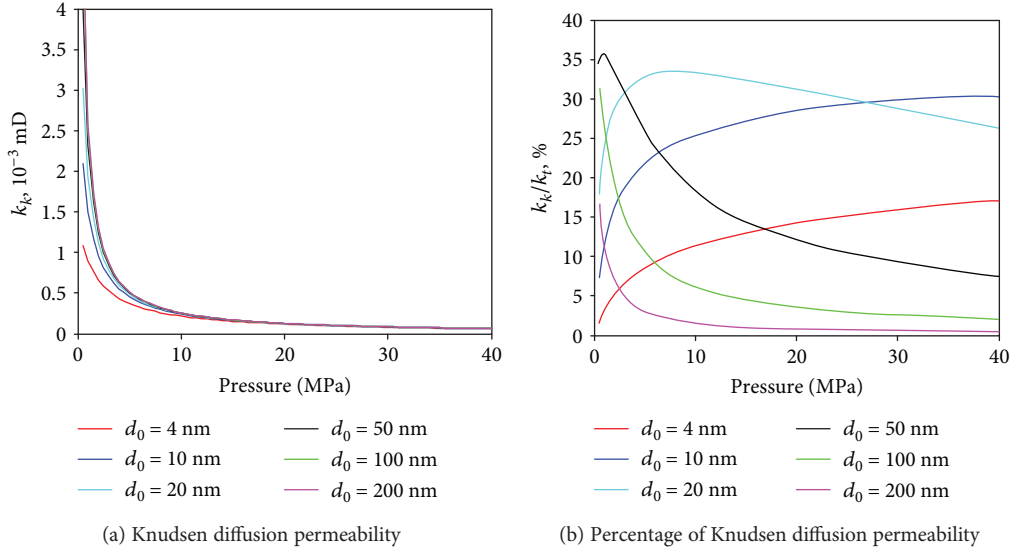


FIGURE 11: Knudsen diffusion permeability and its percentage in total apparent permeability.

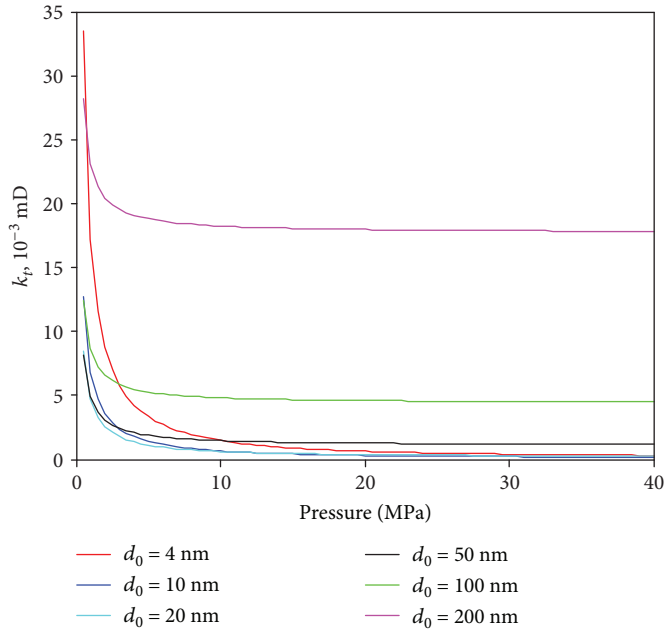


FIGURE 12: Apparent permeability of shale nanopores of different diameters.

and the percentage of viscous flow and slip flow in total apparent permeability increases with increasing pressure. For pores whose diameter is larger than 50 nm, viscous flow and slip flow permeability is dominant and even when pressure decreases to 5 MPa, the contribution is more than 70%; for pores whose diameter is no more than 10 nm, even when pressure reaches 40 MP, the percentage of viscous flow and slip flow in total apparent permeability is smaller than 15%.

Figure 11 shows Knudsen diffusion permeability and its percentage in total apparent permeability at different pressures. We can see from the figure that Knudsen diffusion permeability is higher at low pressure and it decreases rapidly

with pressure, because as pressure increases, the mean free path of gas molecules decreases, the Knudsen number becomes smaller, and the collision between gas molecules and the pore surface becomes smaller and even negligible. At low pressure, smaller diameter means larger Knudsen number and the collision rate of gas molecules and the pore surface is high and therefore makes Knudsen diffusion permeability larger.

The percentage of Knudsen diffusion permeability in total apparent permeability depends on both formation pressure and pore diameter. For pores whose diameter is larger than 50 nm, the percentage of k_v is dominant, while k_v/k_t increases with increasing pressure and therefore makes the

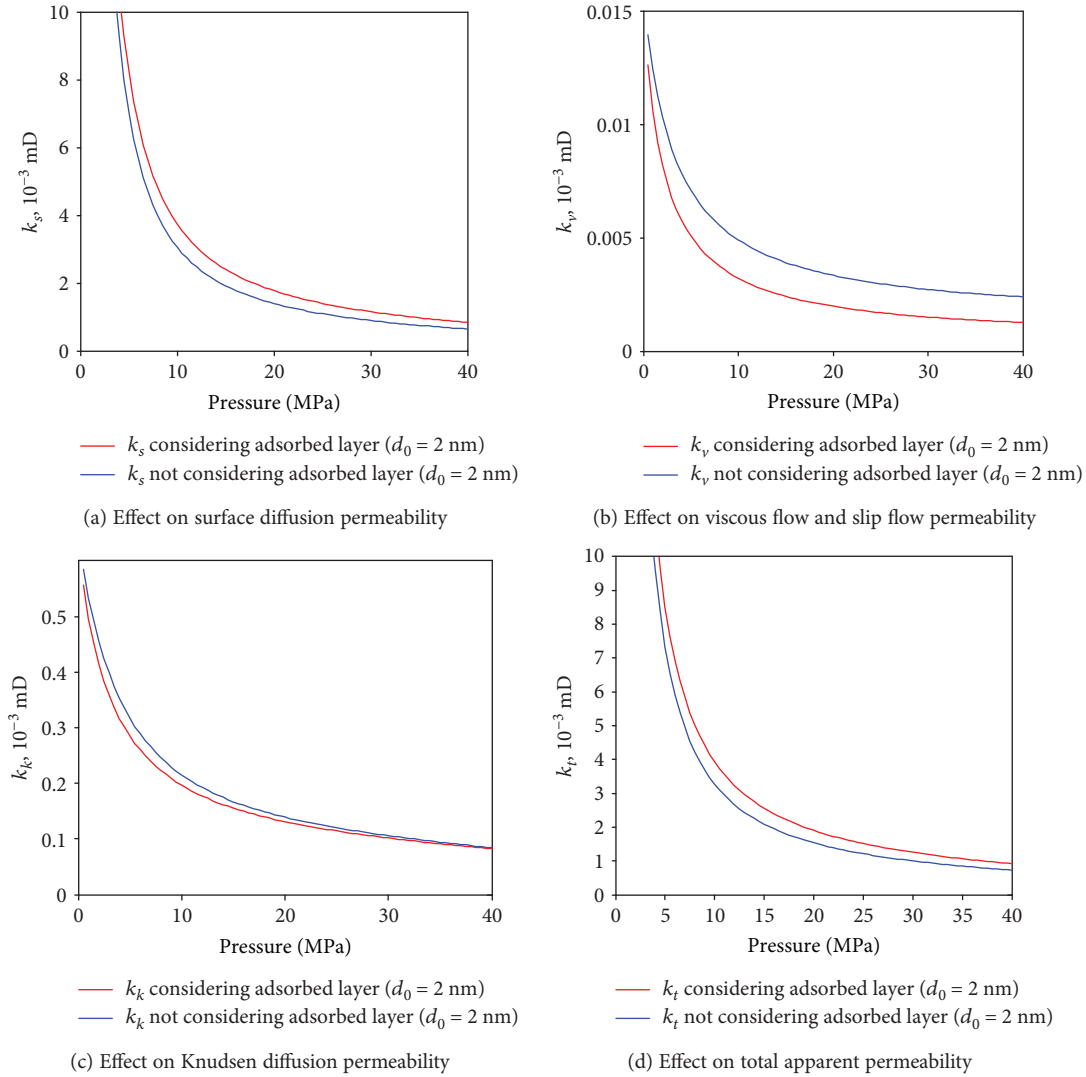


FIGURE 13: The effect of the adsorbed layer on apparent permeability of shale (pore diameter = 2 nm).

percentage of Knudsen diffusion permeability decrease with increasing pressure; for pores whose diameter is no more than 10 nm, the percentage of k_s is dominant and k_s/k_t decreases with increasing pressure and therefore makes the percentage of Knudsen diffusion in total apparent permeability increase with increasing pressure; for pores whose diameter is around 20 nm, k_k/k_t increases and then decreases with increasing pressure.

Figure 12 shows total apparent permeability of a single capillary at different pressures. We can see from the figure that total apparent permeability decreases with increasing pressure and there is a plateau when the pressure is larger than 10 MPa, which is the Klinkenberg permeability. At low pressure, however, as the mean free path of gas molecules is large, the collision between gas molecules and the pore surface (Knudsen diffusion) and hopping of the adsorbed phase dramatically improve total apparent permeability, and this effect is more significant for a smaller diameter. As shown in Figure 9, the surface diffusion effect is more significant in small pores and particularly significant at low pressure, while

viscous and slip flow are more significant at large pores. Therefore, there is an intersection for the curves of total apparent permeability of a single capillary of different grades of diameter. And when ΔH and κ are larger, the contribution of surface diffusion will decrease; the intersections will happen at lower pressure. For example, when pressure is lower than 2.5 MPa, the total apparent permeability of a single capillary whose diameter is 100 nm is smaller than that whose diameter is 4 nm. However, this does not mean that the flow rate in a 4 nm tube can be larger than that of a 100 nm tube, because the flow section for a 100 nm tube is more than 500 times that of a 4 nm tube.

3.4. Sensitivity Analysis. In this section, the effect of the adsorbed layer, Knudsen diffusion, dense gas effect, and pore size distribution on apparent permeability is analyzed; the parameters of the model are shown in Table 2.

3.4.1. Adsorbed Layer. The effect of the adsorption layer on total apparent permeability of shale (pore diameter = 2 nm)

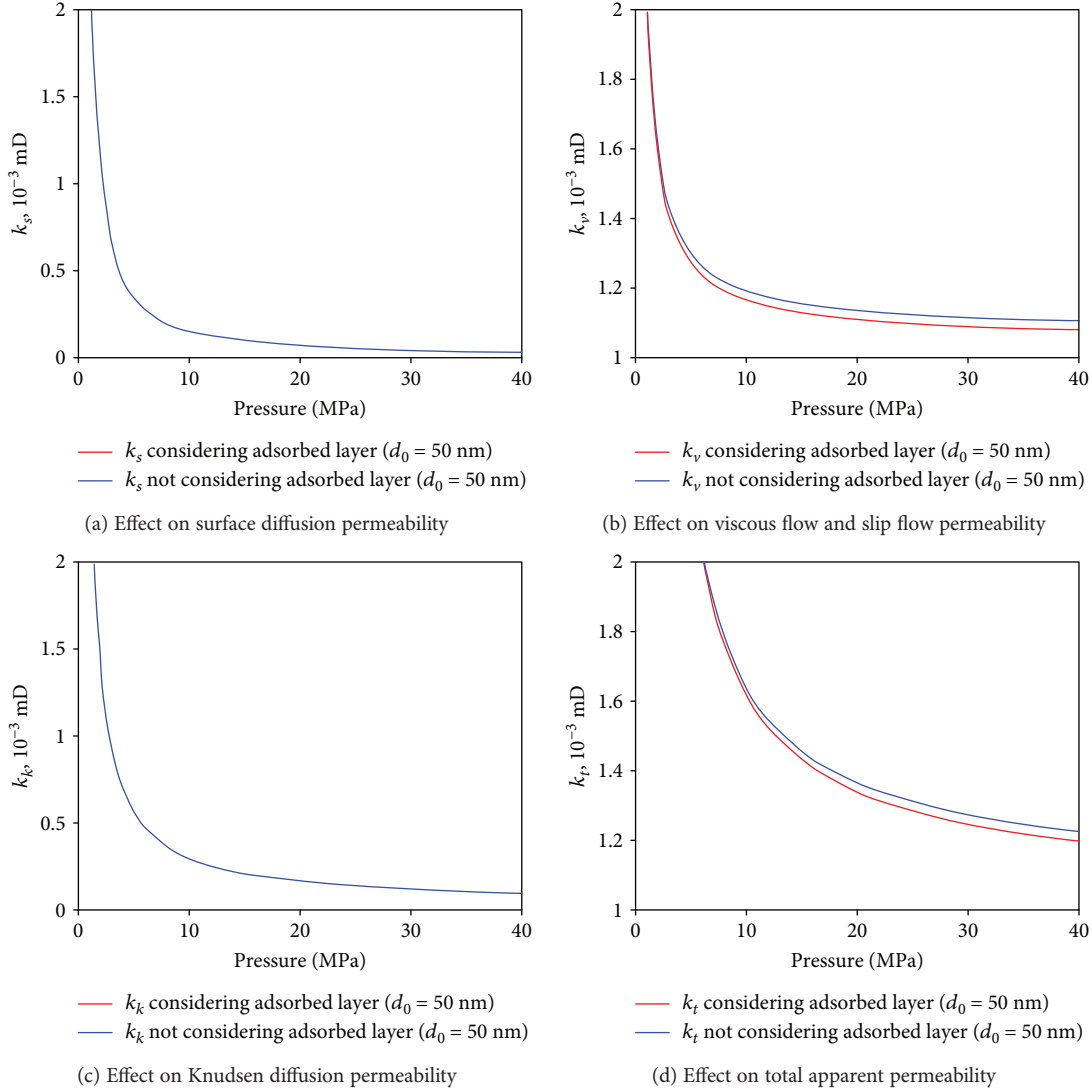


FIGURE 14: The effect of adsorbed layer on apparent permeability of shale (pore diameter = 50 nm).

is shown in Figure 13. Figure 13 indicates that the effect of the adsorption layer on three kinds of permeability is significant, because the adsorption layer reduces the effective flow space in nanopores and thus intensifies surface diffusion but reduces viscous flow and slip flow permeability as well as Knudsen diffusion permeability. As a result, despite that total apparent permeability is mainly affected by surface diffusion, the adsorbed layer improves total apparent permeability.

The effect of the adsorption layer on total apparent permeability of shale (pore diameter = 50 nm) is shown in Figure 14. Figure 14 indicates that the effect of the adsorption layer on three kinds of permeability and total apparent permeability is insignificant, because the percentage of the adsorption layer in the 50 nm pore is negligible. The adsorption layer reduces the effective flow space in nanopores and intensifies surface diffusion permeability but reduces viscous flow and slip flow permeability and Knudsen diffusion permeability. However, total apparent

permeability in the 50 nm pore is predominantly affected by viscous flow and slip flow; therefore, the adsorption layer reduces total apparent permeability.

In order to characterize the effect of the adsorption layer on total apparent permeability, the improvement factor of total apparent permeability due to adsorption layer is defined as

$$\varepsilon_{\text{ads}} = \frac{k_{t(\text{considers adsorbed layer})} - k_{t(\text{does not consider adsorbed layer})}}{k_{t(\text{does not consider adsorbed layer})}} \times 100\%. \quad (32)$$

Figure 15 shows the improvement factor of total apparent permeability due to the adsorption layer at 20 MPa. From the figure, we can see that for pores whose diameter is smaller than 20 nm, as total apparent permeability is dominated by surface diffusion, the introduction of the adsorption layer improves total apparent permeability; for pores whose diameter is larger than 20 nm, as total apparent

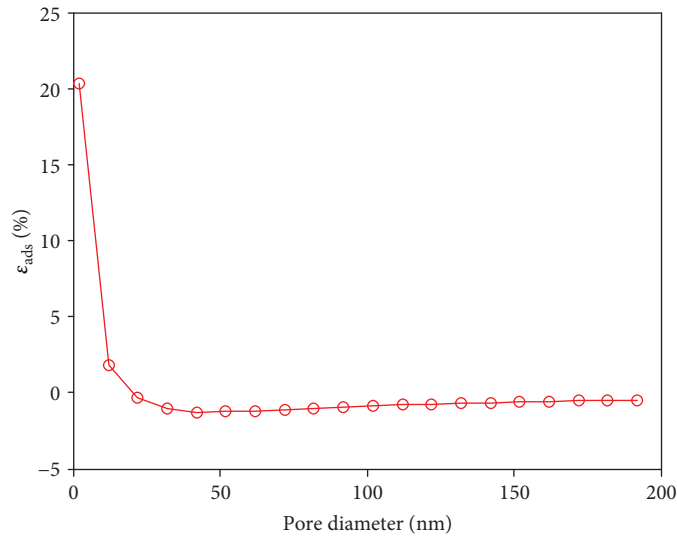


FIGURE 15: The effect of the adsorbed layer on total apparent permeability (formation pressure = 20 MPa).

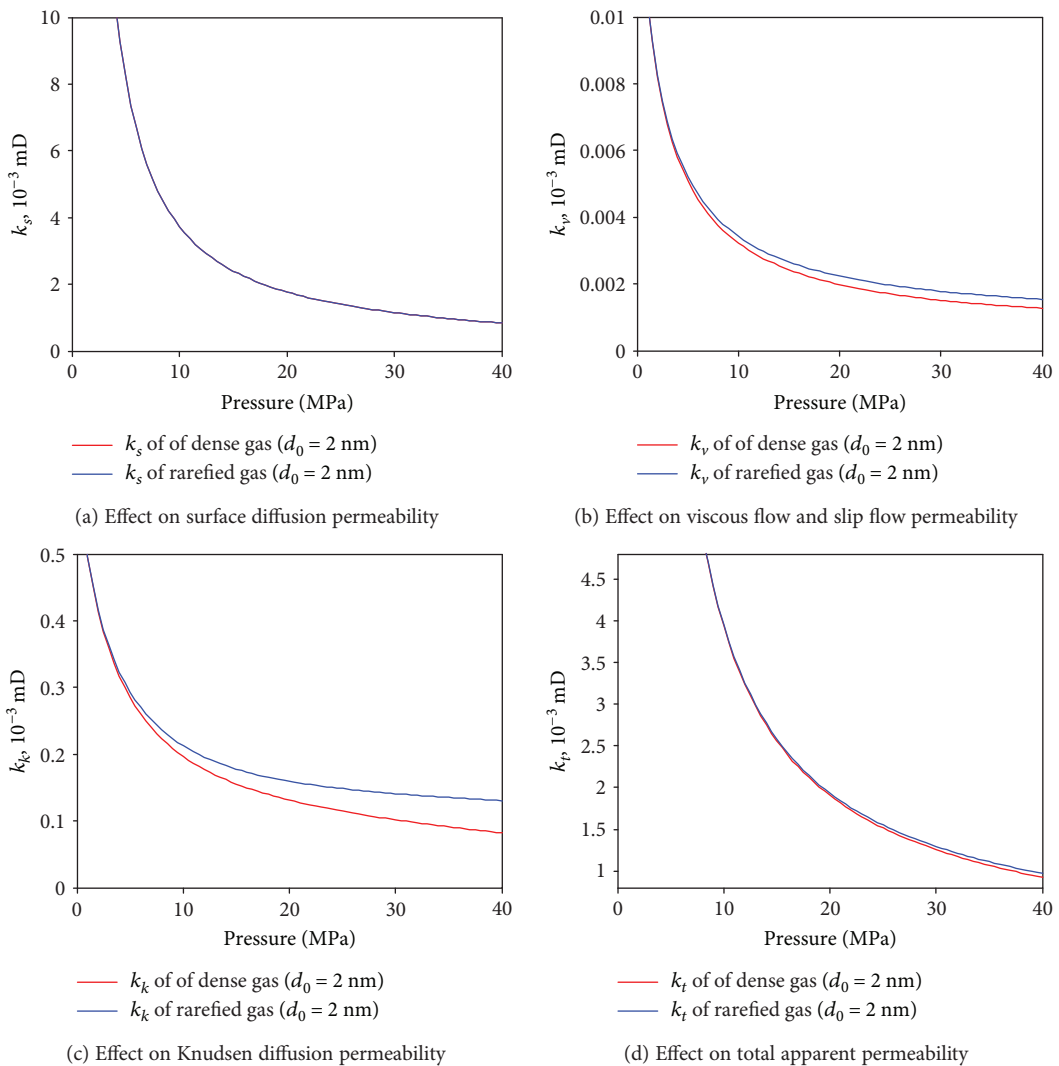


FIGURE 16: The effect of gas density on apparent permeability of shale (pore diameter = 2 nm).

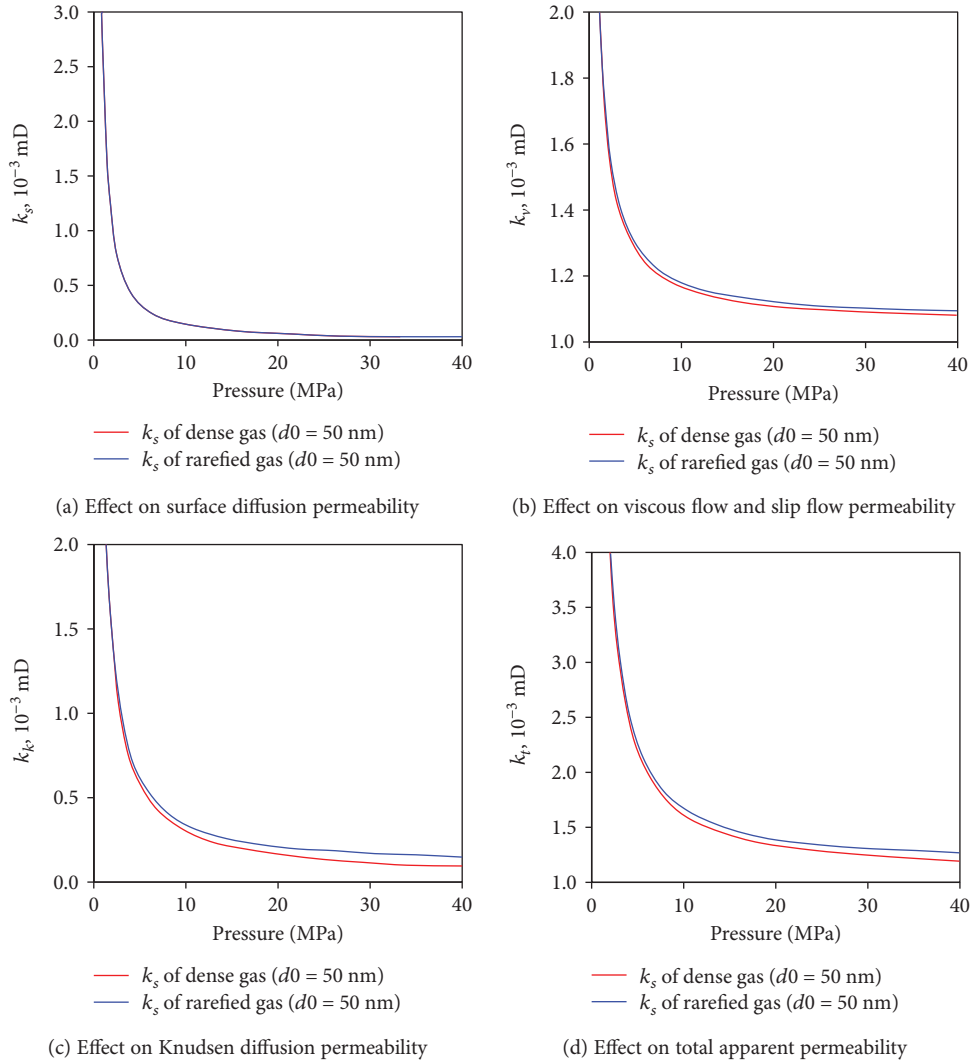


FIGURE 17: The effect of gas density on apparent permeability of shale (pore diameter = 50 nm).

permeability is dominated by Darcy flow or slip flow, the adsorption layer reduces total parent permeability. In addition, both improving and reducing effect becomes weaker as pore diameter increases.

3.4.2. Dense Gas Effect. Figure 16 shows the effect of dense gas on total apparent permeability of shale (pore diameter = 2 nm). From the figure, we can see that the effect of dense gas on all kinds of apparent permeability is insignificant in spite of pressure change. As dense gas effect reduces the mean free path of gas molecules and therefore reduces the Knudsen number, slip flow and Knudsen diffusion permeability are reduced, while surface diffusion permeability keeps constant. Therefore, the dense gas effect reduces total apparent permeability.

Figure 17 shows the effect of dense gas on total apparent permeability of 50 nm pores. The trend of Figure 17 is similar to that of Figure 16, with the difference that the effect is even more insignificant in this scenario.

Similarly, in order to characterize the effect of dense gas on total apparent permeability, the improvement factor

of total apparent permeability due to dense gas effect is defined as

$$\varepsilon_{\text{ads}} = \frac{k_{t(\text{considers dense gas effect})} - k_{t(\text{does not consider dense gas effect})}}{k_{t(\text{does not consider dense gas effect})}} \times 100\%. \quad (33)$$

Figure 18 shows the improvement factor of total apparent permeability of pores of different diameters due to dense gas effect. From the figure, we can see that the dense gas effect reduces total apparent permeability. For pores whose diameter is smaller than 20 nm, total apparent permeability is dominated by surface diffusion permeability, which is barely affected by the dense gas effect, so the effect of dense gas on total apparent permeability is insignificant when the pore diameter is very small. As the pore diameter increases, the percentage of surface diffusion permeability in total apparent permeability gradually decreases and therefore the decline rate of total apparent permeability increases with increasing pore diameter. For pores whose diameter is larger than 20 nm, total apparent permeability is generally affected by

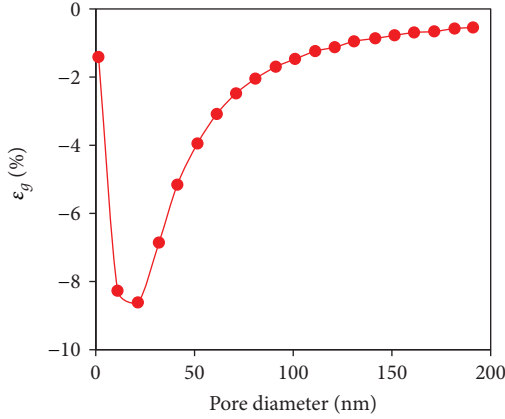


FIGURE 18: The effect of gas density on total apparent permeability (20 MPa).

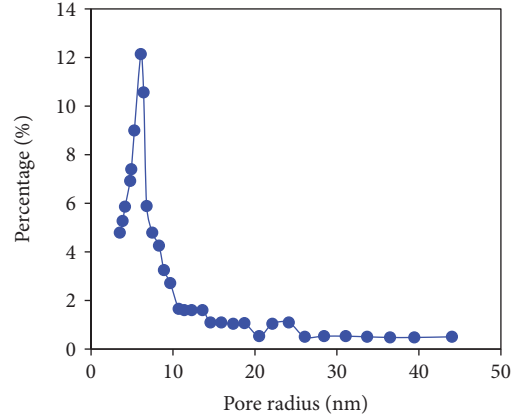


FIGURE 20: Pore size distribution curves of typical shale in Barnett (from [41]).

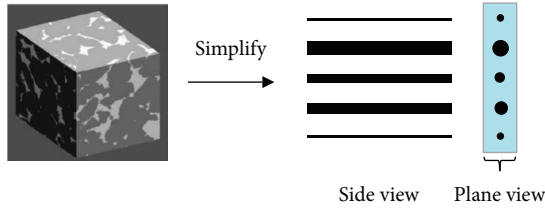


FIGURE 19: Schematic of capillary bundle.

Darcy flow or slip flow, which is reduced by introduction of the dense gas effect. As the pore diameter increases, the effect of dense gas on the mean free path decreases and therefore the decline rate of total apparent permeability decreases.

3.4.3. *Pore Size Distribution.* Gas retention and transport mechanism in shale nanopores is closely related to the pore diameter. However, pore size distribution of the shale core is in a wide range, the effect of the adsorption layer on pores of different diameters varies, and consequently the Knudsen number at the same temperature and pressure is different. Therefore, pore size distribution should be considered in the characterization of total apparent permeability of actual shale formation to make it more feasible.

Based on the transport mechanism for a single capillary in shale gas reservoirs, the storage space in shale is simplified as ideal rock which is made up by a bundle of capillaries of various diameters, as shown in Figure 19. Pore distribution of a shale formation of interest is used for calculation of apparent permeability, as shown in Figure 20 (the data is from [41]). Total apparent permeability k_{ta} can be expressed as

$$k_{ta} = \frac{\sum_{i=1}^N k_{ti} (d_i/2)^2 \chi_i}{\sum_{i=1}^N (d_i/2)^2 \chi_i}, \quad (34)$$

where d_i is the effective pore diameter of capillary i , m; χ_i is the percentage of capillary i , %; and k_{ti} is the total apparent permeability of capillary i , m.

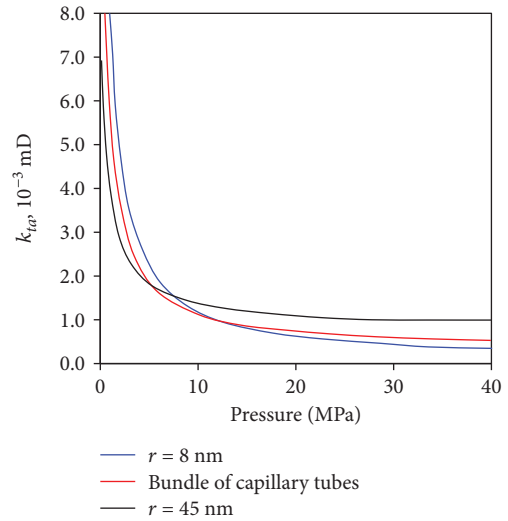


FIGURE 21: Total apparent permeability of type shale.

In the capillary bundle model, the tortuosity of each capillary is 3.5, which is an assumption in this case. Actually, this value may be higher than its truth, and different capillaries are of different tortuosity.

The model is used to analyze the apparent permeability of typical shale at different pressure, as shown in Figure 21. The figure shows that pore size distribution of the typical shale makes it equivalent to a single capillary, whose diameter is between 8 nm and 45 nm. In addition, when the pressure is larger than 20 MPa, the apparent permeability of shale approaches a constant, that is, Klinkenberg permeability, because the mean free path of gas molecules and Knudsen number are small and make the percentage of Knudsen diffusion and surface diffusion small.

3.5. *Permeability Calculation Procedure and Model Limitations.* If a certain shale field is given, the apparent permeability can be calculated with the procedure shown in Figure 22. The parameters should be obtained beforehand

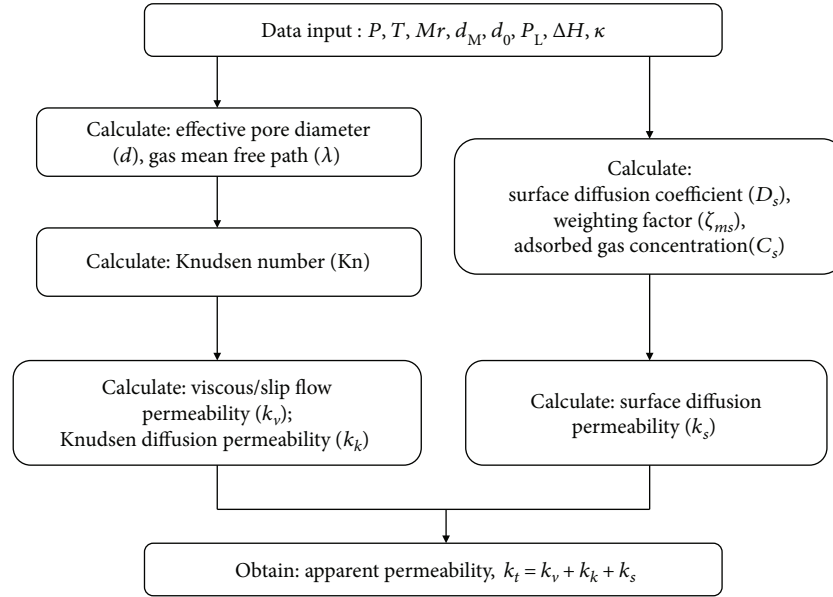


FIGURE 22: Procedure for apparent permeability calculation.

including formation temperature, porosity, pore diameter, gas type, and its physical and thermodynamic parameters as shown in Table 2. Formation temperature, porosity, and pore diameter can be obtained by geological analysis. Gas molecule diameter and molar mass are determined if a certain type of gas is given. Langmuir pressure should be obtained with isothermal adsorption tests, and isosteric adsorption heat can be calculated with the Clausius-Clapeyron equation [42]. The ratio of the rate constant for blockage to the rate constant for forward migration κ is a constant which should be evaluated, which can be set as 0.5 for flow in nanopores referring to Wu et al. [29].

However, there are still some limitations for this model. The pore size will change at high pressure because of the reduction of effective stress [43]. This apparent permeability model is based on a single nanopore, while the permeability in core scale should be given in reservoir simulation and rate/pressure transient analysis. Based on pore structure characterization [44], a pore network model is needed to accomplish this based on the apparent permeability model proposed in this paper, and this is our future work.

4. Conclusions

An apparent permeability model is presented in this paper, in which multiple flow mechanisms, including viscous flow, slip flow, Knudsen diffusion, adsorption layer, surface diffusion, and dense gas effect are taken into account. The main findings can be summarized as follows:

- (1) The effect of the adsorption layer and dense gas on apparent permeability of shale nanopores is characterized and surface diffusion of adsorbed gas is introduced to establish an apparent permeability model for the shale matrix.

- (2) Apparent permeability of the shale matrix is composed of three parts: surface diffusion permeability of the adsorbed phase, Darcy flow and slip flow permeability of the bulk phase, and Knudsen diffusion permeability of the bulk phase. The percentage of permeability caused by various mechanisms in total apparent permeability depends on pore diameters: when the pore diameter is larger than 50 nm, Darcy flow and slip flow of the bulk phase are dominant transport mechanisms; when the pore diameter is no more than 10 nm, surface diffusion of the adsorbed phase is the dominant transport mechanism; when the pore diameter is between 10 and 50 nm, especially when the pore diameter is around 20 nm, the percentage of surface diffusion of the adsorbed phase, Darcy flow, and slip flow of the bulk phase and Knudsen diffusion of the bulk phase is equivalent.
- (3) If pressure is more than 20 MPa, for pores whose diameter is smaller than 20 nm, the adsorption layer improves total apparent permeability; for pores whose diameter is larger than 20 nm, the adsorption layer reduces total apparent permeability.
- (4) If pressure is less than 20 MPa, for pores whose diameter is smaller than 20 nm, the dense gas effect makes the declining rate of total apparent permeability increase with pore diameter; for pores whose diameter is larger than 20 nm, the dense gas effect makes the declining rate of total apparent permeability decrease with pore diameter.

Disclosure

This study was once presented in “China Shale Gas 2015 (International Conference)”.

Conflicts of Interest

The authors declare that they have no conflicts of interest.

Acknowledgments

This study is supported by the National Science and Technology Major Project (no. 2017ZX05037001) and National Natural Science Fund of China (nos. 41672132 and U1762210).

References

- [1] I. Urbina, *Insiders Sound an Alarm Amid a Natural Gas Rush*, New York Times, New York, NY, USA, 2011.
- [2] V. Swami and A. Settari, "A pore scale gas flow model for shale gas reservoir," in *SPE Americas Unconventional Resources Conference*, Pennsylvania, USA, 2012.
- [3] A. J. Mallon and R. E. Swarbrick, "How should permeability be measured in fine-grained lithologies? Evidence from the chalk," *Geofluids*, vol. 8, no. 1, 45 pages, 2008.
- [4] J. Billiotte, D. Yang, and K. Su, "Experimental study on gas permeability of mudstones," *Physics and Chemistry of the Earth Parts A/B/C*, vol. 33, Supplement 1, pp. S231–S236, 2008.
- [5] D. L. Luffel, C. W. Hopkins, and P. D. Schettler, "Matrix permeability measurement of gas productive shales," in *SPE Annual Technical Conference and Exhibition*, Houston, TX, USA, October 1993.
- [6] A. Beskok and G. E. Karniadakis, "Report: a model for flows in channels, pipes, and ducts at micro and nano scales," *Microscale Thermophysical Engineering*, vol. 3, no. 1, pp. 43–77, 1999.
- [7] F. Florence, J. Rushing, K. Newsham, and T. Blasingame, "Improved permeability prediction relations for low permeability sands," in *Rocky Mountain Oil & Gas Technology Symposium*, Denver, CO, USA, April 2007.
- [8] F. Civan, "Effective correlation of apparent gas permeability in tight porous media," *Transport in Porous Media*, vol. 82, no. 2, pp. 375–384, 2010.
- [9] F. Civan, C. S. Rai, and C. H. Sondergeld, "Shale-gas permeability and diffusivity inferred by improved formulation of relevant retention and transport mechanisms," *Transport in Porous Media*, vol. 86, no. 3, pp. 925–944, 2011.
- [10] F. Civan, C. Rai, and C. Sondergeld, "Determining shale permeability to gas by simultaneous analysis of various pressure tests," *SPE Journal*, vol. 17, no. 3, pp. 717–726, 2012.
- [11] X. Xiong, D. Devegowda, G. G. Michel Villazon, R. F. Sigal, and F. Civan, "A fully-coupled free and adsorptive phase transport model for shale gas reservoirs including non-Darcy flow effects," in *SPE Annual Technical Conference and Exhibition*, San Antonio, TX, USA, October 2012.
- [12] K. Ertekin, G. A. King, and F. C. Schwerer, "Dynamic gas slippage: a unique dual-mechanism approach to the flow of gas in tight formations," *Spe Formation Evaluation*, vol. 1, no. 1, pp. 43–52, 1986.
- [13] Q. Liu, P. Shen, and P. Yang, "Pore scale network modelling of gas slippage in tight porous media," *Fluid Flow & Transport in Porous Media Mathematical and Numerical Treatment*, vol. 295, pp. 367–375, 2001.
- [14] F. Javadpour, D. Fisher, and M. Unsworth, "Nanoscale gas flow in shale gas sediments," *Journal of Canadian Petroleum Technology*, vol. 46, no. 10, 2007.
- [15] F. Javadpour, "Nanopores and apparent permeability of gas flow in mudrocks (shales and siltstone)," *Journal of Canadian Petroleum Technology*, vol. 48, no. 8, pp. 16–21, 2009.
- [16] H. Darabi, A. Ettehad, F. Javadpour, and K. Sepehrnoori, "Gas flow in ultra-tight shale strata," *Journal of Fluid Mechanics*, vol. 710, pp. 641–658, 2012.
- [17] M. R. Shahri, R. Aguilera, and A. Kantzas, "A new unified diffusion-viscous flow model based on pore level studies of tight gas formations," *SPE Journal*, vol. 18, no. 1, pp. 38–49, 2012.
- [18] J. B. Curtis, "Fractured shale-gas systems," *AAPG Bulletin*, vol. 86, pp. 1921–1938, 2002.
- [19] M. Mavor, *Barnett Shale Gas-in-Place Volume Including Sorbed and Free Gas Volume*, Fort Worth Geological Society, Texas, USA, 2003.
- [20] I. Y. Akkutlu and E. Fathi, "Multiscale gas transport in shales with local kerogen heterogeneities," *SPE Journal*, vol. 17, no. 4, pp. 1002–1011, 2012.
- [21] S. X. Liu, J. H. Zhong, X. G. Liu, L. I. Yong, Z. F. Shao, and L. Xuan, "Gas transport mechanism in tight porous media," *Natural Gas Geoscience*, vol. 25, pp. 1520–1528, 2014.
- [22] X. Cui, A. M. M. Bustin, and R. M. Bustin, "Measurements of gas permeability and diffusivity of tight reservoir rocks: different approaches and their applications," *Geofluids*, vol. 9, no. 3, 223 pages, 2009.
- [23] E. Fathi and I. Y. Akkutlu, "Nonlinear sorption kinetics and surface diffusion effects on gas transport in low-permeability formations," in *SPE Annual Technical Conference and Exhibition*, New Orleans, LA, USA, October 2009.
- [24] R. J. Ambrose, R. C. Hartman, M. D. Campos, I. Y. Akkutlu, and C. Sondergeld, "New pore-scale considerations for shale gas in place calculations," in *SPE Unconventional Gas Conference*, Pittsburgh, PA, USA, February 2010.
- [25] R. T. Yang, J. B. Fenn, and G. L. Haller, "Modification to the Higashi model for surface diffusion," *AIChE Journal*, vol. 19, no. 5, pp. 1052–1053, 1973.
- [26] Y. D. Chen and R. T. Yang, "Concentration dependence of surface diffusion and zeolitic diffusion," *AIChE Journal*, vol. 37, no. 10, pp. 1579–1582, 1991.
- [27] Y. D. Chen and R. T. Yang, "Surface and mesoporous diffusion with multilayer adsorption," *Carbon*, vol. 36, no. 10, pp. 1525–1537, 1998.
- [28] S. T. Hwang and K. Kammermeyer, "Surface diffusion in microporous media," *The Canadian Journal of Chemical Engineering*, vol. 44, no. 2, pp. 82–89, 1966.
- [29] K. Wu, X. Li, C. Wang, W. Yu, and Z. Chen, "Model for surface diffusion of adsorbed gas in nanopores of shale gas reservoirs," *Industrial & Engineering Chemistry Research*, vol. 54, pp. 3225–3236, 2015.
- [30] K. Wua, X. Li, C. Guo, and Z. Chen, "Adsorbed gas surface diffusion and bulk gas transport in nanopores of shale reservoirs with real gas effect-adsorption-mechanical coupling," in *SPE Reservoir Simulation Symposium*, Houston, TX, USA, February 2015.
- [31] K. Wu, X. Li, C. Wang, W. Yu, and Z. Chen, "Apparent permeability for gas flow in shale reservoirs coupling effects of gas diffusion and desorption," in *Proceedings of the 2nd Unconventional Resources Technology Conference*, CO, USA, 2014.

- [32] H. Y. Wang, J. M. Li, and H. L. Liu, "Progress of basic theory and accumulation law and development technology of coalbed methane," *Petroleum Exploration and Development*, vol. 31, pp. 14–16, 2004.
- [33] Z. Wang, Y. Guo, and M. Wang, "Permeability of high-Kn real gas flow in shale and production prediction by pore-scale modeling," *Journal of Natural Gas Science and Engineering*, vol. 28, pp. 328–337, 2016.
- [34] M. Wang, X. Lan, and Z. Li, "Analyses of gas flows in micro- and nanochannels," *International Journal of Heat and Mass Transfer*, vol. 51, no. 13-14, pp. 3630–3641, 2008.
- [35] Cowling, & George, T., *The Mathematical Theory of Non-uniform Gases*, Cambridge University Press, Cambridge, England, 1970.
- [36] S. A. Mohammad, J. S. Chen Jr., A. M. R. L. Robinson, and K. A. M. Gasem, "Generalized simplified local-density/peng-robinson model for adsorption of pure and mixed gases on coals," *Energy & Fuels*, vol. 23, no. 12, pp. 6259–6271, 2009.
- [37] A. Behrang and A. Kantzas, "A hybrid methodology to predict gas permeability in nanoscale organic materials; a combination of fractal theory, kinetic theory of gases and boltzmann transport equation," *Fuel*, vol. 188, pp. 239–245, 2017.
- [38] M. Zamirian, K. Aminian, E. Fathi, and S. Ameri, "A fast and robust technique for accurate measurement of the organic-rich shales characteristics under steady-state conditions," in *SPE Eastern Regional Meeting*, Charleston, WV, USA, October 2014.
- [39] A. L. Lee, M. H. Gonzalez, and B. E. Eakin, "The viscosity of natural gases," *Journal of Petroleum Technology*, vol. 18, no. 8, pp. 997–1000, 1966.
- [40] P. M. Dranchuk and H. Abou-Kassem, "Calculation of Z factors for natural gases using equations of state," *Journal of Canadian Petroleum Technology*, vol. 14, no. 3, 1975.
- [41] A. Sakhaee-Pour and S. Bryant, "Gas permeability of shale," *SPE Reservoir Evaluation & Engineering*, vol. 15, no. 4, pp. 401–409, 2012.
- [42] A. L. Myers, "Thermodynamics of adsorption in porous materials," *AICHE Journal*, vol. 48, no. 1, pp. 145–160, 2002.
- [43] D. Yang, W. Wang, W. Chen, S. Wang, and X. Wang, "Experimental investigation on the coupled effect of effective stress and gas slippage on the permeability of shale," *Scientific Reports*, vol. 7, article 44696, 2017.
- [44] F. Yang, Z. Ning, Q. Wang, R. Zhang, and B. M. Krooss, "Pore structure characteristics of lower silurian shales in the southern Sichuan basin, China: insights to pore development and gas storage mechanism," *International Journal of Coal Geology*, vol. 156, pp. 12–24, 2016.

Research Article

A Mathematical Pressure Transient Analysis Model for Multiple Fractured Horizontal Wells in Shale Gas Reservoirs

Yan Zeng ^{1,2}, Qing Wang ^{1,2}, Zhengfu Ning^{1,2} and Hongliang Sun^{1,2}

¹State Key Laboratory of Petroleum Resources and Prospecting, China University of Petroleum (Beijing), Beijing 102249, China

²Department of Petroleum Engineering, China University of Petroleum (Beijing), Beijing 102249, China

Correspondence should be addressed to Qing Wang; wq2012@cup.edu.cn

Received 26 July 2017; Revised 2 November 2017; Accepted 5 December 2017; Published 17 January 2018

Academic Editor: Ebrahim Fathi

Copyright © 2018 Yan Zeng et al. This is an open access article distributed under the Creative Commons Attribution License, which permits unrestricted use, distribution, and reproduction in any medium, provided the original work is properly cited.

Multistage fractured horizontal wells (MFHWs) have become the main technology for shale gas exploration. However, the existing models have neglected the percolation mechanism in nanopores of organic matter and failed to consider the differences among the reservoir properties in different areas. On that account, in this study, a modified apparent permeability model was proposed describing gas flow in shale gas reservoirs by integrating bulk gas flow in nanopores and gas desorption from nanopores. The apparent permeability was introduced into the macroseepage model to establish a dynamic pressure analysis model for MFHWs dual-porosity formations. The Laplace transformation and the regular perturbation method were used to obtain an analytical solution. The influences of fracture half-length, fracture permeability, Langmuir volume, matrix radius, matrix permeability, and induced fracture permeability on pressure and production were discussed. Results show that fracture half-length, fracture permeability, and induced fracture permeability exert a significant influence on production. A larger Langmuir volume results in a smaller pressure and pressure derivative. An increase in matrix permeability increases the production rate. Besides, this model fits the actual field data relatively well. It has a reliable theoretical foundation and can preferably describe the dynamic changes of pressure in the exploration process.

1. Introduction

Shale gas is known as a key resource to meet the increasing world energy demand because of its rich reserves and extensive distribution [1]. To be more specific, many pieces of research have shown that shale gas reservoirs are characterized by extremely low permeability values. Consequently, hydraulic fracturing simulations and horizontal drilling are developed for commercial exploitation. In shale gas reservoirs, the complex pore structure, macro/microfracture network distribution, and microscale reservoir properties make the gas flow characteristics become more complicated than those in conventional reservoirs. Gas flow in organic matter, natural fractures, secondary fractures, and hydraulic fractures is controlled by different mechanisms [2]. To be more specific, 20%–80% of shale gas exists in the adsorbed state on the surface of organic particulates. Desorption of adsorbed gas in organic matter affects gas transport mechanisms significantly [3, 4]. Understanding the pressure- and

rate-transient behaviors of multistage fractured horizontal wells in shale gas reservoirs is of great importance for production forecasting, well placement, and configuration optimization [5].

In recent studies [6–8], gas transport mechanisms in organic matter can be described by continuum flow, slip flow viscous flow, the Knudsen diffusion, and transition flow. Wang and Li [9] made a comparison of collision frequency in gas-gas and gas-solid interactions. They concluded that the collisions between gas molecules and the solid wall account for a large percentage of the total collisions. Therefore, the Knudsen diffusion should be considered when studying gas transport in nanopores. Darabi et al. [10] also reported that, under typical shale gas reservoir conditions, the Knudsen diffusion dominates gas transport and the contribution to cumulative production can reach 20%. Adsorbed gas desorption from the surface of organic matter also plays a significant role in gas transport [11, 12]. Swami et al. [13] developed a modified model to investigate the contribution of

adsorbed gas to the final recovery. They found that desorption of adsorbed gas can increase the pore diameter, reduce tortuosity, and cause extra slippage at the solid boundary. Yu and Sepehrnoori [14] analyzed the shale gas development history for a period of 30 years in North America and concluded that different shale samples demonstrate quite different adsorption capacities.

Mayerhofer et al. [15] studied the difference between conventional double wings symmetric fractures and hydraulic fractures of Barnett shale and were the first to propose the simulated reservoir volume (SRV) conception. In SRV, multi-stage hydraulic fracturing connects existing natural fractures, which generates a large fracture network [16]. Kucuk and Sawyer [17] firstly developed an analytical model to investigate transient pressure in shale gas reservoirs. However, the model ignored diffusion flow and the desorption effect. Lee and Brockenbrough [18] analyzed production data coming from vertical wells and developed an analytical solution to describe transient pressure. Ozkan et al. [19] proposed a dual-mechanism, that is to say, a dual-porosity horizontal well model for shale gas reservoirs, which includes hydraulic fractures, as well as the inner region and the outer region. The model can adopt the diffusive flow mechanism but fail to take adsorbed gas into consideration. Stalgorova and Mattar [20–22] extended the trilinear flow model to a five-region model for MFHWs in homogeneous shale gas reservoirs. In order to investigate the effect of natural fractures on matrix permeability, Apaydin et al. [23] combined composite blocks into an analytical trilinear flow model. Zhao et al. [24, 25] analyzed the pressure response and production performance of MFHWs in shale gas reservoirs and they introduced the source function theory to characterize SRV. Liu et al. [26] discussed the desorption and diffusion effects in the analytical model and studied the productivity-decline law. Wang [27] considered the stress sensitive effect of natural fractures and hydraulic fracture angles in the semianalytical model. His research implied that the stress sensitive effect has a significant impact on bottom hole flowing pressure.

In recent years, many general semianalytical models, considering microscopic seepage mechanisms, have been proposed with the rapid development of computer technology [24, 25, 28–30]. These models can describe predominant flow regimes for shale well but fail to consider all of the typical characteristics and possible situations in shale gas reservoirs. In the present study, a novel apparent permeability model was put forward by taking into consideration viscous flow, slip flow, transition flow, gas adsorption/desorption [31], and the poromechanical response [32, 33]. The novelty of this study concentrates on the improvement of the semianalytical model to conduct pressure- and rate-transient analysis in SRV, by considering microscale percolation mechanisms and heterogeneity. The rest of this study can be described in the following way. In Section 2, the apparent permeability model for gas transport in shale nanopores is introduced. The semianalytical model for MFHWs in a heterogeneous shale gas reservoir, by considering microscale percolation mechanisms in a dual-porosity formation, is introduced in Section 3. Log-log dimension pressure, dimension pressure derivative, and production type curves are plotted firstly,

and then a sensitivity analysis of formation parameters is conducted in Section 4. An actual field case is studied in Section 5. Finally, some conclusions are drawn in Section 6.

2. Apparent Permeability Model for Gas Transport in Shale Nanopores

2.1. Viscous Flow. The total shale gas flux is composed of a viscous flow flux and a Knudsen diffusion flux component. Viscous flow is strongly prominent when the short molecule free path is far less than the pore diameter. In other words, the transport mechanism is governed by viscous flow in macropores (where the pore diameter > 50 nm). The Hagen-Poiseuille equation can describe the molar flux [34] as stated below:

$$J_V = -\frac{\phi}{\tau} \frac{r^2 P}{8\mu RT} \frac{dP}{dl}, \quad (1)$$

where J_V is the viscous flow flux, mol/(m²*s); ϕ is porosity, dimensionless; τ is tortuosity, dimensionless; r is the pore radius, m; μ is viscosity, Pa*s; R is the universal gas constant, J/(mol*K); T is temperature, K; P is pressure, Pa; and l is the shale gas transport distance, m.

Gas viscosity gradually deviates from the traditional viscosity definition for high Knudsen numbers. Karniadakis et al. [35] modified the viscosity definition in the Knudsen layer by considering the rarefaction effect.

$$\mu_{\text{eff}} = \frac{1}{1 + \alpha \text{Kn}} \mu, \quad (2)$$

where μ_{eff} is the viscosity considering rarefaction effect, Pa*s; α is the rarefaction coefficient, dimensionless; and Kn is the Knudsen number, dimensionless.

According to the Darcy equation, the apparent permeability of viscous flow can be expressed as [36]:

$$\begin{aligned} K_v &= \frac{J_{v\text{-eff}} \mu V_{\text{std}}}{dP/dl} = (1 + \alpha \text{Kn}) \frac{\phi}{\tau} \frac{r^2 P V_{\text{std}}}{8RT} \\ &= (1 + \alpha \text{Kn}) K_{\infty}, \end{aligned} \quad (3)$$

where K_v is the apparent permeability, taking into account the effect of rarefaction, m²; V_{std} is the gas mole volume at standard conditions, 22.414 * 10⁻³ m³/mol; and K_{∞} is the permeability of viscous flow, m².

2.2. The Knudsen Diffusion. When there is shale gas transport through micropores under low pressure, the molecule free path is long and equal to the pore diameter. The Knudsen diffusion is prominent because collisions between molecules and the micropores wall are more frequent than the intermolecular collisions. The flux of the Knudsen diffusion can be expressed as [34]

$$J_K = -\frac{\phi}{\tau} \frac{MD_K}{RT} \frac{\partial C}{\partial l}, \quad (4)$$

where J_K is the Knudsen diffusion flux, mol/(m²*s); D_K is the Knudsen diffusion coefficient, m²/s; and C is the gas

concentration, m^3/mol . The Knudsen diffusion coefficient is obtained as

$$D_K = \frac{2}{3} r \sqrt{\frac{8RT}{\pi M}}, \quad (5)$$

where M is the gas molar mass, kg/mol . The rough wall has a significant effect on the Knudsen diffusion. Darabi et al. [10] proposed a function to describe the roughness effect as follows:

$$D_{\text{eff}} = \delta^{D_f-2} D_K = \left(\frac{\bar{\lambda}}{2r} \right)^{D_f-2} D_K, \quad (6)$$

where D_{eff} is the Knudsen diffusion coefficient which takes into consideration the roughness effect, m^2/s ; $\bar{\lambda}$ is the mean free path of gas molecules, m ; and D_f is the fractal dimension of the rough wall, dimensionless.

By combining (4) and (6), the apparent permeability of the Knudsen diffusion can be obtained and written as follows:

$$K_K = \frac{J_{K\text{-eff}} \mu V_{\text{std}}}{M d C / d l} = \frac{2}{3} \frac{\phi}{\tau} r \mu \frac{V_{\text{std}}}{M} \left(\frac{\bar{\lambda}}{2r} \right)^{D_f-2} \sqrt{\frac{8M}{\pi RT}}. \quad (7)$$

2.3. Weight Factor. In the actual shale gas reservoirs, different transport mechanisms exist at the same time. Therefore, the total shale gas flux should be a weighted summation of the viscous flow flux and the Knudsen diffusion flux, based on their different contributions. The weight factors of the viscous flow and the Knudsen diffusion flow are defined as the ratios of intermolecular collisions and molecular/pore-wall collisions to total collisions, respectively. Based on the definitions for a gas molecule free path [11] and collision numbers [37], the weight factors of viscous flow and Knudsen diffusion can be approximated as follows:

$$w_V = w = \frac{1}{1 + \text{Kn}/2} \quad (8)$$

$$w_K = 1 - w = \frac{1}{1 + 2/\text{Kn}}.$$

Therefore, the total apparent permeability in nanopores is

$$K = w K_V + (1 - w) K_K$$

$$= w (1 + \alpha \text{Kn}) K_{\infty}$$

$$+ (1 - w) \frac{2}{3} \frac{\phi}{\tau} r \mu \frac{V_{\text{std}}}{M} \left(\frac{\bar{\lambda}}{2r} \right)^{D_f-2} \sqrt{\frac{8M}{\pi RT}}. \quad (9)$$

With a decrease in pressure, the gas molecule free path increases immediately. The weight factor of the Knudsen diffusion also increases. The piece of research carried out by Wu et al. [38] showed that, under the 10 nm radius condition, viscous flow dominates when the pressure is larger than 4.02×10^5 Pa; otherwise, the Knudsen diffusion dominates.

2.4. Sorption-Induced Swelling Response. Organic matter is described by weak strength and strong sensitivity to stress

change. With an increase in reservoir pressure, adsorbed gas begins to desorb. Gas desorption results in shrinkage of the organic matrix and to an increased effective hydraulic diameter [39]. According to the solid deformation theory [40] and the Langmuir isotherm equation [41], the relationship between the degree of solid deformation and the reservoir pressure can be written as follows:

$$\Delta \varepsilon = \frac{V_L \rho_s RT}{E V_{\text{std}}} [\ln(P_L + P_{\text{ini}}) - \ln(P_L + P)]$$

$$+ c_P (P_{\text{ini}} - P), \quad (10)$$

where $\Delta \varepsilon$ is the solid deformation degree, dimensionless; V_L is the Langmuir volume, m^3/kg ; ρ_s is the density of the shale matrix, kg/m^3 ; E is the shale matrix Young modulus, Pa; P_L is the Langmuir pressure, Pa; P_{ini} is the initial pressure, Pa; and c_P is the rock compressibility, Pa^{-1} .

Meanwhile, based on Seidle's model [42], the approximation relation between the porosity and the solid deformation degree is given by

$$\frac{\phi}{\phi_{\text{ini}}} = 1 + \left(1 + \frac{2}{\phi_{\text{ini}}} \right) \Delta \varepsilon. \quad (11)$$

Assume that the pore volumes are proportional to the gas flow channels. In accordance with the capillary model, the effective hydraulic diameter can be obtained as

$$r_{\text{eff}} = r \sqrt{1 + \left(1 + \frac{2}{\phi_{\text{ini}}} \right) \left[\frac{V_L \rho_s RT}{E V_{\text{std}}} \ln \frac{P_L + P_{\text{ini}}}{P_L + P} + c_P (P_{\text{ini}} - P) \right]}. \quad (12)$$

2.5. Gas Adsorption/Desorption. Because of the large surface area and oil-wet characteristic, nanopores have a strong adsorbed gas capacity. The mass balance equation, which considers the adsorbed gas, can be expressed as

$$\rho c_g \phi \left(1 + \frac{1 - \phi}{\phi} \frac{\partial V}{\partial \rho} \right) \frac{\partial P}{\partial t} = \frac{1}{r} \frac{\partial}{\partial r} \left(r \frac{K}{\mu} \rho \frac{\partial P}{\partial r} \right), \quad (13)$$

where ρ is the shale gas density, kg/m^3 ; c_g is the gas compressibility, Pa^{-1} ; and V is the mass of adsorbed gas per unit volume of shale, kg/m^3 . The apparent permeability, which considers desorption of adsorbed gas, can be expressed as

$$K_{\text{app}} = \left(1 + \frac{1 - \phi}{\phi} \frac{\partial V}{\partial \rho} \right) K. \quad (14)$$

Cui et al. [12] defined the effective adsorption porosity as

$$\phi_{\text{ad}} = (1 - \phi) \frac{\partial V}{\partial \rho}. \quad (15)$$

According to the Langmuir isotherm equation, the effective adsorption porosity can be expressed as

$$\phi_{\text{ad}} = \frac{\rho_s M}{V_{\text{std}}} \frac{1 - \phi}{\rho c_g} \frac{V_m P_L}{(P_L + P)^2}. \quad (16)$$

- (2) Natural fracture permeability is stress-dependent and shale gas flow in the matrix is driven by concentration difference.
- (3) The initial pressure throughout the reservoir is uniform.
- (4) Hydraulic fractures penetrate the entire pay formation. Fracture interference is ignored. After SRV, large fracture networks can be generated in region 2 and it has higher natural fracture permeability compared to the other regions.
- (5) The shale gas flow in the reservoir is considered to be an isothermal flow and the effect of gravity and capillary pressure are negligible.
- (6) Nonsimulated areas are described by a dual-porosity system consisting of a shale matrix and natural fractures.
- (7) The only route for shale gas to reach the horizontal wellbore is through hydraulic fractures. The flow rate of MFHW is the sum of the flow rate from every hydraulic fracture.

3.2. Mathematical Model. According to the mass conservation equation, the motion equation, and the state equation, the partial differential formulas for shale gas flow in a matrix system and a fracture system can be obtained as follows [19, 27]:

$$\frac{1}{r_{mD}^2} \frac{\partial}{\partial r_{mD}} \left(r_{mD}^2 \frac{\partial \psi_{mD}}{\partial r_{mD}} \right) = \frac{1}{\eta_{mD}} \frac{\partial \psi_{mD}}{\partial t_D} \quad (18)$$

$$\frac{\partial^2 \psi_{fD}}{\partial x_D^2} - \beta_D \left(\frac{\partial \psi_{fD}}{\partial x_D} \right)^2 = \exp(\beta_D \psi_{fD}) \cdot \left(\frac{2K_{\text{mapp,ave}} h_{\text{ref}}^2}{K_{f_i} h_f r_m} \frac{\partial \psi_{mD}}{\partial r_{mD}} \Big|_{r_{mD}=1} + \frac{1}{\eta_{fD}} \frac{\partial \psi_{fD}}{\partial t_D} \right), \quad (19)$$

where β_D is a characteristic dimensionless parameter of stress sensitivity and relates to the permeability modulus γ . β is defined as $\beta = (\mu Z / 2P) \gamma$, where $K_f = K_{f_i} \exp(-\gamma \Delta P_f)$.

Pedrosa's substitution [43] is used to weaken the nonlinearity of (19). By setting $\psi_{fD} = (1/\gamma_D) \ln(1 - \gamma_D \xi_D)$, (19) can be simplified into

$$\frac{\partial^2 \xi_{fD}}{\partial x_D^2} = \frac{2K_{\text{mapp,ave}} h_{\text{ref}}^2}{K_{f_i} h_f r_m} \frac{\partial \psi_{mD}}{\partial r_{mD}} \Big|_{r_{mD}=1} + \frac{1}{\eta_{fD}} \frac{\partial \xi_{fD}}{\partial t_D}. \quad (20)$$

To solve (18) and (20), these two equations were converted to the Laplace domain. And then the definite boundary continuity is introduced to develop an integral seepage flow differential equation. The final equation can be written as

$$\frac{\partial^2 \bar{\psi}_{fD}}{\partial x_D^2} = f(s) s \bar{\psi}_{fD}, \quad (21)$$

where $f(s) = 1/\eta_{fD} - (\lambda/5s)[1 - \sqrt{s/\eta_{mD}} \coth \sqrt{s/\eta_{mD}}]$.

A series of variables and dimensionless variables are defined in Table 1.

3.2.1. Region 7. In this upper-reservoir region, the governing diffusivity equation for shale gas flow in the z -direction becomes

$$\frac{\partial^2 \bar{\psi}_{fD7}}{\partial z_D^2} - f_7(s) s \bar{\psi}_{fD7} = 0, \quad (22)$$

where

$$f_7(s) = \frac{1}{\eta_{fD7}} - \frac{\lambda_7}{5s} \left[1 - \sqrt{\frac{s}{\eta_{mD7}}} \coth \sqrt{\frac{s}{\eta_{mD7}}} \right]. \quad (23)$$

At the top of the reservoir ($z = z_2$), the boundary condition is no-flow:

$$\frac{\partial \bar{\psi}_{fD7}}{\partial z_D} \Big|_{z_D=z_{2D}} = 0. \quad (24)$$

On the interfaces ($z = z_1$) of regions 7 and 3 and regions 7 and 5, pressure continuity condition can be obtained as

$$\bar{\psi}_{fD7} \Big|_{z_D=z_{1D}} = \bar{\psi}_{fD3} \Big|_{z_D=z_{1D}} = \bar{\psi}_{fD5} \Big|_{z_D=z_{1D}}. \quad (25)$$

Equation (22) is solved simultaneously with (24) and (25). The final solution for (22) can be given as

$$\begin{aligned} \frac{\partial \bar{\psi}_{fD7}}{\partial z_D} \Big|_{z_D=z_{1D}} &= \sqrt{f_7(s) s} \\ &\cdot \tanh \left[\sqrt{f_7(s) s} (z_{1D} - z_{2D}) \right] \bar{\psi}_{fD3} \Big|_{z_D=z_{1D}} \\ &= \sqrt{f_7(s) s} \tanh \left[\sqrt{f_7(s) s} (z_{1D} - z_{2D}) \right] \\ &\cdot \bar{\psi}_{fD5} \Big|_{z_D=z_{1D}}. \end{aligned} \quad (26)$$

3.2.2. Region 6. Consistent with region 7, the governing diffusivity equation for shale gas flow in the z -direction becomes

$$\frac{\partial^2 \bar{\psi}_{fD6}}{\partial z_D^2} - f_6(s) s \bar{\psi}_{fD6} = 0, \quad (27)$$

where

$$f_6(s) = \frac{1}{\eta_{fD6}} - \frac{\lambda_6}{5s} \left[1 - \sqrt{\frac{s}{\eta_{mD6}}} \coth \sqrt{\frac{s}{\eta_{mD6}}} \right]. \quad (28)$$

The boundary condition at the top of the reservoir ($z = z_2$) is

$$\frac{\partial \bar{\psi}_{fD6}}{\partial z_D} \Big|_{z_D=z_{2D}} = 0. \quad (29)$$

The boundary conditions on the interfaces of regions 6 and 2 and regions 6 and 4 are

$$\bar{\psi}_{fD6} \Big|_{z_D=z_{1D}} = \bar{\psi}_{fD2} \Big|_{z_D=z_{1D}} = \bar{\psi}_{fD5} \Big|_{z_D=z_{1D}}. \quad (30)$$

TABLE 1: Definitions of variables.

Variable	Expression	Dimensionless expression		
Pseudo-pressure, psi^2/cp	$\psi = \int_{P_{\text{ini}}}^P \frac{2P}{\mu Z} dP$	$\psi_D = \frac{K_{\text{ref}} h_{\text{ref}}}{2704 q_{\text{sc}} T} (\psi_{\text{ini}} - \psi)$		
Permeability modulus factor, $\text{psi}^{-1} \cdot \text{hr}$	$\beta = \frac{\mu Z}{38P} \gamma$	$\beta_D = \frac{2704 q_{\text{sc}} T}{K_{\text{ref}} h_{\text{ref}}} \beta$		
Diffusivity, ft^2/hr	$\eta_{\text{ref}} = \frac{2.637 \times 10^{-4} K_{\text{ref}}}{\phi_{\text{ref}} c_{\text{ref}} \mu_{\text{ref}}}$	$\eta_{mD} = \frac{\eta_m}{\eta_{\text{ref}}}$		
	$\eta_m = \frac{2.637 \times 10^{-4} K_{m,\text{ave}}}{\phi_m a_{\text{ave}} c_{m,\text{ave}} \mu_{m,\text{ave}}}$	$\eta_{fD} = \frac{\eta_f}{\eta_{\text{ref}}}$		
	$\eta_f = \frac{2.637 \times 10^{-4} K_f}{\phi_f c_{f,\text{ave}} \mu_{f,\text{ave}}}$	$\eta_{FD} = \frac{\eta_F}{\eta_{\text{ref}}}$		
	$\eta_F = \frac{2.637 \times 10^{-4} K_F}{\phi_F c_{F,\text{ave}} \mu_{F,\text{ave}}}$			
Adsorption coefficient, dimensionless	$a_{\text{ave}} = \frac{c_{m,\text{ave}} + ((1 - \phi_m)/\phi_m) (TP_{\text{sc}} Z_{\text{ave}}/T_{\text{sc}} P_{m,\text{ave}} Z_{\text{sc}}) (V_L P_L / (P_L + P_{m,\text{ave}}))^2}{c_{m,\text{ave}}}$			
Time, hr		$t_D = \frac{\eta_{\text{ref}}}{h_{\text{ref}}^2} t$		
Length, ft	$x_{1D} = \frac{x_f}{h_{\text{ref}}}$	$x_{eD} = \frac{x_e}{h_{\text{ref}}}$	$y_{1D} = \frac{y_1}{h_{\text{ref}}}$	$y_{2D} = \frac{y_2}{h_{\text{ref}}}$
	$z_{1D} = \frac{h_F}{2h_{\text{ref}}}$	$z_{2D} = \frac{h}{h_{\text{ref}}}$	$w_D = \frac{w_F}{h_{\text{ref}}}$	$r_{mD} = \frac{r}{r_m}$

The solution for (27) can be given as

$$\begin{aligned} \left. \frac{\partial \bar{\psi}_{fD6}}{\partial z_D} \right|_{z_D=z_{1D}} &= \sqrt{f_6(s)} s \\ &\cdot \tanh \left[\sqrt{f_6(s)} s (z_{1D} - z_{2D}) \right] \bar{\psi}_{fD2} \Big|_{z_D=z_{1D}} \\ &= \sqrt{f_6(s)} s \tanh \left[\sqrt{f_6(s)} s (z_{1D} - z_{2D}) \right] \\ &\cdot \bar{\psi}_{fD4} \Big|_{z_D=z_{1D}}. \end{aligned} \quad (31)$$

3.2.3. *Region 5.* In this region, shale gas flow takes place in the x -direction and the z -direction. So the governing diffusivity equation for region 5 is

$$\frac{\partial^2 \bar{\psi}_{fD5}}{\partial x_D^2} + \frac{\partial^2 \bar{\psi}_{fD5}}{\partial z_D^2} - f_5(s) s \bar{\psi}_{fD5} = 0, \quad (32)$$

where

$$f_5(s) = \frac{1}{\eta_{fD5}} - \frac{\lambda_5}{5s} \left[1 - \sqrt{\frac{s}{\eta_{mD5}}} \coth \sqrt{\frac{s}{\eta_{mD5}}} \right]. \quad (33)$$

Along the horizontal well ($z = 0$), there is a no-flow boundary:

$$\left. \frac{\partial \bar{\psi}_{fD5}}{\partial z_D} \right|_{z_D=0} = 0. \quad (34)$$

Flux across the interface of regions 5 and 7 ($z = z_1$) is continuous; therefore,

$$K_{f5} \left. \frac{\partial \bar{\psi}_{fD5}}{\partial z_D} \right|_{z_D=z_{1D}} = K_{f7} \left. \frac{\partial \bar{\psi}_{fD7}}{\partial z_D} \right|_{z_D=z_{1D}}. \quad (35)$$

Substituting (34) and (35) into (32), each of its terms from 0 to z_{1D} is integrated with respect to z_D . The governing diffusivity can be simplified as

$$\frac{\partial^2 \bar{\psi}_{fD5}}{\partial x_D^2} + \frac{K_{f7}}{K_{f5} z_{1D}} \left. \frac{\partial \bar{\psi}_{fD7}}{\partial z_D} \right|_{z_D=z_{1D}} - f_5(s) s \bar{\psi}_{fD5} = 0. \quad (36)$$

In this region, shale gas flow in the x -direction and with a closed boundary condition ($x = x_e$) is expressed as

$$\left. \frac{\partial \bar{\psi}_{fD5}}{\partial x_D} \right|_{x_D=x_eD} = 0. \quad (37)$$

Pressure continuity condition between regions 5 and 3 (at $x = x_1$) is expressed as

$$\bar{\psi}_{fD5} \Big|_{x_D=x_{1D}} = \bar{\psi}_{fD2} \Big|_{x_D=x_{1D}}. \quad (38)$$

By solving (36), the solution can be obtained as

$$\begin{aligned} \left. \frac{\partial \bar{\psi}_{fD5}}{\partial x_D} \right|_{x_D=x_{1D}} &= \sqrt{\alpha_5} \tanh \left[\sqrt{\alpha_5} (x_{1D} - x_{eD}) \right] \bar{\psi}_{fD3} \Big|_{x_D=x_{1D}}, \end{aligned} \quad (39)$$

where

$$\begin{aligned} \alpha_5 &= f_5(s) s \\ &- \frac{K_{f7}}{K_{f5} z_{1D}} \sqrt{f_7(s) s} \tanh \left[\sqrt{f_7(s) s} (z_{1D} - z_{2D}) \right]. \end{aligned} \quad (40)$$

3.2.4. *Region 4.* In a similar way, shale gas flow in this region takes place in the x -direction and the z -direction. The governing diffusivity equation for region 4 is

$$\frac{\partial^2 \bar{\psi}_{fD4}}{\partial x_D^2} + \frac{\partial^2 \bar{\psi}_{fD4}}{\partial z_D^2} - f_4(s) s \bar{\psi}_{fD4} = 0, \quad (41)$$

where

$$f_4(s) = \frac{1}{\eta_{fD4}} - \frac{\lambda_4}{5s} \left[1 - \sqrt{\frac{s}{\eta_{mD4}}} \coth \sqrt{\frac{s}{\eta_{mD4}}} \right]. \quad (42)$$

The same method is also used in region 5, where the governing diffusivity equation can be simplified as

$$\frac{\partial^2 \bar{\psi}_{fD4}}{\partial x_D^2} + \frac{K_{f4}}{K_{f6} z_{1D}} \frac{\partial \bar{\psi}_{fD4}}{\partial z_D} \Big|_{z_D=z_{1D}} - f_4(s) s \bar{\psi}_{fD4} = 0. \quad (43)$$

No-flow condition at the outer-reservoir boundary ($x = x_e$) is given as

$$\frac{\partial \bar{\psi}_{fD4}}{\partial x_D} \Big|_{x_D=x_eD} = 0. \quad (44)$$

On the interface of regions 4 and 2, the boundary condition is

$$\bar{\psi}_{fD4} \Big|_{x_D=x_{1D}} = \bar{\psi}_{fD2} \Big|_{x_D=x_{1D}}. \quad (45)$$

The solution for (41) is given as

$$\begin{aligned} &\frac{\partial \bar{\psi}_{fD4}}{\partial x_D} \Big|_{x_D=x_{1D}} \\ &= \sqrt{\alpha_4} \tanh \left[\sqrt{\alpha_4} (x_{1D} - x_{eD}) \right] \bar{\psi}_{fD2} \Big|_{x_D=x_{1D}}, \end{aligned} \quad (46)$$

where

$$\begin{aligned} \alpha_4 &= f_4(s) s \\ &- \frac{K_{f6}}{K_{f4}} \sqrt{f_6(s) s} \tanh \left[\sqrt{f_6(s) s} (z_{1D} - z_{2D}) \right]. \end{aligned} \quad (47)$$

3.2.5. *Region 3.* This region is adjacent to regions 5 and 7, so shale gas flow direction takes place along the x -direction, y -direction, and z -direction. The governing diffusivity equation becomes

$$\frac{\partial^2 \bar{\psi}_{fD3}}{\partial y_D^2} + \frac{\partial^2 \bar{\psi}_{fD3}}{\partial x_D^2} + \frac{\partial^2 \bar{\psi}_{fD3}}{\partial z_D^2} - f_3(s) s \bar{\psi}_{fD3} = 0, \quad (48)$$

where

$$f_3(s) = \frac{1}{\eta_{fD3}} - \frac{\lambda_3}{5s} \left[1 - \sqrt{\frac{s}{\eta_{mD3}}} \coth \sqrt{\frac{s}{\eta_{mD3}}} \right]. \quad (49)$$

For the x -direction, the boundary condition used is a no-flow condition for a horizontal well ($z = 0$) and a flux continuity condition is used on the interface of regions 5 and 3 ($x = x_1$):

$$\begin{aligned} &\frac{\partial \bar{\psi}_{fD3}}{\partial x_D} \Big|_{x_D=0} = 0 \\ &K_{f3} \frac{\partial \bar{\psi}_{fD3}}{\partial x_D} \Big|_{x_D=x_{1D}} = K_{f5} \frac{\partial \bar{\psi}_{fD5}}{\partial x_D} \Big|_{x_D=x_{1D}}. \end{aligned} \quad (50)$$

For the z -direction, (51) can be obtained:

$$\begin{aligned} &\frac{\partial \bar{\psi}_{fD3}}{\partial z_D} \Big|_{z_D=0} = 0 \\ &K_{f3} \frac{\partial \bar{\psi}_{fD3}}{\partial z_D} \Big|_{z_D=z_{1D}} = K_{f7} \frac{\partial \bar{\psi}_{fD7}}{\partial z_D} \Big|_{z_D=z_{1D}}. \end{aligned} \quad (51)$$

By substituting (50) and (51) into (48), the final governing diffusivity equation becomes

$$\begin{aligned} &\frac{\partial^2 \bar{\psi}_{fD3}}{\partial y_D^2} + \frac{K_{f7}}{K_{f3} z_{1D}} \frac{\partial \bar{\psi}_{fD7}}{\partial z_D} \Big|_{z_D=z_{1D}} \\ &+ \frac{K_{f5}}{K_{f3} x_{1D}} \frac{\partial \bar{\psi}_{fD5}}{\partial x_D} \Big|_{x_D=x_{1D}} - f_3(s) s \bar{\psi}_{fD3} = 0. \end{aligned} \quad (52)$$

Between two fractures, there is a no-flow boundary ($y = y_2$):

$$\frac{\partial \bar{\psi}_{fD3}}{\partial y_D} \Big|_{y_D=y_{2D}} = 0. \quad (53)$$

On the interface of regions 3 and 2, the pressure continuity condition is written as

$$\bar{\psi}_{fD3} \Big|_{y_D=y_{1D}} = \bar{\psi}_{fD2} \Big|_{y_D=y_{1D}}. \quad (54)$$

The solution for (48) is given as

$$\begin{aligned} &\frac{\partial \bar{\psi}_{fD3}}{\partial y_D} \Big|_{y_D=y_{1D}} \\ &= \sqrt{\alpha_3} \tanh \left[\sqrt{\alpha_3} (y_{1D} - y_{2D}) \right] \bar{\psi}_{fD2} \Big|_{y_D=y_{1D}}, \end{aligned} \quad (55)$$

where

$$\begin{aligned} \alpha_3 &= f_3(s) s \\ &- \frac{K_{f7}}{K_{f3} z_{1D}} \sqrt{f_7(s) s} \tanh \left[\sqrt{f_7(s) s} (z_{1D} - z_{2D}) \right] \\ &- \frac{K_{f5}}{K_{f3} x_{1D}} \sqrt{\alpha_5} \tanh \left[\sqrt{\alpha_5} (x_{1D} - x_{eD}) \right]. \end{aligned} \quad (56)$$

3.2.6. *Region 2.* Similarly, as region 2 is adjacent to hydraulic fracture, the governing diffusivity equation is

$$\frac{\partial^2 \bar{\psi}_{fD2}}{\partial y_D^2} + \frac{\partial^2 \bar{\psi}_{fD2}}{\partial x_D^2} + \frac{\partial^2 \bar{\psi}_{fD2}}{\partial z_D^2} - f_2(s) s \bar{\psi}_{fD2} = 0. \quad (57)$$

Consistent with region 3, the simplified equation can be written as

$$\begin{aligned} \frac{\partial^2 \bar{\psi}_{fD2}}{\partial y_D^2} + \frac{K_{f6}}{K_{f2} z_{1D}} \frac{\partial \bar{\psi}_{fD6}}{\partial z_D} \Big|_{z_D=z_{1D}} \\ + \frac{K_{f4}}{K_{f2} x_{1D}} \frac{\partial \bar{\psi}_{fD4}}{\partial x_D} \Big|_{x_D=x_{1D}} - f_2(s) s \bar{\psi}_{fD2} = 0, \end{aligned} \quad (58)$$

where

$$f_2(s) = \frac{1}{\eta_{fD2}} - \frac{\lambda_2}{5s} \left[1 - \sqrt{\frac{s}{\eta_{mD2}}} \coth \sqrt{\frac{s}{\eta_{mD2}}} \right]. \quad (59)$$

At the interface of regions 2 and 3, the boundary condition is characterized by flux continuity:

$$K_{f2} \frac{\partial \bar{\psi}_{fD2}}{\partial y_D} \Big|_{y_D=y_{1D}} = K_{f3} \frac{\partial \bar{\psi}_{fD3}}{\partial y_D} \Big|_{y_D=y_{1D}}. \quad (60)$$

And between the hydraulic fracture level and region 2, the boundary condition is

$$\bar{\psi}_{fD2} \Big|_{y_D=w_D/2} = \bar{\psi}_{FD} \Big|_{y_D=w_D/2}. \quad (61)$$

Solving (58) to (61),

$$\frac{\partial \bar{\psi}_{fD2}}{\partial y_D} \Big|_{y_D=w_D/2} = -\beta_2 \bar{\psi}_{FD} \Big|_{y_D=w_D/2}, \quad (62)$$

where

$$\begin{aligned} \beta_2 &= \sqrt{\alpha_2} \\ &\cdot \frac{\exp(-\sqrt{\alpha_2}(w_D/2)) - \beta_1 \exp(\sqrt{\alpha_2}(w_D/2))}{\exp(-\sqrt{\alpha_2}(w_D/2)) + \beta_1 \exp(\sqrt{\alpha_2}(w_D/2))} \\ \beta_1 &= \exp(-2\sqrt{\alpha_2} y_{1D}) \\ &\cdot \frac{K_{f2} \sqrt{\alpha_2} + K_{f3} \sqrt{\alpha_3} \tanh[\sqrt{\alpha_3}(y_{1D} - y_{2D})]}{K_{f2} \sqrt{\alpha_2} - K_{f3} \sqrt{\alpha_3} \tanh[\sqrt{\alpha_3}(y_{1D} - y_{2D})]} \end{aligned} \quad (63)$$

$$\begin{aligned} \alpha_2 &= f_2(s) s - \frac{K_{f6}}{K_{f2} z_{1D}} \sqrt{f_6(s) s} \\ &\cdot \tanh \left[\sqrt{f_6(s) s} (z_{1D} - z_{2D}) \right] - \frac{K_{f4}}{K_{f2} x_{1D}} \sqrt{\alpha_4} \\ &\cdot \tanh \left[\sqrt{\alpha_4} (x_{1D} - x_{eD}) \right]. \end{aligned}$$

3.2.7. *Region 1.* In this region, the diffusivity equation is given by

$$\frac{\partial^2 \bar{\psi}_{pFD}}{\partial x_D^2} + \frac{2}{F_{CD}} \frac{\partial \bar{\psi}_{fD2}}{\partial y_D} \Big|_{y_D=w_D/2} - \frac{s}{\eta_{FD}} \bar{\psi}_{pFD} = 0, \quad (64)$$

where $F_{CD} = K_F w_D / K_{f2}$. The boundary condition can be stated by the expressions:

$$\begin{aligned} \frac{\partial \bar{\psi}_{pFD}}{\partial x_D} \Big|_{x_D=x_{1D}} &= 0 \\ \frac{\partial \bar{\psi}_{pFD}}{\partial x_D} \Big|_{x_D=x_{1D}} &= -\frac{\pi}{F_{CD} s}. \end{aligned} \quad (65)$$

The solution can be obtained:

$$\bar{\psi}_{pFD} = \frac{\pi \cosh[\sqrt{\alpha_F}(x_D - x_{1D})]}{\sqrt{\alpha_F} F_{CD} s \sinh(\sqrt{\alpha_F} x_{1D})}, \quad (66)$$

where

$$\alpha_F = \frac{2\beta_2}{F_{CD}} + \frac{s}{\eta_{FD}}. \quad (67)$$

Assuming that pressure distribution along the horizontal well is uniform, the dimensionless down-hole pressure can be solved by setting $x_D = 0$ [44]:

$$\bar{\psi}_{wD} = \bar{\psi}_{pFD} \Big|_{x_D=0} = \frac{\pi}{\sqrt{\alpha_F} F_{CD} s \tanh(\sqrt{\alpha_F} x_{1D})}. \quad (68)$$

Shale gas flow in hydraulic fractures is not completely linear. The nonlinear streamlines result in an additional pressure drop. Mukherjee and Economides [45] presented a formulation to take this additional pressure drop into consideration.

$$S_c = \frac{K_{f1} h}{K_F w_f} \left[\ln \left(\frac{h}{2r_w} \right) - \frac{\pi}{2} \right]. \quad (69)$$

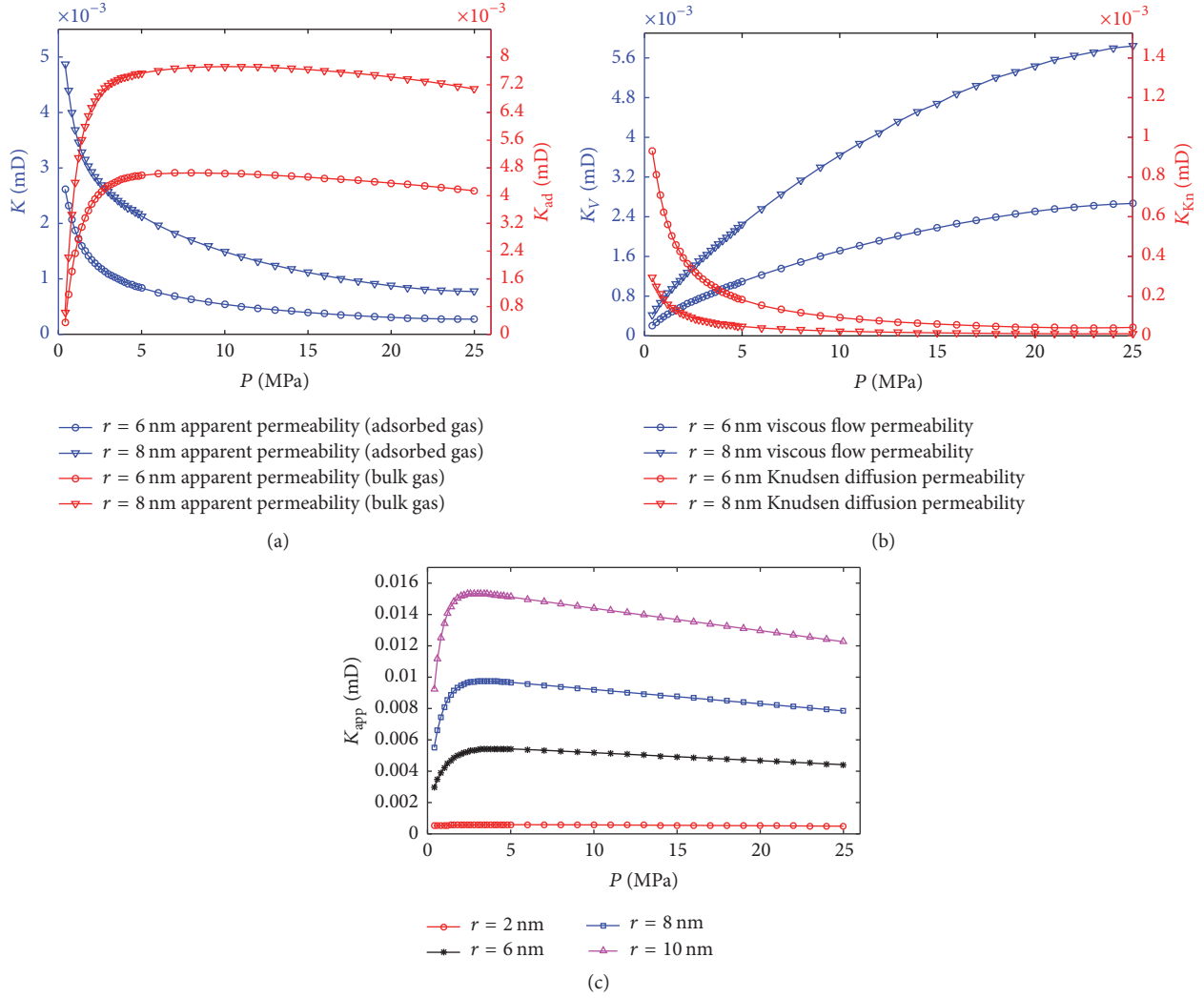


FIGURE 2: Variation of $K_{app,ad}$, K_v , $K_{app,Kn}$, and $K_{app,t}$ with average pressure.

Based on the Duhamel principle and the superposition principle, the dimensionless flowing bottom hole pressure (FHBP), which takes into consideration the wellbore storage effect and the skin effect, can be expressed as [30]

$$\bar{\psi}_{wD}(S_c, C_D) = \frac{S_c + s\bar{\psi}_{wD}}{s[1 + C_D s(s\bar{\psi}_{wD} + S_c)]}. \quad (70)$$

The FHBP for MFHWs, when considering the stress sensitivity effect, can be obtained as

$$\bar{\psi}_{wD}(S_c, C_D, t_D) = -\frac{1}{\gamma_D} \ln [1 - \gamma_D \bar{\psi}_{wD}(S_c, C_D)]. \quad (71)$$

The relationship between the dimensionless rate under the condition of constant pressure and dimensionless pressure caused by the constant rate is described as [46]

$$\bar{q}_D = \frac{1}{s^2 \bar{\psi}_{wD}}. \quad (72)$$

4. Discussion and Analysis

4.1. Apparent Permeability in the Shale Matrix. Figure 2 shows the variation of the apparent permeabilities against the average pressure. The input parameters are listed in Table 2. Based on Figure 2, one can observe that, in the early period, with a decrease of the average pressure, the bulk permeability $K_{app,bulk}$ decreases dramatically, but the apparent permeability caused by gas desorption $K_{app,ad}$ increases greatly. In the later period, $K_{app,bulk}$ increases slightly with an increase of the pressure. $K_{app,ad}$ also increases in a similar way with an increase in pressure. The explanation is that, at high pressure, the Knudsen diffusion increases significantly. As can be seen in Figure 2, viscous flow dominates at high pressure and the Knudsen diffusion dominates at low pressure. Figure 2 also indicates that the pore diameter has a great impact on the apparent permeability. With a decrease of the pressure, nanopores become larger and larger under the influence of matrix shrinkage, so the apparent permeability increases gradually. However, there is an inflection point between the apparent permeability and the average pressure.

TABLE 2: Basic parameters.

Variable	Value
ϕ , dimensionless	0.05
r , m	10^{-8}
P_{ini} , MPa	25
T , K	333
k_B , J/K	$1.38 * 10^{-23}$
ρ_s , t/m ³	2.56
c_p , MPa ⁻¹	$4.35 * 10^{-4}$
V_L , m ³ /t	18.66
E , MPa	4000
τ , dimensionless	4.3
μ , Pa*s	$1.75 * 10^{-5}$
P_{fim} , MPa	1
M , kg/mol	0.016
V_{std} , m ³ /mol	$22.4 * 10^{-3}$
ρ_g , t/m ³	0.085
c_g , MPa ⁻¹	$6.89 * 10^{-2}$
P_L , MPa	2.72
α , dimensionless	2.0

TABLE 3: Model parameters.

Variable	Value
Reservoir size in x -direction, x_e , ft	500
Distance to no-flow boundary, y_2 , ft	250
Reservoir thickness, h , ft	250
Fracture width, w_f , ft	0.01
Reservoir temperature, T , K	333
Gas volumetric factor, B_g	0.004
Initial matrix compressibility c_m , psi ⁻¹	10^{-3}
Fracture porosity, ϕ_f	0.45
Fracture permeability, K_f , mD	10^3
Hydraulic fracture compressibility, c_F , psi ⁻¹	10^{-3}
Hydraulic fracture permeability, K_F , mD	10^5
Well length, L_w , ft	1500
Fracture half-length, x_f , ft	400
SRV width, y_1 , ft	250
Fracture height, h_f , ft	0.001
Matrix radius, r_m , ft	5
Initial viscosity, μ_{ini} , cp	0.018
Initial matrix porosity, ϕ_m	0.05
Matrix permeability, K_m , mD	10^{-6}
Fracture compressibility c_f , psi ⁻¹	10^{-3}
Hydraulic fracture porosity, ϕ_F	0.38

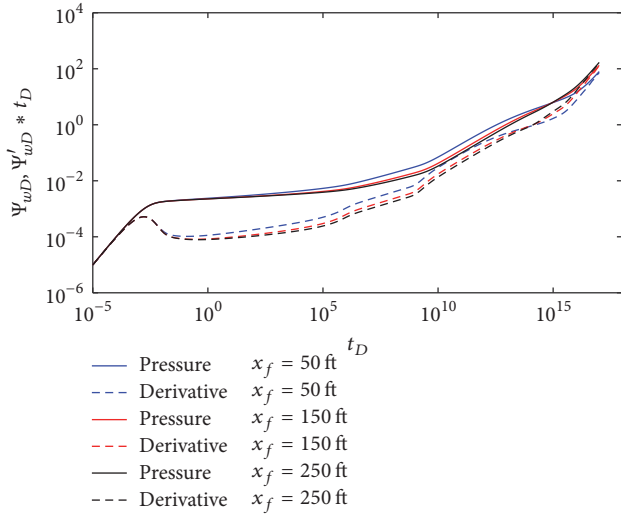


FIGURE 3: Effect of hydraulic fracture half-length on pressure.

Furthermore, pore diameter is bigger and the time of the inflection point for apparent permeability occurring appears later. The apparent permeability decreases faster after the inflection point. The results presented in Figure 2 agree well with those presented by Wu et al. [38].

4.2. Effects of Hydraulic Fracture Half-Length. Figures 3 and 4 show the effect of hydraulic fracture half-length on pseudo-pressure, pseudo-pressure derivative, and dimensionless production. The input parameters are listed in Table 3. According to the results, fracture half-length affects the whole production process. The longer the hydraulic fracture half-length, the more significant the pressure drop and the higher the production rate. The contact area between the hydraulic

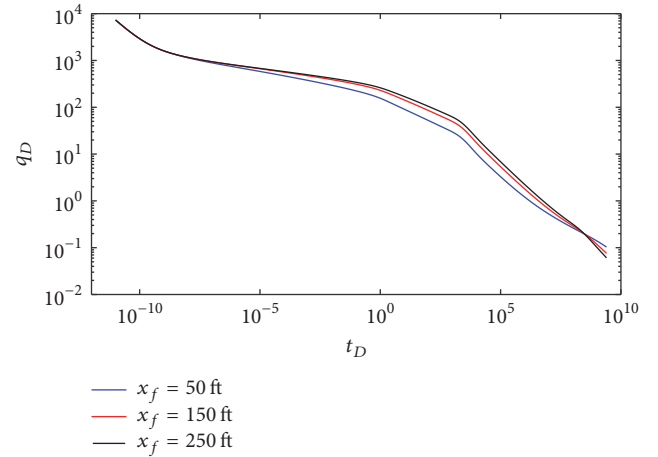


FIGURE 4: Effect of hydraulic fracture half-length on production.

fracture and the shale gas reservoir is larger when the fracture half-length is longer. Therefore, when gas flow resistance is reduced, more shale gas can flow to the fracture. Furthermore, larger flow rate results in significant pressure drop and a larger production.

4.3. Effect of Hydraulic Fracture Permeability. Figures 5 and 6 present the curve of the relationships of dimensionless time and pseudo-pressure and dimensionless production rate under different hydraulic fracture permeability. The figures show that hydraulic fracture permeability dominates all of the production period except for when we have early pure

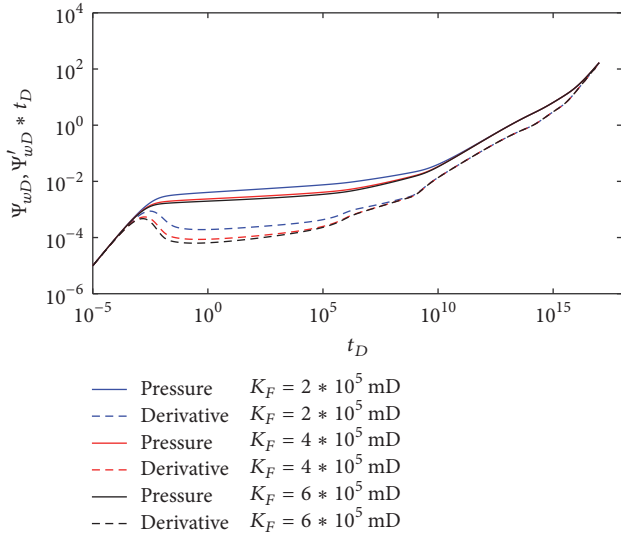


FIGURE 5: Effect of hydraulic fracture permeability on pressure.

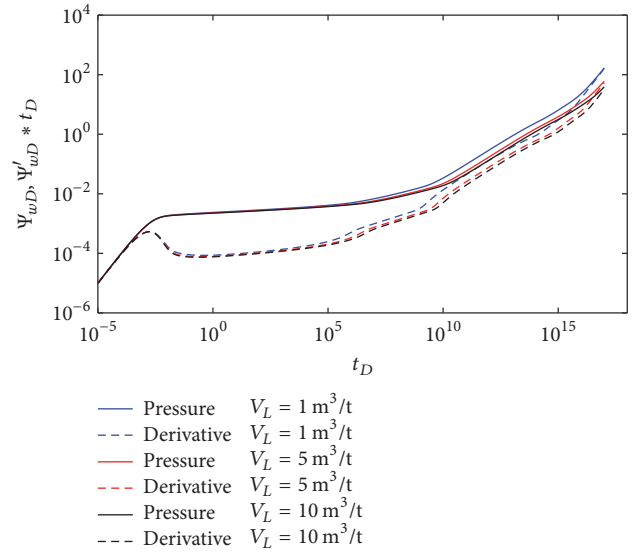


FIGURE 7: Effect of Langmuir volume (V_L) on pressure.

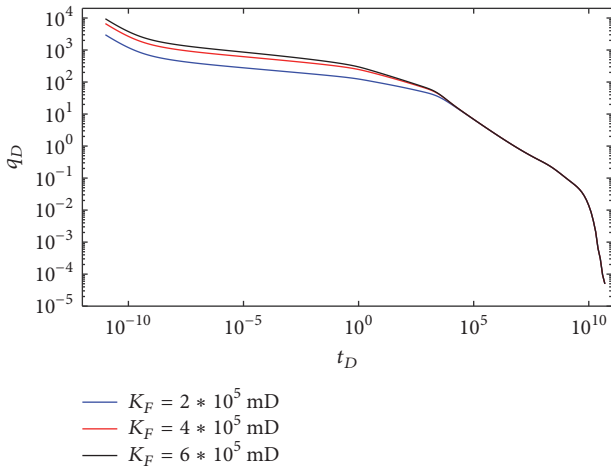


FIGURE 6: Effect of hydraulic fracture permeability on production.

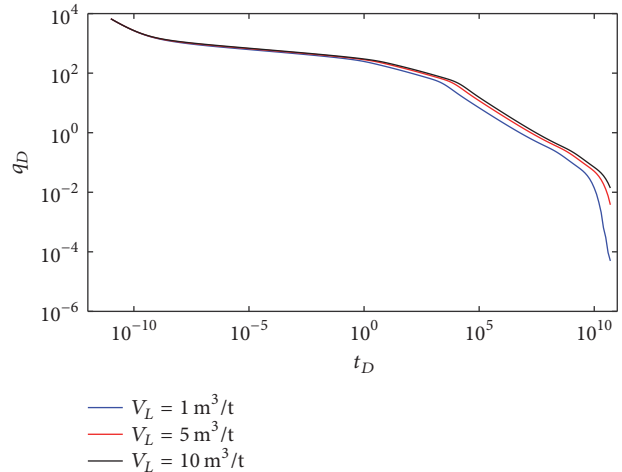


FIGURE 8: Effect of Langmuir volume (V_L) on production.

wellbore storage regime and boundary flow regime. The results are quite different from those observed in a single porosity tight reservoir where hydraulic fracture permeability only exerts an influence on early time pressure behavior [47]. The figures also indicate that, with an increase in fracture permeability, the pseudo-pressure drop and the production rate growth tend to slow down. Therefore, there is an optimal fracture permeability for a certain reservoir.

4.4. Effect of the Langmuir Volume. The effects of the Langmuir volume on pressure and production are plotted in Figures 7 and 8. The Langmuir volume is defined as the maximum volume of shale gas that can be adsorbed to a unit weight organic matrix at infinite pressure. The Langmuir volume is a significant parameter for gas adsorption and desorption. As illustrated in Figures 7 and 8, the larger the Langmuir volume is, the lower the pressure drop and the production will be. This is because a larger Langmuir volume results in a greater amount of adsorbed gas which provides an

extra contribution for well reserves. However, the Langmuir volume does not affect the linear flow stage as only shale gas in hydraulic fractures contributes to production at that period. It can also be seen that, with an increase of the Langmuir volume, the dimensionless rate decreases slowly. This results in longer production time.

4.5. Effect of Matrix Radius. Figures 9 and 10 show the effect of matrix block radius on pseudo-pressure, pseudo-pressure derivative, and dimensionless production rate. The shape and size of the matrix blocks exert a very significant effect on the interporosity flow stage. In this model, the value of the matrix block radius determines the magnitudes of the interporosity flow coefficient and the storativity ratio. According to the results, the matrix block radius mainly affects the transitional stage and the stage of bilinear flow. That is to say, the larger the matrix block radius, the more significant the pressure drop of the transitional stage. Consequently, the stage of bilinear flow

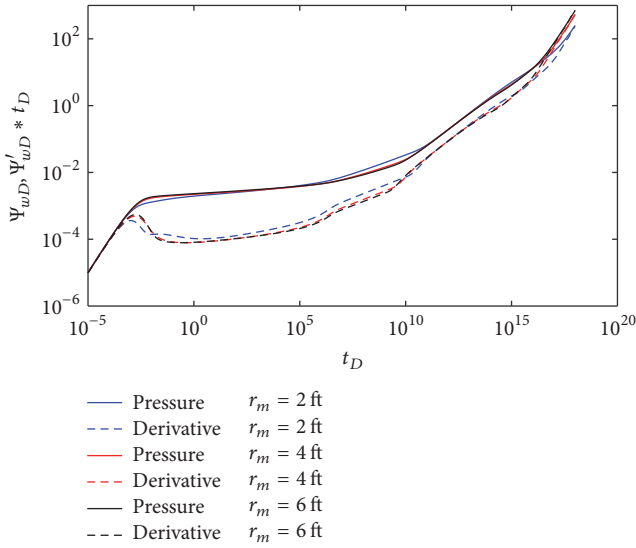


FIGURE 9: Effect of matrix radius on pressure.

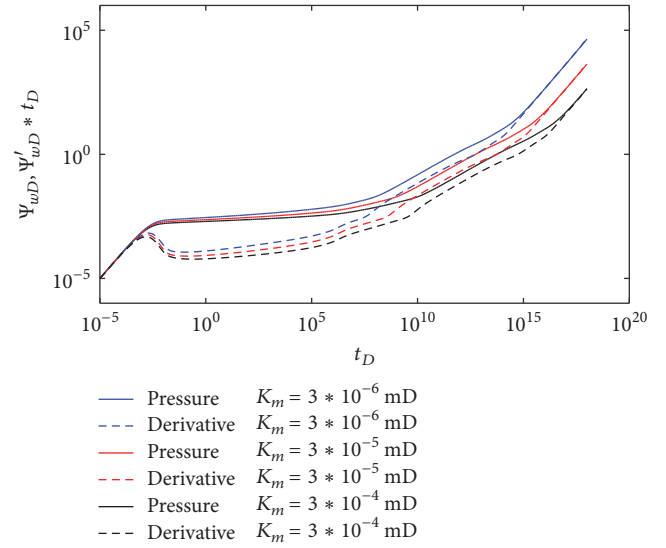


FIGURE 11: Effect of matrix permeability on pressure.

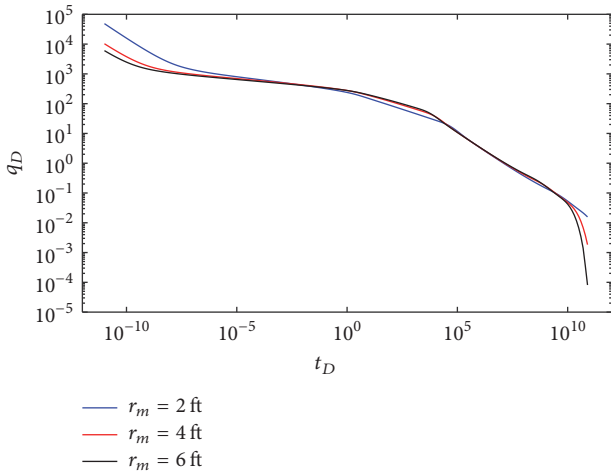


FIGURE 10: Effect of matrix radius on production.

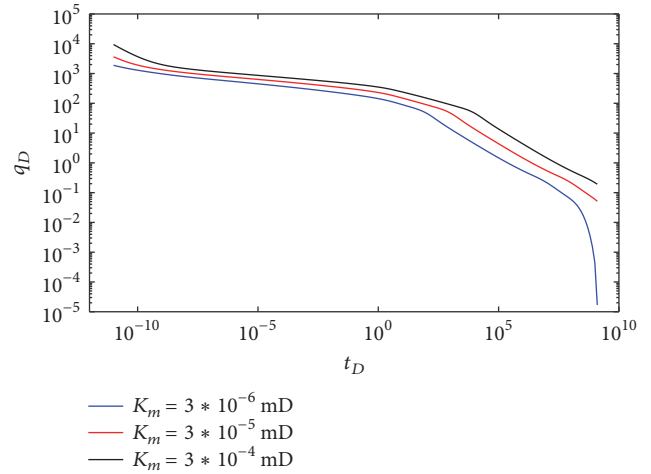


FIGURE 12: Effect of matrix permeability on production.

occurs later. When the matrix block radius is large enough, bilinear flow disappears. Meanwhile, the magnitude of the matrix block radius also affects the production in the early and middle stages. With an increasing matrix block radius, the production rate gradually decreases, and the production decline rate decreases as well. In the late stage of production, the production rates under different matrix block radii are approximately the same [30].

4.6. Effect of Matrix Permeability. Figures 11 and 12 demonstrate how matrix permeability affects pseudo-pressure and dimensionless production rate. As can be seen in these two figures, as the matrix permeability decreases, pressure drop in the transient period becomes more significant and the fracture linear flow period becomes longer. Dimensionless production rate increases slowly with an increase of matrix permeability. The results indicate that the rock has more capacity to transfer gas molecules from the matrix to the

fracture system. Under ultra-low matrix permeability conditions, the pressure variation is more sensitive.

4.7. Effect of Induced Fracture Permeability. Figures 13 and 14 represent the effect of induced fracture permeability on pressure and production. The induced fracture permeability of shale reservoirs is an extremely important reservoir parameter, as shale gas transport to hydraulic fracture should take place through induced fracture systems. Therefore, the induced fracture permeability determines the scale of gas well productivity. The results show that the higher the induced fracture permeability, the more significant the pressure drop during the transitional period. With a continuous increase in induced fracture permeability, the duration of the stage of bilinear flow becomes shorter and shorter until it completely disappears. Figure 13 indicates that the induced fracture permeability has a more significant influence on pressure than matrix radius and matrix permeability. Meanwhile,

TABLE 4: Parameters of the typical well.

Porosity	Viscosity	Compressibility	Temperature
0.032	$1.47 * 10^{-2}$ cp	$4.8 * 10^{-2}$ MPa ⁻¹	96.8°C
Wellhead pressure	Depth	Pressure coefficient	Horizontal length
39 MPa	2900 m	1.96	1438 m
Ψ_{ini}	Ψ_{wD}	Fracturing segments	Thickness
$1.62 * 10^5$ MPa ² /cp	$1.62 * 10^5$ MPa ⁴ /cp	15	35 m

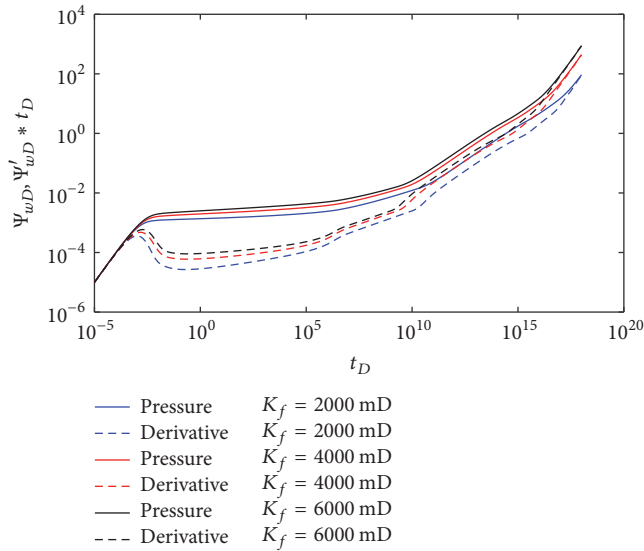


FIGURE 13: Effect of induced fracture permeability on pressure.

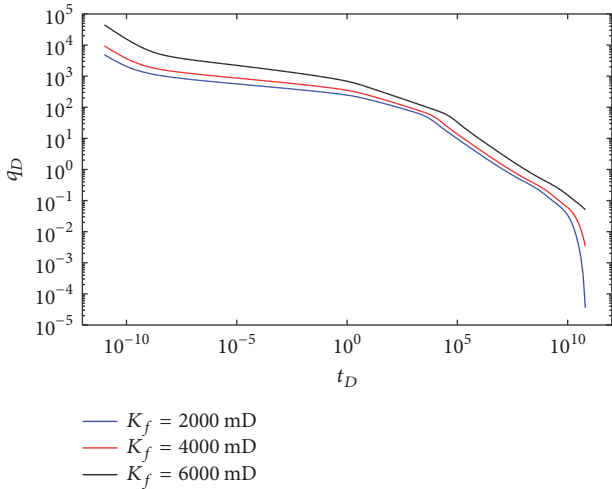


FIGURE 14: Effect of induced fracture permeability on production.

the induced fracture permeability also affects the scale of production rate; that is, the higher the permeability, the larger the scale. However, as far as production rate is concerned, the secondary fracture permeability only affects its scale, but not its decline rate.

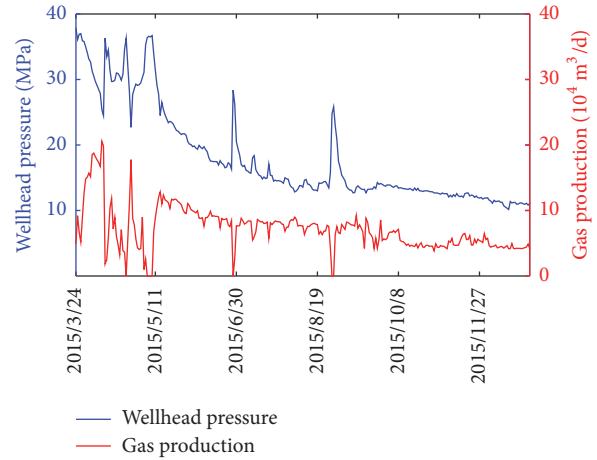


FIGURE 15: Production history.

5. Case Study

The MFHW is located in the transitional zone between the Sichuan Basin and the Yunnan-Guizhou Plateau (400–1,200 m in altitude) and mainly developed a marine and continental sedimentary facies. The specific stratum parameters are listed in Table 4.

As seen in Figure 15, the production data show that there is a relatively high degree of correlation between pressure and production; the production data present an obvious response to the pressure fluctuations caused by the test carried out in the early stage; therefore, the data have a certain degree of reliability. As shown by a comparative analysis on the actual production data and production curve, the measured data are deviated from the typical curve by a relatively significant extent. This is mainly because of the skin effect and wellbore storage effect on the early stage seepage. The fitting curve shows that the data points are concentrated in the stage of linear flow of matrix (see Figure 16), mainly because the extremely low permeability of matrix-fractures has extended the duration of the stage of nonsteady state linear flow.

6. Conclusion

In this study, an analytical model was presented to simulate shale gas flow through MFHW in a shale reservoir. Based on microscale percolation mechanisms in nanopores, a seven-linear-flow model for dual-porosity formations was established. This model takes viscous flow, the Knudsen diffusion, the sorption-induced swelling response, the

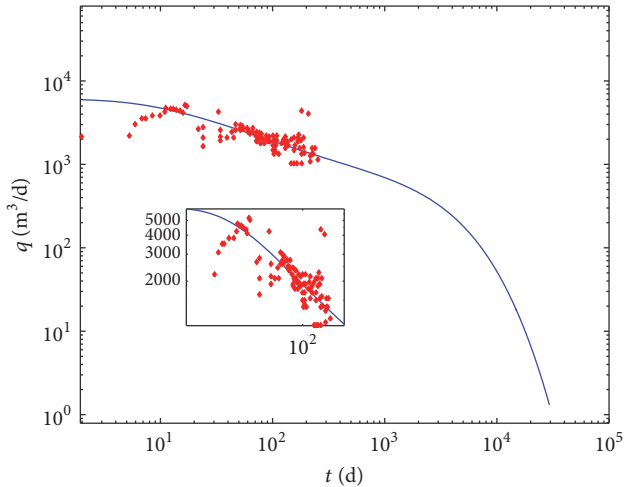


FIGURE 16: History matching of typical well.

adsorption/desorption, the matrix shrinkage and the stress sensitivity effect into consideration. The pressure transient analysis was carried out under conditions of constant rate. The following conclusions were deduced:

(1) The shale gas transport mechanism in nanopores mainly includes bulk gas transport and gas adsorption/desorption. Bulk gas apparent permeability is a weighted summation of viscous flow permeability and the Knudsen diffusion permeability. Gas desorption can increase the total apparent permeability.

(2) A semianalytical model was established for the pressure behavior of MFHWs in shale gas reservoirs. Based on the proposed model, flow regimes were identified into two top reservoir regions, two inner-reservoir regions, two outer-reservoir regions, and one artificial fracture region.

(3) Larger fracture half-length results in a more significant pressure drop and a higher production rate. Fracture permeability dominates throughout the production period except during the early pure wellbore storage stage and the boundary flow stage. The effect of desorption cannot be neglected when simulating, as the Langmuir volume has a significant influence on the production rate. Compared with the matrix radius and matrix permeability, pressure and production are more sensitive to induced fracture permeability.

(4) The semianalytical model fits relatively well with the actual production data, has a reliable theoretical foundation, and can preferably describe the dynamic changes of pressure in the exploration process of shale gas wells.

Nomenclature

T : Temperature, K
 τ : Shale tortuosity
 M : Gas molar mass, kg/mol
 R : Universal gas constant, J/(mol*K)
 k_B : Boltzmann constant, J/K
 ρ_s : Shale density, t/m³
 ρ_g : Gas density, t/m³

c_p : Shale compressibility, MPa⁻¹
 c_g : Gas compressibility, MPa⁻¹
 V_{std} : Mole volume of gas at standard constant, m³/mol
 V_L : Langmuir volume, m³/t
 P_L : Langmuir pressure, MPa
 E : Shale matrix Young modulus, MPa
 α : Rarefaction coefficient
 ψ : Pseudo-pressure, psi²/cp
 q : Production rate, Mscf/D
 s : Laplace transform parameter
 t : Time, hours
 γ : Permeability modulus, psi⁻¹
 x : x -Coordinate, ft
 y : y -Coordinate, ft
 z : z -Coordinate, ft
 w_F : Hydraulic fracture width, ft
 x_f : Hydraulic fracture half-length, ft
 x_e : Reservoir size in x -direction, ft
 y_1 : SRV width, ft
 y_2 : Half-width between two fractures, ft
 z_1 : Half- fracture height, ft
 z_2 : Half reservoir thickness, ft
 r : Radius, ft
 μ : Shale viscosity, cp
 ϕ : Porosity
 σ : Shape factor
 η : Diffusivity, ft/hour
 λ : Flow capacity ratio
 a_{ave} : Desorption coefficient at average pressure
 ω : Storativity ratio
 S : Skin factor
 C_D : Dimensionless wellbore storage coefficient.

Subscript

D : Dimensionless
 f : Natural fracture system
 F : Hydraulic fracture
 i : The i -th region ($i = 2, 3, 4, 5, 6, 7$)
 m : Matrix system
 sc : Standard condition
 wD : Dimensionless wellbore
 eD : Dimensionless length of external boundary.

Conflicts of Interest

The authors declare that they have no conflicts of interest.

Acknowledgments

The authors would like to acknowledge the support from MOE Key Laboratory of Petroleum Engineering in China University of Petroleum (Beijing). The authors would also like to acknowledge the financial support from the National Nature Science Foundation of China (no. 51504265) and Science Foundation of China University of Petroleum, Beijing (no. 2462015YQ0223).

References

- [1] R. Heller, J. Vermylen, and M. Zoback, "Experimental investigation of matrix permeability of gas shales," *AAPG Bulletin*, vol. 98, no. 5, pp. 975–995, 2014.
- [2] J. B. Curtis, "Fractured shale-gas systems," *AAPG Bulletin*, vol. 86, no. 11, pp. 1921–1938, 2002.
- [3] F. Javadpour, "Nanopores and apparent permeability of gas flow in mudrocks (shales and siltstone)," *Journal of Canadian Petroleum Technology*, vol. 48, no. 8, pp. 16–21, 2009.
- [4] F. Yang, Z. Ning, Q. Wang, R. Zhang, and B. M. Krooss, "Pore structure characteristics of lower Silurian shales in the southern Sichuan Basin, China: Insights to pore development and gas storage mechanism," *International Journal of Coal Geology*, vol. 156, pp. 12–24, 2016.
- [5] F. Civan, D. Devegowda, and R. F. Sigal, "Critical evaluation and improvement of methods for determination of matrix permeability of shale," in *Proceedings of the SPE Annual Technical Conference and Exhibition*, pp. 4620–4629, Society of Petroleum Engineers, October 2013.
- [6] W. N. Yuan, Z. J. Pan, X. Li et al., "Experimental study and modelling of methane adsorption and diffusion in shale," *Fuel*, vol. 117, pp. 509–519, 2014.
- [7] R. Aguilera, "Flow units: from conventional to tight gas to shale gas reservoirs," in *Proceedings of the Trinidad and Tobago Energy Resources Conference*, pp. 572–587, Society of Petroleum Engineers, June 2010.
- [8] M. R. Rahmaman, R. Aguilera, and A. Kantzas, "A new unified diffusion-viscous-flow model based on pore-level studies of tight gas formations," *SPE Journal*, vol. 18, no. 1, pp. 38–49, 2012.
- [9] M. Wang and Z. Li, "Nonideal gas flow and heat transfer in micro- and nanochannels using the direct simulation Monte Carlo method," *Physical Review E: Statistical, Nonlinear, and Soft Matter Physics*, vol. 68, no. 4, Article ID 046704, 2003.
- [10] H. Darabi, A. Ettehad, F. Javadpour, and K. Sepehrnoori, "Gas flow in ultra-tight shale strata," *Journal of Fluid Mechanics*, vol. 710, pp. 641–658, 2012.
- [11] F. Javadpour, D. Fisher, and M. Unsworth, "Nanoscale gas flow in shale gas sediments," *Journal of Canadian Petroleum Technology*, vol. 46, no. 10, pp. 55–61, 2007.
- [12] X. Cui, A. M. M. Bustin, and R. M. Bustin, "Measurements of gas permeability and diffusivity of tight reservoir rocks: Different approaches and their applications," *Geofluids*, vol. 9, no. 3, pp. 208–223, 2009.
- [13] V. Swami, A. T. Settari, and F. Javadpour, "A numerical model for multi-mechanism flow in shale gas reservoirs with application to laboratory scale testing," in *Proceedings of the SPE EAGE Annual Conference & Exhibition incorporating (EUROPEC '13)*, pp. 1274–1293, Society of Petroleum Engineers, June 2013.
- [14] W. Yu and K. Sepehrnoori, "Simulation of gas desorption and geomechanics effects for unconventional gas reservoirs," *Fuel*, vol. 116, pp. 455–464, 2014.
- [15] M. J. Mayerhofer, E. P. Lolon, J. E. Youngblood, and J. R. Heinze, "Integration of microseismic fracture mapping results with numerical fracture network production modeling in the Barnett shale," in *Proceedings of the SPE Annual Technical Conference and Exhibition (ATCE '06)*, pp. 976–983, Society of Petroleum Engineers, San Antonio, Tex, USA, September 2006.
- [16] C. R. Clarkson, "Production data analysis of unconventional gas wells: review of theory and best practices," *International Journal of Coal Geology*, vol. 109, pp. 101–146, 2013.
- [17] F. Kucuk and W. K. Sawyer, "Transient flow in naturally fractured reservoirs and its application to devonian gas shales," in *Proceedings of the SPE Annual Technical Conference and Exhibition*, Society of Petroleum Engineers, 1980.
- [18] S.-T. Lee and J. R. Brockenbrough, "A new approximate analytic solution for finite-conductivity vertical fractures," *SPE Formation Evaluation*, vol. 1, no. 1, pp. 75–88, 1986.
- [19] E. Ozkan, R. S. Raghavan, and O. G. Apaydin, "Modeling of fluid transfer from shale matrix to fracture network," in *Proceedings of the SPE Annual Technical Conference and Exhibition*, pp. 3314–3331, Society of Petroleum Engineers, September 2010.
- [20] E. Stalgorova and L. Mattar, "Analytical model for unconventional multifractured composite systems," *SPE Reservoir Evaluation & Engineering*, vol. 16, no. 3, pp. 246–256, 2013.
- [21] E. Stalgorova and L. Mattar, "Analytical model for history matching and forecasting production in multifrac composite systems," in *Proceedings of the SPE Canadian Tight Resources Conference*, pp. 450–466, Society of Petroleum Engineers, November 2012.
- [22] E. Stalgorova and L. Mattar, "Practical analytical model to simulate production of horizontal wells with branch fractures," in *Proceedings of the SPE Canadian Tight Resources Conference*, pp. 433–449, Society of Petroleum Engineers, November 2012.
- [23] O. G. Apaydin, E. Ozkan, and R. Raghavan, "Effect of discontinuous microfractures on ultratight matrix permeability of a dual-porosity medium," *SPE Reservoir Evaluation & Engineering*, vol. 15, no. 4, pp. 473–485, 2012.
- [24] Y.-L. Zhao, L.-H. Zhang, J.-Z. Zhao, J.-X. Luo, and B.-N. Zhang, "'Triple porosity' modeling of transient well test and rate decline analysis for multi-fractured horizontal well in shale gas reservoirs," *Journal of Petroleum Science and Engineering*, vol. 110, pp. 253–262, 2013.
- [25] Y.-L. Zhao, L.-H. Zhang, J.-X. Luo, and B.-N. Zhang, "Performance of fractured horizontal well with stimulated reservoir volume in unconventional gas reservoir," *Journal of Hydrology*, vol. 512, pp. 447–456, 2014.
- [26] Q. Liu, K. Li, W. Wang, X. Hu, and H. Liu, "Production behavior of fractured horizontal well in closed rectangular shale gas reservoirs," *Mathematical Problems in Engineering*, vol. 2016, Article ID 4260148, 9 pages, 2016.
- [27] H.-T. Wang, "Performance of multiple fractured horizontal wells in shale gas reservoirs with consideration of multiple mechanisms," *Journal of Hydrology*, vol. 510, pp. 299–312, 2014.
- [28] R.-H. Zhang, L.-H. Zhang, R.-H. Wang, Y.-L. Zhao, and D.-L. Zhang, "Research on transient flow theory of a multiple fractured horizontal well in a composite shale gas reservoir based on the finite-element method," *Journal of Natural Gas Science and Engineering*, vol. 33, Article ID 66e80, pp. 587–598, 2016.
- [29] R. H. Zhang, L. H. Zhang, R. H. Wang et al., "Simulation of a multistage fractured horizontal well with finite conductivity in composite shale gas reservoir through finite-element method," *Energy & Fuels*, vol. 30, no. 11, pp. 9036–9049, 2016.
- [30] Y. Zeng, Z. Ning, Y. Lei, L. Huang, C. Lv, and Y. Hou, "Analytical model for shale gas transportation from matrix to fracture network," in *Proceedings of the SPE Europec featured at 79th EAGE Conference and Exhibition*, Society of Petroleum Engineers, Paris, France, 2017.
- [31] J. Wang, L. Chen, Q. Kang, and S. S. Rahman, "Apparent permeability prediction of organic shale with generalized lattice Boltzmann model considering surface diffusion effect," *Fuel*, vol. 181, pp. 478–490, 2016.

- [32] A. Tinni, E. Fathi, R. Agarwal, C. Sondergeld, Y. Akkutlu, and C. Rai, "Shale permeability measurements on plugs and crushed samples," in *Proceedings of the SPE Canadian Unconventional Resources Conference*, pp. 342–355, Society of Petroleum Engineers, November 2012.
- [33] S. Wang, D. Elsworth, and J. Liu, "A mechanistic model for permeability evolution in fractured sorbing media," *Journal of Geophysical Research: Solid Earth*, vol. 117, no. 6, 2012.
- [34] J.-G. Choi, D. D. Do, and H. D. Do, "Surface diffusion of adsorbed molecules in porous media: Monolayer, multilayer, and capillary condensation regimes," *Industrial & Engineering Chemistry Research*, vol. 40, no. 19, pp. 4005–4031, 2001.
- [35] G. Karniadakis, A. Beskok, and N. Aluru, *Simple Fluids in Nanochannels*, Springer, New York, NY, USA, 2005.
- [36] S. Yuhong and W. K. Chan, "Analytical modeling of rarefied Poiseuille flow in microchannels," *Journal of Vacuum Science & Technology A: Vacuum, Surfaces, and Films*, vol. 22, no. 2, pp. 383–394, 2004.
- [37] F. Reif, *Fundamentals of Statistical and Thermal Physics*, Wiley-Interscience, New York, 2009.
- [38] K. Wu, X. Li, C. Wang et al., "Apparent permeability for gas flow in shale reservoirs coupling effects of gas diffusion and desorption," in *Proceedings of the Unconventional Resources Technology Conference (URTEC '14)*, August 2014.
- [39] K. R. Alnoaimi and A. R. Kovscek, "Experimental and numerical analysis of gas transport in shale including the role of sorption," in *Proceedings of the SPE Annual Technical Conference and Exhibition*, pp. 3527–3542, Society of Petroleum Engineers, October 2013.
- [40] A. D. Bangham, "Membrane models with phospholipids," *Progress in Biophysics and Molecular Biology*, vol. 18, pp. 29–95, 1968.
- [41] I. Langmuir and V. J. Schaefer, "The effect of dissolved salts on insoluble monolayers," *Journal of the American Chemical Society*, vol. 59, no. 11, pp. 2400–2414, 1937.
- [42] J. P. Seidle and L. G. Huitt, "Experimental measurement of coal matrix shrinkage due to gas desorption and implications for cleat permeability increases," in *Proceedings of the International Meeting on Petroleum Engineering*, pp. 575–582, November 1995.
- [43] O. A. Pedrosa, "Pressure transient response in stress-sensitive formations," in *Proceedings of the SPE California Regional Meeting*, Society of Petroleum Engineers, 1986.
- [44] Q. Deng, R.-S. Nie, Y.-L. Jia, X.-Y. Huang, J.-M. Li, and H.-K. Li, "A new analytical model for non-uniformly distributed multi-fractured system in shale gas reservoirs," *Journal of Natural Gas Science and Engineering*, vol. 27, pp. 719–737, 2015.
- [45] H. Mukherjee and M. J. Economides, "Parametric comparison of horizontal and vertical well performance," *SPE Formation Evaluation*, vol. 6, no. 2, pp. 209–216, 1991.
- [46] A. F. Van Everdingen and W. Hurst, "The application of the Laplace transformation to flow problems in reservoirs," *Journal of Petroleum Technology*, vol. 1, no. 12, pp. 305–324, 1949.
- [47] S. Yao, F. Zeng, H. Liu, and G. Zhao, "A semi-analytical model for multi-stage fractured horizontal wells," *Journal of Hydrology*, vol. 507, pp. 201–212, 2013.

Research Article

Theoretical Modeling of Dielectric Properties of Artificial Shales

Tongcheng Han ^{1,2}, **Roman Beloborodov** ³, **Marina Pervukhina**,⁴
Matthew Josh,⁴ **Yanlin Cui**,⁵ and **Pengyao Zhi**⁶

¹*School of Geosciences, China University of Petroleum (East China), Qingdao 266580, China*

²*Laboratory for Marine Mineral Resources, Qingdao National Laboratory for Marine Science and Technology, Qingdao 266071, China*

³*Department of Exploration Geophysics, Curtin University, Perth, WA 6151, Australia*

⁴*CSIRO Energy, Perth, WA 6151, Australia*

⁵*Library, China University of Petroleum (East China), Qingdao 266580, China*

⁶*College of Earth Science and Engineering, Shandong University of Science of Technology, Qingdao 266590, China*

Correspondence should be addressed to Tongcheng Han; hantc@upc.edu.cn

Received 27 July 2017; Revised 18 October 2017; Accepted 9 November 2017; Published 11 January 2018

Academic Editor: Xiaohu Dong

Copyright © 2018 Tongcheng Han et al. This is an open access article distributed under the Creative Commons Attribution License, which permits unrestricted use, distribution, and reproduction in any medium, provided the original work is properly cited.

Accurately modeling the anisotropic dielectric properties of shales is important for the interpretation of dielectric data acquired from shales as source rocks and unconventional reservoirs. We have developed a multiphase incremental model for the frequency dependent anisotropic dielectric properties of sedimentary rocks and presented an approach based on the developed model to simulate the measured anisotropic dielectric behaviors of artificial shales. The new model was built based on the theoretical basis of differential effective medium models for any number of mineral grain components aligned in any direction and was shown to be independent of the mixing order. The model incorporates the measured orientation distribution function of the clay particles to determine the shale dielectric anisotropy, and the frequency dependent dielectric behaviors of the wet clay minerals are obtained by inverting the dielectric properties of the artificial sample composed of clay and the same brine as in other artificial shales. The modeling technique combined important polarization mechanisms in the intermediate frequency range and was shown to give satisfactory fit to the measured frequency dependent anisotropic relative permittivity and conductivity of the artificial shales with varying silt contents by using a reasonable aspect ratio and constant dielectric parameters for the silt grains.

1. Introduction

Shales are the most abundant sedimentary rocks and are of increasing interest in hydrocarbon exploration worldwide as source rocks and unconventional reservoirs. Among the physical and petrophysical parameters employed for shale characterizations, the electrical and more specifically dielectric properties are one of the most direct and effective ways for the discrimination of geofluid types and concentrations as well as for the inference of their transport properties. However, for improved inversion and interpretation of the acquired shale dielectric data, a robust rock physics model that links the bulk dielectric properties of shales to those of the complex rock-forming components is essential. Such models must also be able to account for the shale anisotropy caused by the preferential orientation of mineral foliations.

In recent decades, shale dielectric modeling was mainly focused on the effects of the electrical double layer associated with clay minerals (e.g., [1–7]). Effort has been made to develop models that can explain the dependence of complex electrical conductivity on cation exchange capacity (CEC) and specific surface area (SSA), salinity and pH of the pore water, sorption of cations and organic molecules, influence of grain size, and the relationship between surface conductivity and quadrature conductivity, temperature, and water saturation. While the model is designed for isotropic shaly materials, Revil et al. [8] generalize the versatile model to the case of anisotropic shales by introducing tensorial versions of formation factor and tortuosity with the intention of quantifying the role played by kerogen on surface conductivity and quadrature conductivity. However, the model accounts only for the Stern layer (the inner portion of the electrical double

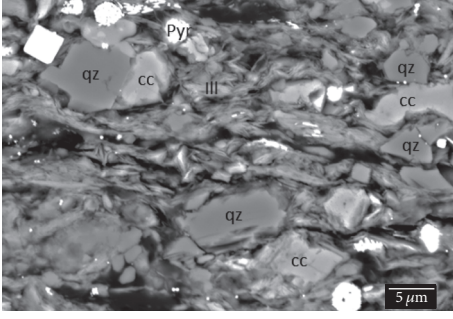


FIGURE 1: A scanning electron microscopy (SEM) image showing the mineral composition and microstructure of a typical shale sample (courtesy of C. Delle Piane). In this sample, the quartz (qz), calcite (cc), and pyrite (Pyr) grains are randomly distributed while the illite (Ill) shows some local disorder or misalignment, with respect to the vertical symmetry axis.

layer coating the surface of mineral grains) polarization [9] and neglects an important polarization mechanism in the intermediate frequency range (0.1 MHz–100 MHz), often referred to as Maxwell–Wagner polarization or interfacial polarization, due to the build-up of charge on the interfaces of the heterogeneous systems (e.g., [10]).

To describe the dielectric behaviors of a heterogeneous system caused by the Maxwell–Wagner polarization, various models have been developed (e.g., [11–20]) and a comprehensive review of the models can be found in Cai et al. [19]. Among these models, the differential effective medium (DEM) models are the kind of models that have had the most success in simulating the dielectric behavior of clay-free sedimentary rocks [21] and in modeling the high-frequency dielectric properties of both clay-free soils and clay soils [22]. The Hanai-Bruggeman (HB) equation [23–26] is one of such DEM models that predicts the bulk rock dielectric properties through the dielectric properties of the components, their volume fractions, and the geometric details of how the phases are arranged relative to each other described by the cementation factor (m). However, the HB model is designed for the isotropic medium only and could not be applied to modeling the anisotropic dielectric properties of shales. On the other hand, the Asami [27] model, as another kind of the DEM model, is capable of modeling the dielectric properties of a medium at any given direction relative to the applied electric field. The Asami model is a 2-phase (i.e., solid minerals and fluid) model that assumes that all the solid particles are uniformly shaped and aligned, which, however, is not the case for real shales that usually contain multiple mineral phases and the orientations of each of the minerals and the alignments of the different proportion of the same minerals are varying as shown in Figure 1. This requires the development of a multiphase anisotropic dielectric model where the complex mineral composition and the orientation distribution of the clay minerals can be accounted for; the model should also take into account the Stern layer polarization associated with clay minerals.

This work aims to present such a model. We first extend Asami’s 2-phase anisotropic dielectric model to more phases

based on an incremental algorithm [21, 28, 29] so that the multiminerale nature of shales can be modeled. In the new model, the clay minerals with different orientations are grouped through the measured clay orientation distribution function, and the frequency dependent dielectric properties of the wet clay minerals that contain the information of the Stern layer polarization are determined by inverting the measured dielectric responses of an artificial sample composed of pure clay and pore water identical to that used in the shale under investigation with the silt component. The approach is then applied to modeling the laboratory measurements of the qualified samples in the frequency range 0.1 MHz–100 MHz presented in the companion paper.

2. Anisotropic Dielectric Model

2.1. Two-Phase Anisotropic Dielectric Model. Based on Maxwell–Wagner theory [30, 31], Asami [27] derived an equation for the complex relative permittivity (ϵ^*) of a 2-phase mixture where the ellipsoidal inclusions (with complex permittivity of ϵ_g^*) are oriented in the background medium (with complex permittivity of ϵ_a^*) with the angle φ_k between the k -axis and the electric field, as follows:

$$\epsilon^* = \epsilon_a^* \left[1 + \Phi \sum_{k=x,y,z} \frac{\epsilon_g^* - \epsilon_a^*}{\epsilon_a^* + (\epsilon_g^* - \epsilon_a^*) L_k} \cos^2 \varphi_k \right], \quad (1)$$

where Φ is the volume fraction of the solid inclusions; the complex relative permittivity ϵ^* is defined as

$$\epsilon^* = \epsilon' - j\epsilon'' = \epsilon + \frac{\kappa}{j\epsilon_0\omega}, \quad (2)$$

where $j = \sqrt{-1}$, ϵ' and ϵ'' are the real and imaginary parts of ϵ^* , respectively, ϵ is the relative permittivity, κ is the effective conductivity, $\epsilon_0 = 8.8542 \times 10^{-12}$ F/m is the absolute permittivity of vacuum, and $\omega = 2\pi f$ (where f is the frequency) is the angular frequency of the applied electric field. L_k is the k -axis depolarization factor of the oblate spheroidal inclusions ($R_x = R_y > R_z$, where R_k is the semiaxis of the ellipsoid along the k -axis) with aspect ratio $\alpha < 1$ ($\alpha = R_z/R_x$), given by [27]

$$L_z = \frac{1}{1 - \alpha^2} - \frac{\alpha}{(1 - \alpha^2)^{3/2}} \cos^{-1} \alpha, \quad (3)$$

$$L_x = L_y = \frac{(1 - L_z)}{2}.$$

2.2. Multiphase Anisotropic Dielectric Model. Berg [21] presented an incremental algorithm to extend the 2-phase HB equation to more phases without ordering effect. Han et al. [28] adapted the algorithm to the isotropic dielectric model of Asami [27]. In this work, we apply the incremental concept to the 2-phase anisotropic dielectric model (see (1)) to enable more mineral components to be modeled.

In the new multiphase (M -phase) anisotropic dielectric model, the second phase with a volume fraction of C_2/n

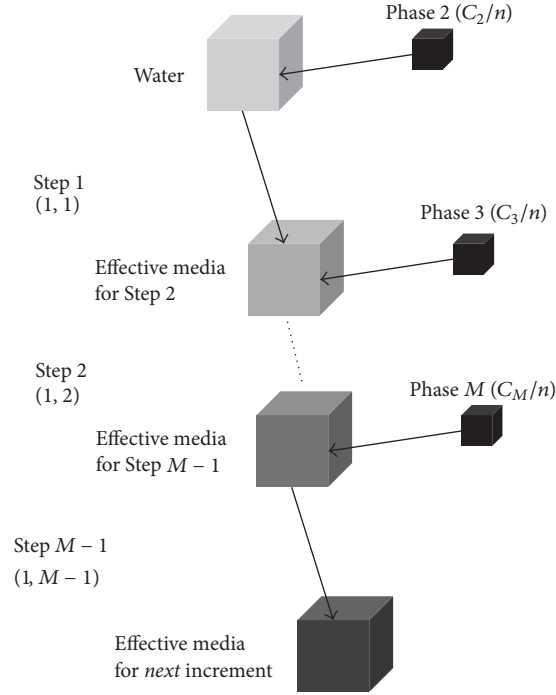


FIGURE 2: Schematic diagram showing the steps used in the first increment in the multiphase anisotropic dielectric model, in which water is the starting medium. The effective media formed in the last step of each increment become the starting background for the next increment, after Han et al. [28, 29].

(where C_2 is the initial concentration of phase 2 and n is the incremental number) is first added to the water (the first phase) background, forming an effective medium for the next step (step 2 as shown in Figure 2) in which phase 3 with a volume fraction of C_3/n is then included to form an effective background for step 3. This procedure continues until the M th phase with volume fraction of C_M/n is finally added. The effective media formed when the $M - 1$ phases included in each increment become a background for the next increment until the incremental number of n is reached. The effective media formed in each step are assumed to be an effective single phase, and the 2-phase anisotropic equation (see (1)) is used to calculate the effective dielectric properties in the directions parallel and perpendicular to the applied electric field, respectively.

In the incremental algorithm, the inclusion is added to the effective background to displace the same amount of medium; the volume fractions of the various phases in each step are therefore functions of their volume fractions in the previous step. Following Han et al. [28, 29], it is convenient to derive the volume fractions of the inclusions ($V_i, i = 1 : M$) based on their initial concentrations C and the incremental number n .

In the first increment (indicated by the column number), the volume fraction of each component after phase 2 is included (step 1, denoted by the row number):

$$V_1(1, 1) = 1 - \frac{C_2}{n},$$

$$V_2(1, 1) = \frac{C_2}{n},$$

$$V_3(1, 1) = 0,$$

$$\vdots$$

$$V_M(1, 1) = 0; \tag{4}$$

the volume fractions of the constituents when phase 3 is added (step 2) are calculated as

$$V_1(1, 2) = V_1(1, 1) \cdot \left(1 - \frac{C_3}{n}\right),$$

$$V_2(1, 2) = V_2(1, 1) \cdot \left(1 - \frac{C_3}{n}\right),$$

$$V_3(1, 2) = \frac{C_3}{n}, \tag{5}$$

$$V_4(1, 2) = 0,$$

$$\vdots$$

$$V_M(1, 2) = 0;$$

the volume fractions of the components when phase 4 is added (step 3) are

$$V_1(1, 3) = V_1(1, 2) \cdot \left(1 - \frac{C_4}{n}\right),$$

$$V_2(1, 3) = V_2(1, 2) \cdot \left(1 - \frac{C_4}{n}\right),$$

$$\begin{aligned}
V_3(1,3) &= V_3(1,2) \cdot \left(1 - \frac{C_4}{n}\right), & V_1(i,3) &= V_1(i,2) \cdot \left(1 - \frac{C_4}{n}\right), \\
V_4(1,3) &= \frac{C_4}{n}, & V_2(i,3) &= V_2(i,2) \cdot \left(1 - \frac{C_4}{n}\right), \\
V_5(1,3) &= 0, & V_3(i,3) &= V_3(i,2) \cdot \left(1 - \frac{C_4}{n}\right), \\
&\vdots & V_4(i,3) &= V_4(i,2) \cdot \left(1 - \frac{C_4}{n}\right) + \frac{C_4}{n}, \\
V_M(1,3) &= 0, & V_5(i,3) &= V_5(i,2) \cdot \left(1 - \frac{C_4}{n}\right), \\
&& &\vdots \\
&& & V_M(i,3) = V_M(i,2) \cdot \left(1 - \frac{C_4}{n}\right), \\
&& & V_1(i, M-1) = V_1(i, M-2) \cdot \left(1 - \frac{C_M}{n}\right), \\
&& &\vdots \\
&& & V_{M-1}(i, M-1) = V_{M-1}(i, M-2) \cdot \left(1 - \frac{C_M}{n}\right), \\
&& & V_M(i, M-1) = V_M(i, M-2) \cdot \left(1 - \frac{C_M}{n}\right) + \frac{C_M}{n}.
\end{aligned} \tag{6}$$

and after the final step (step $M - 1$) when phase M is finally included in the first iteration, the volume fraction of each element can be found by

$$\begin{aligned}
V_1(1, M-1) &= V_1(1, M-2) \cdot \left(1 - \frac{C_M}{n}\right), \\
&\vdots \\
V_{M-1}(1, M-1) &= V_{M-1}(1, M-2) \cdot \left(1 - \frac{C_M}{n}\right), \\
V_M(1, M-1) &= \frac{C_M}{n}.
\end{aligned} \tag{7}$$

The effective medium in the last step in each increment forms the starting background for the next increment; the volume fraction of each component in the i th increment ($2 \leq i \leq n$), after phases 2, 3, 4, and $M - 1$ are added, is therefore given, respectively, by

$$\begin{aligned}
V_1(i,1) &= V_1(i-1, M-1) \cdot \left(1 - \frac{C_2}{n}\right), \\
V_2(i,1) &= V_2(i-1, M-1) \cdot \left(1 - \frac{C_2}{n}\right) + \frac{C_2}{n}, \\
V_3(i,1) &= V_3(i-1, M-1) \cdot \left(1 - \frac{C_2}{n}\right), \\
&\vdots \\
V_M(i,1) &= V_M(i-1, M-1) \cdot \left(1 - \frac{C_2}{n}\right), \\
V_1(i,2) &= V_1(i,1) \cdot \left(1 - \frac{C_3}{n}\right), \\
V_2(i,2) &= V_2(i,1) \cdot \left(1 - \frac{C_3}{n}\right), \\
V_3(i,2) &= V_3(i,1) \cdot \left(1 - \frac{C_3}{n}\right) + \frac{C_3}{n}, \\
V_4(i,2) &= V_4(i,1) \cdot \left(1 - \frac{C_3}{n}\right), \\
&\vdots \\
V_M(i,2) &= V_M(i,1) \cdot \left(1 - \frac{C_3}{n}\right),
\end{aligned}$$

For a given rock sample with known volume fractions of the components (e.g., from laboratory measurements), the initial concentration of each phase for the model input can be determined from (4)–(8), based on the assigned incremental number n .

To demonstrate the effects of the order of mixing the different inclusions on the simulation results and their dependence on the iteration number n , we show in Figure 3 the modeling results for a hypothetical sample composed of brine (with relative permittivity and conductivity of 79 and 4.69 S/m, resp.) and 3 groups of quartz grains aligned 0° , 30° , and 90° to the bedding, respectively. The sample has a porosity of 0.1, and the quartz inclusions with alignment of 0° , 30° , and 90° to the bedding have volume fractions of 0.6, 0.2, and 0.1, respectively. The aspect ratios of all the quartz minerals are assumed to be 0.1, and the relative permittivity and conductivity are taken to be 20 and 10^{-5} S/m, respectively. In the example, the calculations at each iteration number are made using 6 different mixing orders of the 3 inclusions, as shown in the legend where 0, 30, and 90 stand for the quartz oriented 0° , 30° , and 90° to the bedding, respectively, and their orders in the legend represent the mixing order of the corresponding ingredients. The big separation between the simulated relative permittivity and conductivity when n is set to be 1 confirms that the conventional DEM model is dependent on the mixing order of the multiple components (e.g., [15, 32, 33]). With an increase in the iteration number, the ordering effect decreases, and the calculated relative permittivity and conductivity at each direction start to converge and become identical when the iteration number

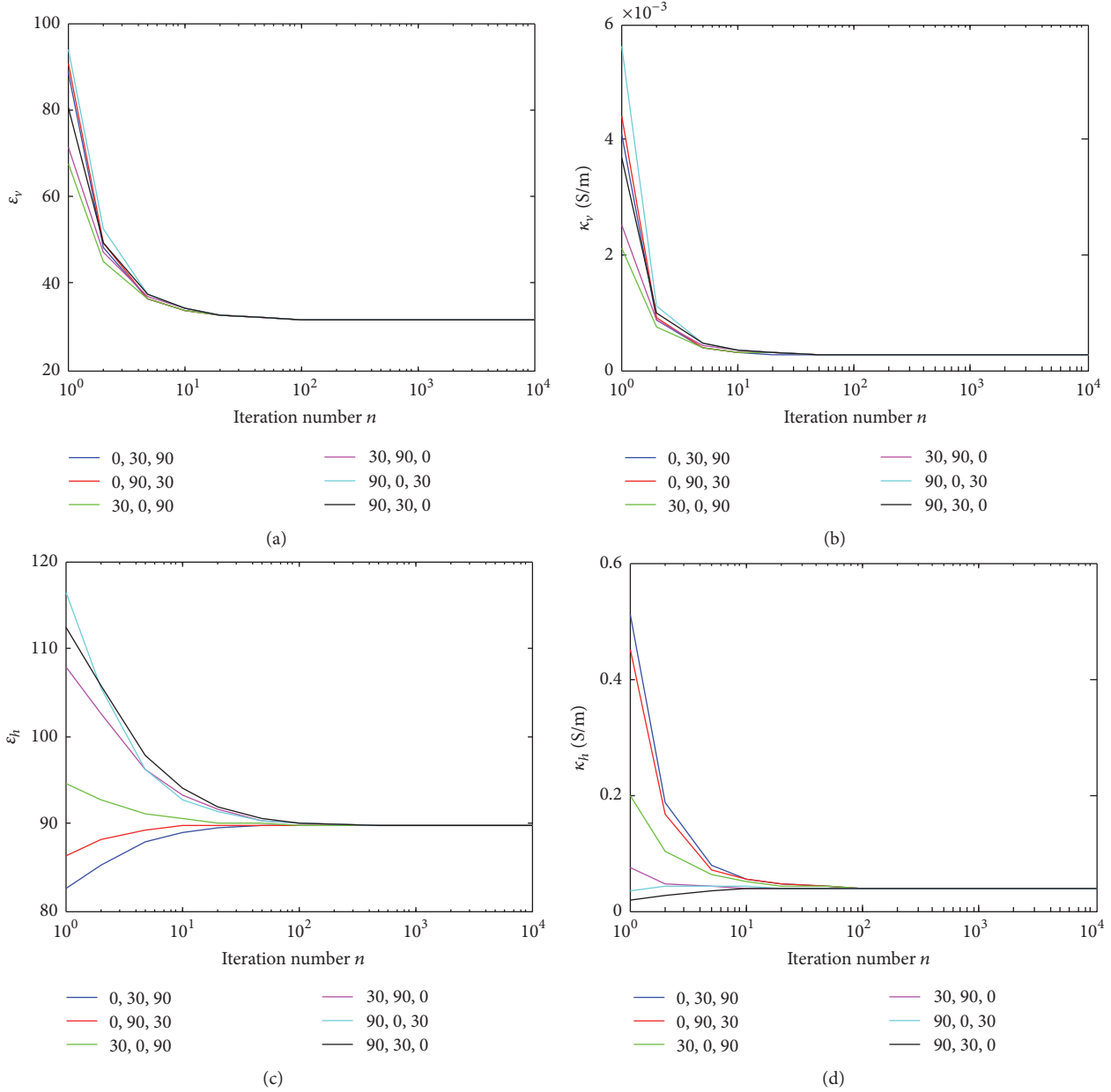


FIGURE 3: Simulated relative permittivity and conductivity of the hypothetical sample in the directions when the applied electric field is perpendicular (ϵ_v and κ_v , resp.) and parallel (ϵ_h and κ_h , resp.) to the bedding, respectively. The lines with varying colors are for the quartz grains with different mixing orders, where 0, 30, and 90 stand for the quartz oriented 0° , 30° , and 90° to the bedding, respectively.

is sufficiently high (i.e., when $n = 1000$), demonstrating that the developed multiphase anisotropic dielectric model is independent of mixing order at high iteration numbers. A further increase in the iteration number will not affect the results but may cause an increase in the computing time. Therefore, unless otherwise stated, an iteration number of 1000 is used for the rest of the calculations to guarantee accuracy of the simulation results in a quick manner.

3. Application to Artificial Shales

3.1. Sample Selection. Having developed the multiphase anisotropic dielectric model, we proceed to apply the model

to simulating the laboratory measured frequency dependent dielectric responses of the artificial shales presented in the companion paper. To do this, as mentioned previously, the frequency dependent dielectric properties of the rock-forming components, their volume fractions, and geometric information are needed as the inputting model parameters. While the dielectric properties of the insulating silt and the conductive water can be regarded frequency independent in the frequency range between 0.1 MHz and 100 MHz, there is evidence that the dielectric properties of wet clay minerals are frequency dependent as a result of the Stern layer polarization associated with clay minerals (e.g., [34]). Since the magnitude of the Stern layer polarization depends on the water salinity,

TABLE 1: Volume fractions of the rock-forming components for the model input of the 3 samples under investigation. The volume fractions are determined based on the measured sample porosity, the solid silt to kaolinite ratio, and the obtained orientation distribution function of the kaolinite grains.

Sample	φ	V_{silt}	V_{kao}^0	V_{kao}^{30}	V_{kao}^{60}	V_{kao}^{90}
A0100_75	0.18	0	0.4756	0.2303	0.0682	0.0459
A2575_75	0.158	0.2105	0.4111	0.1792	0.0285	0.0127
A4060_75	0.14	0.3440	0.2893	0.1614	0.0429	0.0224

the dielectric properties of wet clay minerals are also related to the properties of water. It is therefore reasonable to select a series of samples (in disc shape with diameter of 20 mm and thickness of 3–5 mm) saturated with the same brine but with varying clay to silt ratios so that the frequency dependent dielectric properties of the wet clay minerals at this specific brine conditions can be inverted based on the developed model from the measured dielectric behaviors of the sample with no silt fraction (i.e., the sample composed of only kaolinite and brine). Samples fulfilling this criterion include the dispersed samples saturated with distilled water (i.e., samples D0100_0 and D4555_0) and the aggregated samples filled with 75 g/l KCl brine (i.e., samples A0100_75, A2575_75, and A4060_75). Considering the fact that the contributions to the dielectric responses of the distilled water saturated shales are mainly from the Stern layer polarization which overwhelms the Maxwell–Wagner polarization, based on which the multiphase dielectric model is developed, therefore, only the aggregated shales samples saturated with 75 g/l KCl are selected for the modeling.

3.2. Determination of the Volume Fractions of the Ingredients.

We use the measured porosity, preset silt to kaolinite weight ratios, and the collected orientation distributions of the kaolinite grains (as shown in Figure 4 for all the 3 samples in consideration) to determine the volume fractions of the ingredients, which are essential for the model inputs. The clay particle orientation distributions are measured using neutron diffraction goniometry at polar angle interval of 5° , giving rise to 19 data points in the range 0° to 90° . Although the multiphase model is developed for any number of phases, the 19 clay phases will significantly increase the computing time. To simplify the clay orientation distributions but to keep the effects of the distribution density on the dielectric anisotropy, we choose 4 representative angles instead of using the complete orientation distributions. This is done by averaging the obtained distribution densities, respectively, between 0° and 15° , 20° and 40° , 50° and 70° , and 75° and 90° to represent the orientation distributions at 0° , 30° , 60° , and 90° , respectively. Considering the fact that kaolinite and silt grains are similar in densities (the densities of the kaolinite and quartz were determined to be 2.61 g/cm^3 and 2.65 g/cm^3 , respectively), the volume fractions of the kaolinite at the 4 polar angles (V_{kao}^i) and the volume fraction of the silt (V_{silt}) are then determined as

$$V_{\text{kao}}^i = (1 - \varphi) W_{\text{kao}} \frac{d_{\text{kao}}^i}{\sum_{i=0,30,60,90} d_{\text{kao}}^i}, \quad (9)$$

$$V_{\text{silt}} = (1 - \varphi) W_{\text{silt}},$$

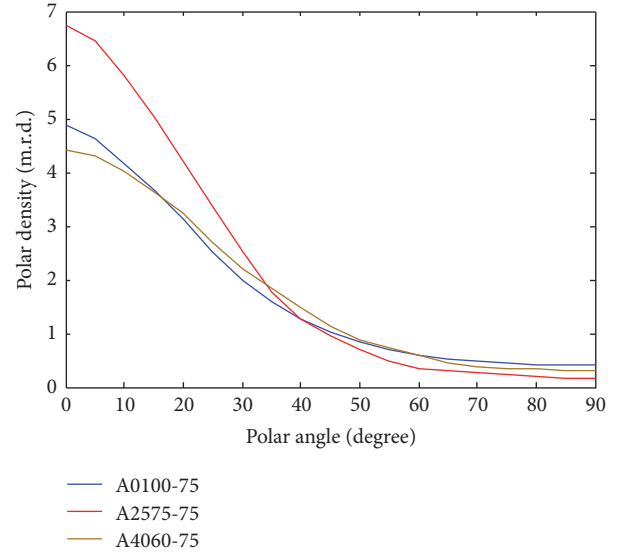


FIGURE 4: Experimental c -axis distribution density figures of the kaolinite in the 3 samples with corresponding integrated polar angle profiles. Distribution density is expressed in multiples of random distribution (m.r.d.).

where φ is the porosity of the artificial shale sample, W_{silt} and W_{kao} are the preset weight ratio between silt and kaolinite, and d_{kao}^i are the averaged orientation distribution densities at 0° , 30° , 60° , and 90° , respectively.

The calculated volume fractions of the ingredients for all the 3 samples are listed in Table 1, and the initial concentrations of the various phases C that are directly input into the model can be obtained from (4)–(8), based on the assigned incremental number $n = 1000$.

3.3. Inversion of the Dielectric Properties of Wet Clays.

To obtain the unknown dielectric properties of the wet clay minerals that are dependent on the brine (among many other factors including grain size and temperature) saturating the shale samples, we invert the measured dielectric behaviors of the artificial sample made of pure kaolinite and the same brine filling the other 2 samples, that is, the 75 g/l KCl brine with relative permittivity of 79 and electrical conductivity of 11.2 S/m . The inversion is done on sample A0100_75 by minimizing the difference between the laboratory measurements and the model prediction for relative permittivity and conductivity in the directions parallel and perpendicular to the bedding, respectively, at each frequency between 0.1 MHz and 100 MHz where the laboratory data are collected. In the

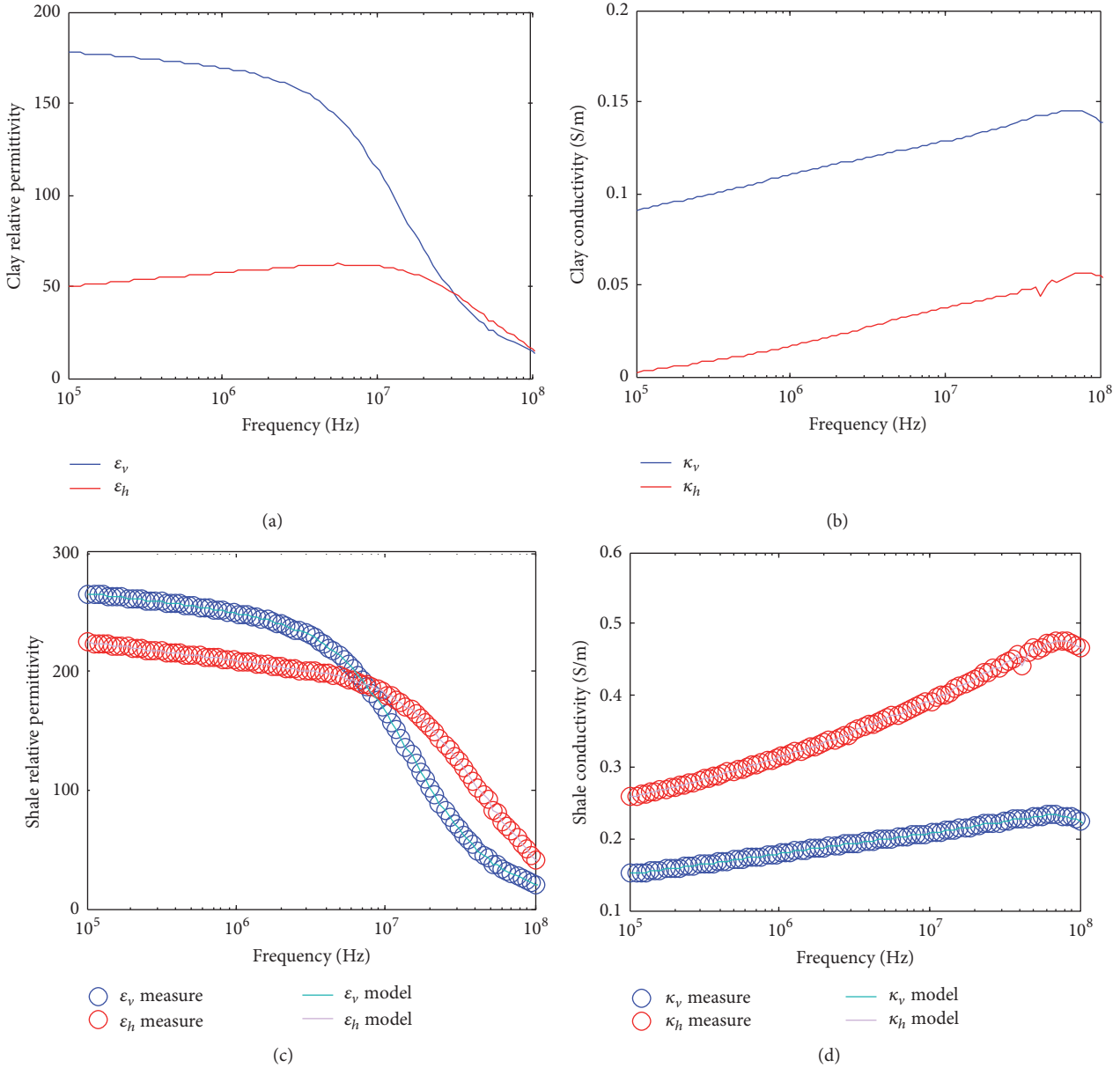


FIGURE 5: Inverted frequency dependent relative permittivity (a) and conductivity (b) of the wet kaolinite and comparison of the laboratory measured relative permittivity (c) and conductivity (d) of the shale sample A0100.75 with the model prediction based on the wet kaolinite properties in the vertical and horizontal directions, respectively.

modeling, an aspect ratio of 0.1 is employed for the kaolinite grains based on analysis of the SEM images of the compacted sample [35].

The results are given in Figure 5 for the inverted frequency dependent relative permittivity and electrical conductivity of the wet kaolinite in the vertical (perpendicular to the bedding, in blue curves) and horizontal (parallel to the bedding, in red curves) directions, respectively. Also shown in Figure 5 is the comparison of the measured shale (A0100.75) relative permittivity and conductivity (vertical and horizontal, resp.) with those predicted using the developed anisotropic model based on the inverted wet clay dielectric properties and their simplified orientation distributions.

The wet clay dielectric properties obtained in the vertical and horizontal directions are for the brine coated oblate kaolinite grains in the directions along the short and long axis, respectively. These properties are thought to be a result of the Stern layer polarization only that is dependent merely on the brine properties and are assumed to be the properties of the wet clay in the artificial shales saturated with the same brine. The anisotropic wet clay dielectric properties are further employed to account for the Maxwell–Wagner polarization through the developed multiphase model to predict the anisotropic dielectric behaviors of the shales with varying amounts of silt fractions. It should be noted that the excellent agreement between the laboratory data and the

model prediction as shown in Figures 5(c) and 5(d) is not an indication of the correctness of either the new model or the inverted wet clay dielectric properties but does imply that the combination of them can sufficiently simulate the measured frequency dependent dielectric behaviors of the silt-free shale sample. It is therefore reasonable to expect that the joint employment of the developed model and the obtained wet clay dielectric properties could also give satisfactory simulation to the artificial samples with the silt fractions, as to be shown in the next section.

3.4. Modeling Results. Having selected qualified artificial shale samples, having determined the volume fractions of their ingredients, and having obtained the frequency dependent dielectric properties of wet kaolinite clay aggregates form a basis for the developed multiphase model to simulate the measured anisotropic responses of the shale samples with silt fractions, which makes the artificial samples more resembling natural shales in terms of their mineral compositions. The inclusion of the silt fractions, however, will add additional complexity to the model.

Firstly, the distribution of the silt fractions turns to be random in the kaolinite matrix, making the shale less anisotropic. To adjust the developed multiphase anisotropic dielectric model to be capable of adding isotropic inclusions, the 2-phase anisotropic dielectric model (see (1)) is replaced with the 2-phase isotropic model when the silt component is added, given as follows [27]:

$$\varepsilon^* = \varepsilon_a^* \left[1 + \frac{1}{3} \Phi \sum_{k=x,y,z} \frac{\varepsilon_g^* - \varepsilon_a^*}{\varepsilon_a^* + (\varepsilon_g^* - \varepsilon_a^*) L_k} \right]. \quad (10)$$

Secondly, the dielectric properties of wet silt are unknown. It is well documented in the literature that dry quartz mineral has a relative permittivity of approximately 4.5 (e.g., [36]), but wet quartz exhibits higher values due to the electrochemical interactions of the mineral-water system. In this work, a constant relative permittivity of 20 [37, 38] is employed for wet silt with an electrical conductivity of 10^{-5} S/m. The high relative permittivity value for the wet silt can be explained by the polarization at the mineral-water surface and/or by the fact that there are small amount of silt grains with high aspect ratio, which give rise to high relative permittivity at relative low frequencies [39]. And lastly, the geometric information (i.e., aspect ratio) of the silt fractions that is required for the model input needs to be determined. In this work, the silt aspect ratio is set as a fitting parameter to give the best correlation coefficient between laboratory measurements (both relative permittivity and conductivity) and model prediction in the vertical and horizontal directions, respectively.

Using the dielectric properties of the various ingredients together with their volume fractions (as listed in Table 1) and aspect ratios, the built anisotropic multiphase dielectric model is applied to the artificial shale samples of A2575_75 and A4060_75 based on the procedures outlined above.

The modeling results for the artificial shale sample A2575_75 are given in Figure 6. By using the silt aspect ratios of 0.1 and 0.06 the modeled dielectric responses give

satisfactory fit to the dielectric measurements at the vertical and horizontal directions, respectively, with correlation coefficients of $R = 0.9833$ and $R = 0.9775$ for the relative permittivity and conductivity in the vertical direction and $R = 0.9979$ and $R = 0.9940$ for the relative permittivity and conductivity in the horizontal direction, respectively. The obtained silt aspect ratios of 0.1 and 0.06 are within the aspect ratio range of the silt from the micro-CT image of the compacted sample [35] and can also be explained by the nonhomogeneous microstructure at the sample scale [40]. It is interesting that different values of the silt aspect ratio are inverted in the orthogonal directions and this can be explained by the fact that although randomly dispersed silts are assumed in the model, they are in fact aligned to some extent, and therefore their contributions to the dielectric responses at different directions are varying; as a result, different values for the silt grain aspect ratio should be used. This is similar to the distinct wet clay dielectric properties that are employed to model the anisotropic shale properties in the different directions.

Figure 7 shows the modeling results for the sample A4060_75. When the silt grain aspect ratio is determined to be 0.1 for both vertical and horizontal directions, the new multiphase anisotropic dielectric model gives best fit to the laboratory measurements with correlation coefficients of $R = 0.9921$ and $R = 0.9433$ for the vertical relative permittivity and conductivity and $R = 0.9971$ and $R = 0.9943$ for the relative permittivity and conductivity horizontally, respectively. The inverted silt aspect ratio is consistent with the results obtained for the sample A2575_75 with less silt content and the uniform silt aspect ratio for the orthogonal directions indicates that the silt grains are more homogeneously distributed in the sample so that the dielectric properties of the rock caused by the silt component can be effectively described by the isotropic model (see (10)).

4. Discussion

The multiphase anisotropic dielectric model was developed based on the incremental algorithm [21, 28], in which a small amount of each component is required to be added in every increment, making the model independent of the mixing order, a problem usually encountered by multiphase DEM models [15, 32, 33]. This excludes the difference in the results caused by the order of mixing the different mineral phases and ensures that the results are unique for the determined shale dielectric properties based on the dielectric responses and volume fractions of the constituents and their specific microstructure described by the simplified orientation distribution function of the clay particles, which determines the anisotropy of the bulk dielectric properties through the orientational alignments of the clay minerals. A complete orientation distribution of the clay minerals as measured may give better anisotropic results for the model, but will also increase dramatically the computing time due to the repeated incremental addition of the more directional phases. It turns out that the simplified clay orientation distribution function as proposed above is a reasonable compromise that gives excellent model to laboratory data fit at relatively lower simulation costs.

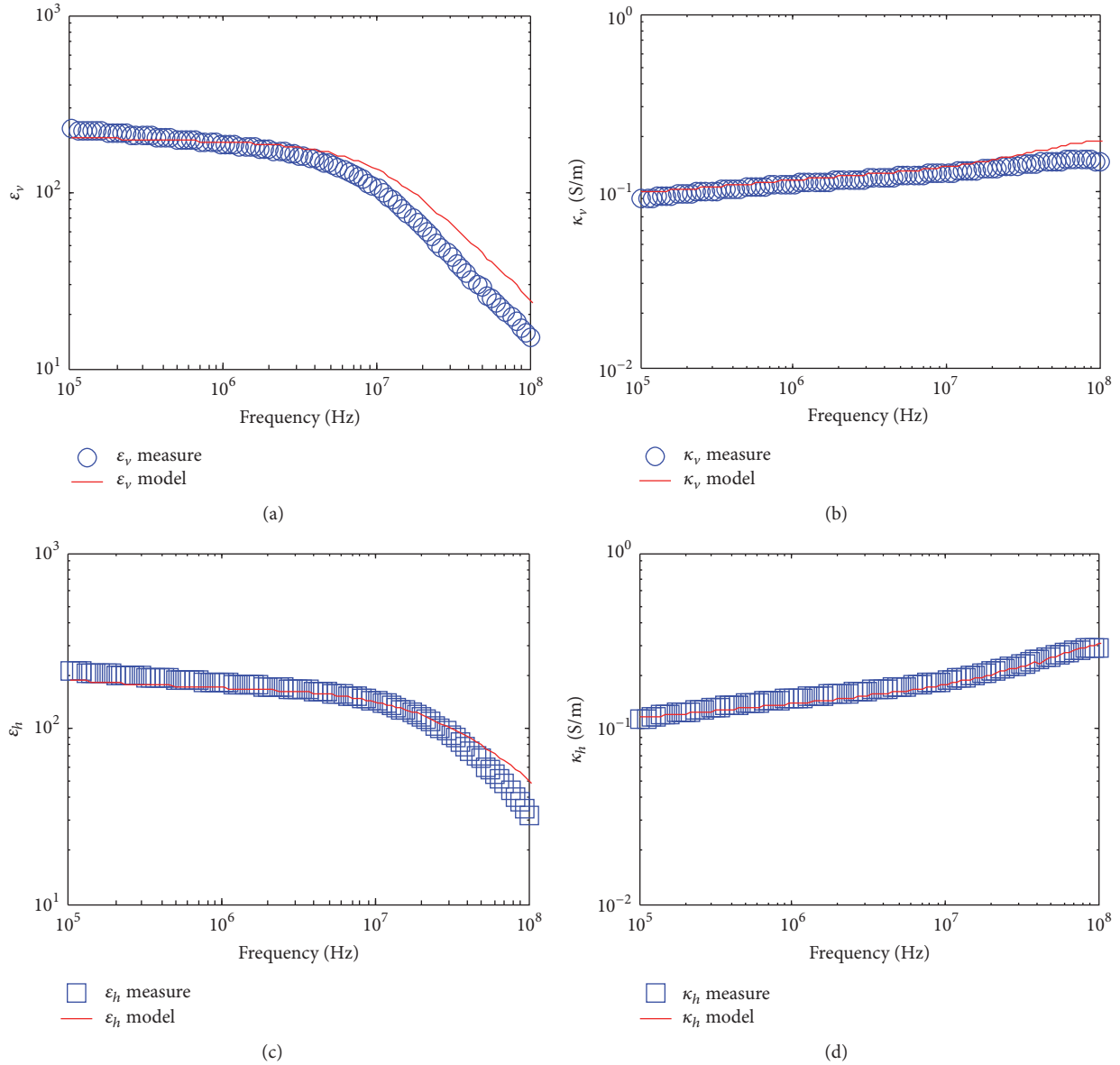


FIGURE 6: Comparison of the experimental measurements with the modeling results for the artificial shale sample A2575_75. The correlation coefficients are $R = 0.9833$ and $R = 0.9775$, respectively, for the relative permittivity and conductivity in the vertical direction and $R = 0.9979$ and $R = 0.9940$ for the relative permittivity and conductivity in the horizontal direction, respectively.

The direction dependent dielectric properties of the wet clay aggregates as a function of frequency are inverted from the silt-free artificial shale sample using the built multiphase dielectric model. Since the Maxwell–Wagner polarization has already been accounted for by the new model, the obtained anisotropic dielectric properties of the wet clay minerals are thought to be the results of all other types of polarization mechanisms including the Stern layer polarization in the directions along the axes of the clay particles coated by the specific 75 g/l KCl brine. The obtained wet clay dielectric properties can be validated by the models based on Stern layer polarization (e.g., [34]); however such models usually need additional parameters (e.g., formation factor and cation exchange capacity of the sample and

electrochemical properties of the pore filling brine) which are not available from the experiments presented in the companion paper. Nevertheless, as mentioned in the context, through the inverted wet clay dielectric properties, the proposed modeling approach combines the Stern layer and Maxwell–Wagner polarization mechanisms in the intermediate frequency range 0.1 MHz–100 MHz, which is a clear advantage of the model over other theoretical models that deal with only one of the polarization mechanisms.

In addition to the anisotropic dielectric properties of the wet clay minerals, the shale dielectric anisotropy in the modeling is caused exclusively by the aligned clay minerals and the silt grains are assumed to be randomly dispersed, which leads to isotropic dielectric properties if the background is

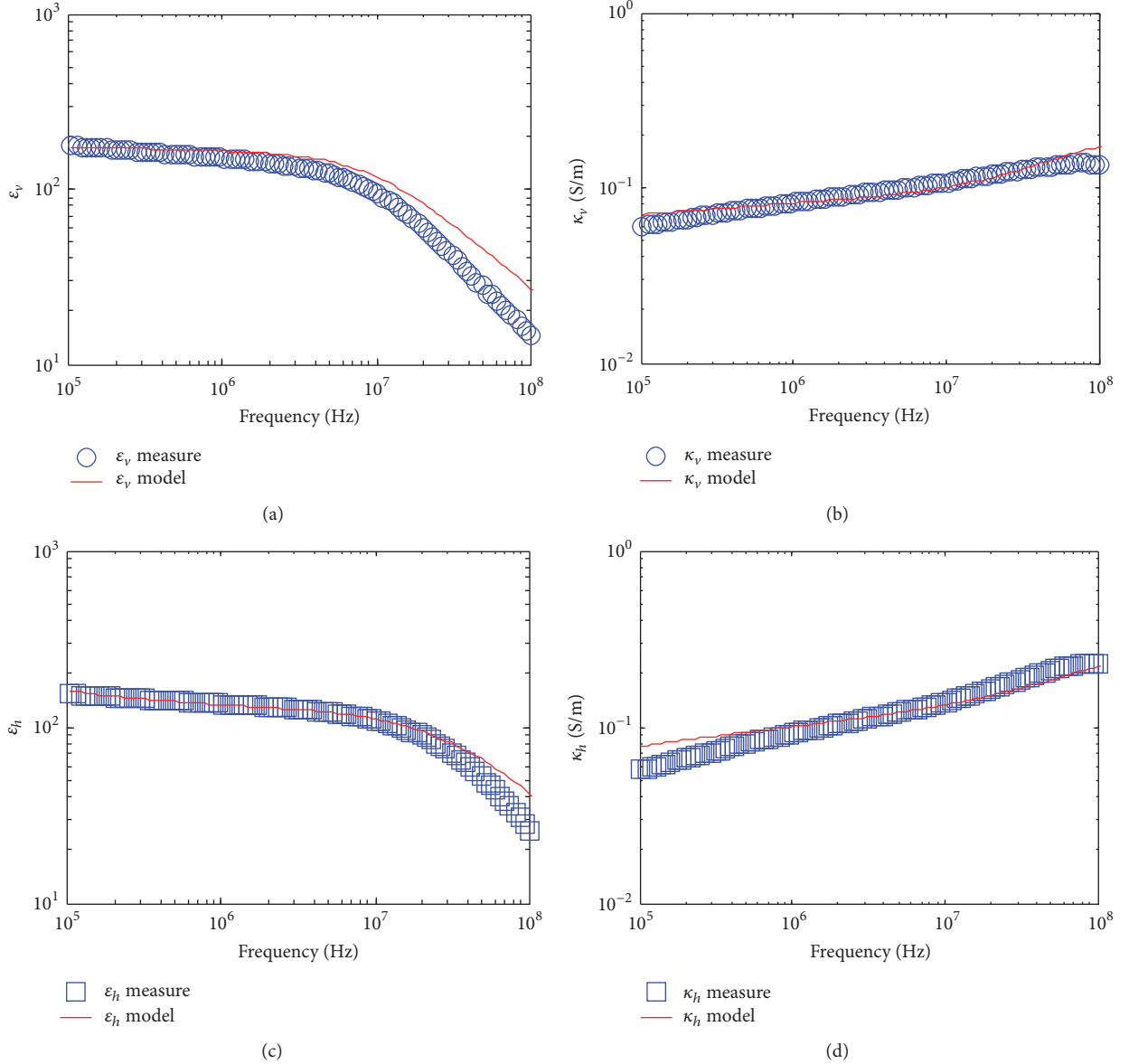


FIGURE 7: Comparison of the experimental measurements with the modeling results for the artificial shale sample A4060_75. The correlation coefficients are $R = 0.9921$ and $R = 0.9433$, respectively, for the relative permittivity and conductivity in the vertical direction and $R = 0.9971$ and $R = 0.9943$ for the relative permittivity and conductivity in the horizontal direction, respectively.

homogeneous and reduces anisotropy if the host matrix is anisotropic. The 2-phase isotropic model [27] is therefore employed to account for the dielectric properties when the silt fractions are included. However, the different silt aspect ratios obtained from the inversion for sample A2575_75 of the 2 orthogonal directions indicates that the contributions of the silt grains to the bulk dielectric behaviors are dependent on the directions, which in turn implies that the silt grains are not randomly distributed as assumed, which will originate additional anisotropy to the sample [40]. A detailed laboratory investigation of the orientation distribution of the silt grains is needed to enable the developed multiphase model to better simulate the anisotropic dielectric properties of shales, and this will be one of the topics for a future study.

The wet clay dielectric properties are frequency dependent in the modeling, while the relative permittivity and conductivity of the wet silt grains are assumed to be constant over the frequency range under investigation. It should be noted, however, that the dielectric responses of wet quartz should also be a function of the applied electrical field frequency, due to the electrochemical interactions of the mineral-water system that give additional contribution to the rock dielectric properties [6, 37, 38]. To better determine the frequency dependent dielectric properties of the wet silt, a separate experiment measuring the relative permittivity and conductivity of the silt and 75 g/l KCl brine mixture as a function of frequency is needed, and an inversion algorithm as presented in the context to obtain the frequency dependent

dielectric properties of the wet clay minerals can be implemented to remove the effects caused by the Maxwell–Wagner polarization to finally arrive at the dependence of the wet silt dielectric properties on frequency that is a result merely of the Stern layer polarization. The derived relative permittivity and conductivity of the wet silt are essentially the effective values resulting from the electrochemical Stern layer polarization at each frequency [41].

The proposed modeling approach can be applied to calibrating and comparing the results of different geophysical methods that acquire the dielectric properties from different directions (i.e., dielectric logging from the horizontal direction and surface Induced Polarization method from the vertical direction) in addition to determining the geofluids type and concentration and estimating the transport properties of the shales. Another important potential application of the modeling is for the detection and prediction of overpressure in shales due to their extremely low permeability that makes the pore pressure less able to equilibrate to hydrostatic pressure. Accurate overpressure detection and prediction play an important role in understanding the depositional and evolutionary history of a sedimentary basin, hydrocarbon migration, and trapping in the reservoir, as well as in reducing the risks of drilling hazards during hydrocarbon exploitation [42–45]. Overpressure results in lower than expected electrical resistivity (reciprocal of conductivity) through the enlarged porosity associated with the high pore pressure, and conventional overpressure prediction models based on electrical properties evaluate the difference between the measured electrical properties and those of the normally compacted shales at the same depth to estimate the abnormal pore pressure [46, 47]. Since the developed multiphase dielectric model does not take into account the pressure effects, the modeled shale electrical properties can then be regarded as the electrical properties of the shales if the pore pressure is normal (i.e., the normally compacted shale electrical properties), which can be further employed for the overpressure prediction based on their difference from the measured electrical anomalies. Application of the multiphase model to the overpressure detection and prediction in shales will be a topic for a future study.

5. Conclusions

A multiphase incremental model has been developed for the anisotropic dielectric properties of sedimentary rocks. The model is for any number of mineral grain components aligned in any direction and is independent of the mixing order. Based on the new model, we propose a modeling approach for the frequency dependent anisotropic dielectric properties of shales in which the shale anisotropy is determined from the measured orientation distribution function of the clay particles and the dielectric properties of the wet clay minerals are inverted from the obtained dielectric behaviors of the artificial shale sample composed of clay and brine that is the same as that used in other shale samples. The method combines the two important polarization mechanisms (i.e., the Stern layer polarization and the Maxwell–Wagner polarization, resp.) taking effect

in the intermediate frequency range of 0.1 MHz–100 MHz. Application of the modeling approach to the artificial shale samples with varying silt contents show that the frequency dependent relative permittivity and conductivity of the shales in the two orthogonal directions can be satisfactorily modeled by using a reasonable aspect ratio and constant dielectric parameters for the silt grains.

Conflicts of Interest

The authors declare that they have no conflicts of interest.

Acknowledgments

The authors would like to thank the CSIRO Shale Rock Physics and Petrophysics (SHARPP) project sponsored by Total and the Strategic Research Program of the Chinese Academy of Sciences (XDA14010303) for financial support of this work.

References

- [1] C. Clavier, G. Coates, and J. Dumanoir, “Theoretical and experimental bases for the dual-water model for interpretation of shaly sands,” *SPE Journal*, vol. 24, no. 2, pp. 153–168, 1984.
- [2] O. A. L. De Lima and M. M. Sharma, “A grain conductivity approach to shaly sandstones,” *Geophysics*, vol. 55, no. 10, pp. 1347–1356, 1990.
- [3] P. W. Glover, P. G. Meredith, P. R. Sammonds, and S. A. Murrell, “Ionic surface electrical conductivity in sandstone,” *Journal of Geophysical Research: Solid Earth*, vol. 99, no. B11, pp. 21635–21650, 1994.
- [4] A. Rabautte, A. Revil, and E. Brosse, “In situ mineralogy and permeability logs from downhole measurements: application to a case study in chlorite-coated sandstones,” *Journal of Geophysical Research: Atmospheres*, vol. 108, no. 108, pp. 369–378, 2003.
- [5] P. Leroy, A. Revil, A. Kemna, P. Cosenza, and A. Ghorbani, “Complex conductivity of water-saturated packs of glass beads,” *Journal of Colloid and Interface Science*, vol. 321, no. 1, pp. 103–117, 2008.
- [6] A. Revil and M. Skold, “Salinity dependence of spectral induced polarization in sands and sandstones,” *Geophysical Journal International*, vol. 187, no. 2, pp. 813–824, 2011.
- [7] N. Schwartz and A. Furman, “Spectral induced polarization signature of soil contaminated by organic pollutant: experiment and modeling,” *Journal of Geophysical Research: Atmospheres*, vol. 117, no. B10, Article ID B10203, 10203 pages, 2012.
- [8] A. Revil, W. F. Woodruff, C. Torres-Verdín, and M. Prasad, “Complex conductivity tensor of anisotropic hydrocarbon-bearing shales and mudrocks,” *Geophysics*, vol. 78, no. 6, pp. D403–D418, 2013.
- [9] O. Stern, “Zur theorie der elektrolytischen doppelschicht (the theory of the electrolytic double shift),” *Zeitschrift Fur Elektrochemie Und Angewandte Physikalische Chemie*, vol. 30, pp. 508–516, 1924.
- [10] L. K. H. van Beek, “Dielectric behaviour of heterogeneous systems,” in *Progress in Dielectrics*, vol. 7, pp. 69–114, Heywood Books, London, 1967.
- [11] P. N. Sen, C. Scala, and M. H. Cohen, “A self-similar model for sedimentary rocks with application to the dielectric constant of fused glass beads,” *Geophysics*, vol. 46, no. 5, pp. 781–795, 1981.

- [12] J. G. Berryman, "Mixture theories for rock properties," in *Rock Physics & Phase Relations*, vol. 3, pp. 205–228, American Geophysical Union, Washington, D. C., USA, 1995.
- [13] L.-J. Gelius and Z. Wang, "Modelling production caused changes in conductivity for a siliciclastic reservoir: a differential effective medium approach," *Geophysical Prospecting*, vol. 56, no. 5, pp. 677–691, 2008.
- [14] M. H. Ellis, M. C. Sinha, T. A. Minshull, J. Sothcott, and A. I. Best, "An anisotropic model for the electrical resistivity of two-phase geologic materials," *Geophysics*, vol. 75, no. 6, pp. E161–E170, 2010.
- [15] T. Han, A. I. Best, L. M. MacGregor, J. Sothcott, and T. A. Minshull, "Joint elastic-electrical effective medium models of reservoir sandstones," *Geophysical Prospecting*, vol. 59, no. 4, pp. 777–786, 2011.
- [16] J. G. Berryman and G. M. Hoversten, "Modelling electrical conductivity for earth media with macroscopic fluid-filled fractures," *Geophysical Prospecting*, vol. 61, no. 2, pp. 471–493, 2013.
- [17] P. W. J. Glover, "A generalized Archie's law for n phases," *Geophysics*, vol. 75, no. 6, pp. E247–E265, 2010.
- [18] W. Wei, J. Cai, X. Hu, and Q. Han, "An electrical conductivity model for fractal porous media," *Geophysical Research Letters*, vol. 42, no. 12, pp. 4833–4840, 2015.
- [19] J. Cai, W. Wei, X. Hu, and D. A. Wood, "Electrical conductivity models in saturated porous media: a review," *Earth-Science Reviews*, vol. 171, pp. 8419–8433, 2017.
- [20] P. N. Sævik, M. Jakobsen, M. Lien, and I. Berre, "Anisotropic effective conductivity in fractured rocks by explicit effective medium methods," *Geophysical Prospecting*, vol. 62, no. 6, pp. 1297–1314, 2014.
- [21] C. Berg, "An effective medium algorithm for calculating water saturations at any salinity or frequency," *Geophysics*, vol. 72, no. 2, pp. E59–E67, 2007.
- [22] P. Cosenza, C. Camerlynck, and A. Tabbagh, "Differential effective medium schemes for investigating the relationship between high-frequency relative dielectric permittivity and water content of soils," *Water Resources Research*, vol. 39, no. 9, 1230 pages, 2003.
- [23] D. A. Bruggeman, "Berechnung verschiedener physikalischer Konstanten von heterogenen Substanzen," *Annalen der Physik*, vol. 416, no. 7, pp. 636–664, 1935.
- [24] T. Hanai, "Theory of the dielectric dispersion due to the interfacial polarization and its application to emulsions," *Colloid and Polymer Science*, vol. 171, no. 1, pp. 23–31, 1960.
- [25] T. Hanai, "A remark on the "Theory of the dielectric dispersion due to the interfacial polarization";," *Colloid and Polymer Science*, vol. 175, no. 1, pp. 61–62, 1961.
- [26] A. E. Bussian, "Electrical conductance in a porous medium.," *Geophysics*, vol. 48, no. 9, pp. 1258–1268, 1983.
- [27] K. Asami, "Characterization of heterogeneous systems by dielectric spectroscopy," *Progress in Polymer Science*, vol. 27, no. 8, pp. 1617–1659, 2002.
- [28] T. Han, M. B. Clennell, M. Josh, and M. Pervukhina, "Determination of effective grain geometry for electrical modeling of sedimentary rocks," *Geophysics*, vol. 80, no. 4, pp. D319–D327, 2014.
- [29] T. Han, M. B. Clennell, and M. Pervukhina, "Modelling the low-frequency electrical properties of pyrite-bearing reservoir sandstones," *Marine and Petroleum Geology*, vol. 68, pp. 341–351, 2015.
- [30] J. C. Maxwell, *Treatise on electricity and magnetism*, The Clarendon Press, Oxford University Press, 1891.
- [31] K. W. Wagner, "Erklärung der dielektrischen Nachwirkungsvorgänge auf Grund Maxwellscher Vorstellungen," *Archiv für Elektrotechnik*, vol. 2, no. 9, pp. 371–387, 1914.
- [32] M. Spalburg, "The effective medium theory used to derive conductivity equations for clean and shaly hydrocarbon-bearing reservoirs," in *Proceedings of the 11th European Formation Evaluation Symposium*, 1988.
- [33] P. Cosenza, A. Ghorbani, C. Camerlynck, F. Rejiba, R. Guérin, and A. Tabbagh, "Effective medium theories for modelling the relationships between electromagnetic properties and hydrological variable in geomaterials: a review," *Near Surface Geophysics*, vol. 7, no. 5–6, pp. 563–578, 2009.
- [34] A. Revil, "On charge accumulation in heterogeneous porous rocks under the influence of an external electric field," *Geophysics*, vol. 78, no. 4, pp. D271–D291, 2013.
- [35] R. Beloborodov, M. Pervukhina, V. Luzin et al., "Compaction of quartz-kaolinite mixtures: the influence of the pore fluid composition on the development of their microstructure and elastic anisotropy," *Marine and Petroleum Geology*, vol. 78, pp. 426–438, 2016.
- [36] G. R. Olhoeft, "Electrical properties of rocks," in *Physical Properties of Rocks and Minerals*, pp. 257–329, Hemisphere Publishing Corporation, New York, NY, USA, 1989.
- [37] J. L. Davis and A. P. Annan, "Ground-penetrating radar for high-resolution mapping of soil and rock stratigraphy," *Geophysical Prospecting*, vol. 37, no. 5, pp. 531–551, 1989.
- [38] D. J. Daniels, "Surface-penetrating radar—IEE Radar, Sonar, Navigation and Avionics Series 6," *The Institute of Electrical Engineers*, 1996, London, UK.
- [39] P. N. Sen, "Relation of certain geometrical features to the dielectric anomaly of rocks," *Geophysics*, vol. 46, no. 12, pp. 1714–1720, 1981.
- [40] P. Cosenza, D. Prêt, and M. Zamora, "Effect of the local clay distribution on the effective electrical conductivity of clay rocks," *Journal of Geophysical Research: Solid Earth*, vol. 120, no. 1, pp. 145–168, 2015.
- [41] O. A. L. De Lima and M. M. Sharma, "A generalized Maxwell-Wagner theory for membrane polarization in shaly sands," *Geophysics*, vol. 57, no. 3, pp. 431–440, 1992.
- [42] B. J. O. L. Mcpherson and G. Garven, "Hydrodynamics and overpressure mechanisms in the Sacramento basin, California," *American Journal of Science*, vol. 299, no. 6, pp. 429–466, 1999.
- [43] A. Muggerridge and H. Mahmode, "Hydrodynamic aquifer or reservoir compartmentalization?" *AAPG Bulletin*, vol. 96, no. 2, pp. 315–336, 2012.
- [44] M. R. P. Tingay, R. R. Hillis, R. E. Swarbrick, C. K. Morley, and A. R. Damit, "Origin of overpressure and pore-pressure prediction in the Baram province, Brunei," *AAPG Bulletin*, vol. 93, no. 1, pp. 51–74, 2009.
- [45] T. Han, M. Pervukhina, M. B. Clennell, and D. N. Dewhurst, "Model-based pore-pressure prediction in shales: an example from the gulf of Mexico, North America," *Geophysics*, vol. 82, no. 3, pp. M37–M42, 2017.
- [46] C. Hottmann and R. Johnson, "Estimation of formation pressures from log-derived shale properties," *Journal of Petroleum Technology*, vol. 17, no. 06, pp. 717–722, 1965.
- [47] J. Zhang, "Pore pressure prediction from well logs: methods, modifications, and new approaches," *Earth-Science Reviews*, vol. 108, no. 1–2, pp. 50–63, 2011.

Research Article

Experimental Characterization of Dielectric Properties in Fluid Saturated Artificial Shales

Roman Beloborodov,¹ Marina Pervukhina,² Tongcheng Han,^{3,4} and Matthew Josh²

¹Department of Exploration Geophysics, Curtin University, Perth, WA 6151, Australia

²CSIRO Energy, Perth, WA 6151, Australia

³School of Geosciences, China University of Petroleum (East China), Qingdao 266580, China

⁴Laboratory for Marine Mineral Resources, Qingdao National Laboratory for Marine Science and Technology, Qingdao 266071, China

Correspondence should be addressed to Roman Beloborodov; roman.beloborodov@postgrad.curtin.edu.au

Received 27 July 2017; Accepted 20 November 2017; Published 20 December 2017

Academic Editor: Feng Yang

Copyright © 2017 Roman Beloborodov et al. This is an open access article distributed under the Creative Commons Attribution License, which permits unrestricted use, distribution, and reproduction in any medium, provided the original work is properly cited.

High dielectric contrast between water and hydrocarbons provides a useful method for distinguishing between producible layers of reservoir rocks and surrounding media. Dielectric response at high frequencies is related to the moisture content of rocks. Correlations between the dielectric permittivity and specific surface area can be used for the estimation of elastic and geomechanical properties of rocks. Knowledge of dielectric loss-factor and relaxation frequency in shales is critical for the design of techniques for effective hydrocarbon extraction and production from unconventional reservoirs. Although applicability of dielectric measurements is intriguing, the data interpretation is very challenging due to many factors influencing the dielectric response. For instance, dielectric permittivity is determined by mineralogical composition of solid fraction, volumetric content and composition of saturating fluid, rock microstructure and geometrical features of its solid components and pore space, temperature, and pressure. In this experimental study, we investigate the frequency dependent dielectric properties of artificial shale rocks prepared from silt-clay mixtures via mechanical compaction. Samples are prepared with various clay contents and pore fluids of different salinity and cation compositions. Measurements of dielectric properties are conducted in two orientations to investigate the dielectric anisotropy as the samples acquire strongly oriented microstructures during the compaction process.

1. Introduction

Dielectric permittivity of a material is a measure of its frequency dependent electrical polarizability [1], in an applied external electric field. In the presence of an electric field, electrons, ions, and polar molecules all contribute to the frequency dependent dielectric properties. In composite materials, the build-up of charge at dissimilar conductivity boundaries and the creation of exchangeable cations may completely dominate the dielectric behaviour. For example, rock consists of liquid, solid, and gas components and each of them is clearly defined by specific chemical and/or mineral composition. Although the dielectric constants of the most of individual rock components rarely exceed 80, the bulk dielectric permittivity of a rock sample may reach many orders of magnitude at the radio frequency range (kilohertz to

megahertz), implying that not only the constituents of a rock but also their geometry, interaction, spatial arrangement, and interfaces have a significant contribution to polarization [2].

In clay bearing rocks, the presence of a connate brine results in the so-called surface effects: electric double layer polarization (i.e., Stern layer polarization) and Maxwell-Wagner space-charge polarization. They occur due to the presence of polarizable bound water at the clay-water interface and weakly bounded ions on the surface of mineral particles, which can slowly move under the influence of an external field and contribute to both the conduction and electric polarization [3]. These effects become prominent at frequencies below MHz range and complicate the interpretation of data. Figure 1 illustrates the various polarization effects with the corresponding frequency bands of their occurrence.

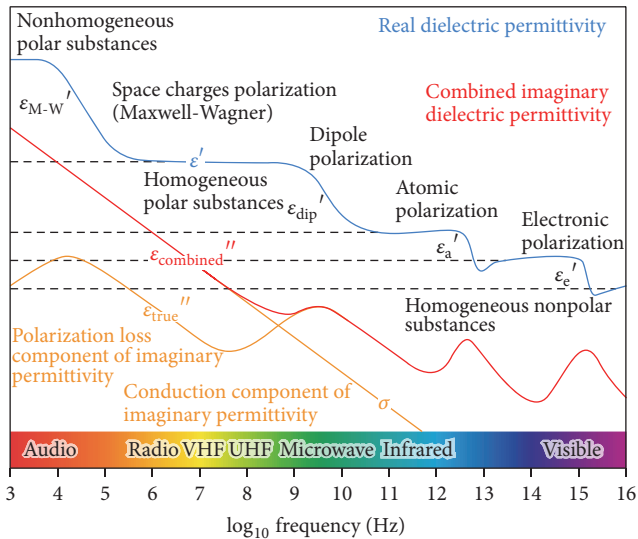


FIGURE 1: Schematics of dielectric polarization/conduction mechanisms, modified from Josh [11].

Dielectric measurements in petrophysics and petroleum industry are mostly used to determine the water content. Water molecules have a fixed electrical dipole moment and rotate quickly to align with an external electric field [4], whereas hydrocarbons have nonpolar molecules and as a result have much lower permittivity than water. Therefore, estimating moisture content from the dielectric permittivity at high frequencies ($>1\text{GHz}$) is often used in borehole petrophysics. However, dielectric logging at frequencies of 1GHz and above remains challenging in field measurements due to decreased depth of electric field penetration. On the contrary, currently available commercial dielectric tools operate at multiple spot frequencies [5] to facilitate a determination of water content and CEC: dielectric response at frequencies below 50MHz is more affected by the surface effects described above [6]. At lower frequencies, clay content, geometry and spatial orientations of mineral rock constituents, and the salinity of pore fluid also affect the measured dielectric permittivity [7, 8].

Some recent studies suggest alternative methods for oil recovery in unconventional reservoirs that utilize dielectric heating [9]. This technology allows increasing economical efficiency of exploration and reducing the ecological impact on the environment. It heavily relies on knowledge of the dielectric behaviour in kilohertz-megahertz range of frequencies where the depth of electric field penetration is sufficient for field applications and the dielectric loss-factor exhibits peak values [10]. However, interplay of several physical effects results in wide dispersion of dielectric relaxation peaks at frequencies below gigahertz. Identifying of the frequencies of these attenuation peaks as well as estimation of the range of dielectric dispersion for specific types of rock would be useful for tuning the frequency of dielectric heating tools to ensure the energy efficient and productive heating.

Another purpose of dielectric measurements is the estimation of cation exchange capacity (CEC), a property that is

directly attributed to mineral composition and specifically to clay content. Josh [11] showed a strong correlation between dielectric response at $\sim 30\text{MHz}$ and the CEC. In turn, this property is linearly proportional to the specific surface area (SSA) of a rock that determines character and amount of interparticle contacts (coordination number) under the given mineral composition and porosity of a rock. Therefore, it is expected that dielectric constant should correlate with both static and dynamic elastic properties of a rock.

It is hard to segregate and independently study different factors influencing the dielectric properties of natural shales due to the complex composition of their mineral and fluid components. There are many experimental and theoretical studies dedicated to frequency dependent dielectric properties of rocks with relation to the geometry of their components (e.g., aspect ratios and orientation of mineral grains and pores), water saturation, and organic content (e.g., [2, 12, 13]). However, there is very little evidence of studies taking into account the clay content, microstructure, and the chemical composition of pore fluid (e.g., [4, 7]). The anisotropy of dielectric properties of shales is crucial for the interpretation of dielectric well-logs especially in deviated wells and may affect the efficiency of production via the dielectric heating in unconventional shale reservoirs [14, 15]. Again, there is little to no evidence on how the anisotropy of dielectric properties of shales depend on the aforementioned parameters. The least known parameter in terms of its effect on dielectric response is the microstructure of the clay fraction in shales. Different geological settings may significantly affect the microstructure of sediment and consequently its properties [16]. For example, Dong and Wang [17] showed that the kaolinite sediments saturated with water solutions of different pH exhibit significantly different dielectric spectra due to the different mechanisms of microstructure formation.

In this work, we prepare artificial shale samples using the laboratory mechanical compaction of simple water-based mixtures of kaolinite clay and quartz powder. Our goal is to use these models of natural shales to extend our knowledge on and independently investigate the influence of clay content, microstructure, and the chemical composition of pore fluid on their frequency dependent dielectric properties and anisotropy.

2. Methodology

2.1. Sample Preparation. Artificial shale samples were prepared from mineral mixtures via mechanical compaction. In order to simplify the modelled rock and reduce uncertainties related to multiphase composition, we chose simplistic mineral components and pore fluid chemicals. Quartz and kaolinite were used for silt and clay fractions as they are the common minerals in natural shales. Compared with minerals from smectite group, kaolinite is nonswelling clay, which makes it one of the easiest clay minerals to work with. Crushed quartz powder consists of silt-sized grains.

To prepare mixtures with different types of initial clay microstructure, we utilized physicochemical approach. The presence of electrolyte in the pore fluid leads to aggregation

TABLE 1: Specification of the samples.

Name	Type of clay microstructure	Clay content (%)	Porosity (%)	Salinity (g/l)	Salt
D0100_0	Dispersed	100	21	0	-
D4555_0	Dispersed	55	10	0	-
C4	Dispersed	75	28	0	-
C5	Dispersed	60	23	0	-
A1090_0	Aggregated	90	13	0	-
A0100_10	Aggregated	100	10	10	NaCl
A0100_34	Aggregated	100	26	34	NaCl
A0100_75	Aggregated	100	18	75	KCl
A2575_75	Aggregated	75	16	75	KCl
A4060_75	Aggregated	60	14	75	KCl
C2	Aggregated	75	23	75	KCl
C3	Aggregated	60	24	75	KCl

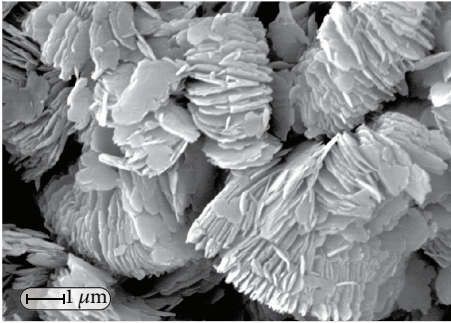


FIGURE 2: Aggregates of the kaolinite particles.

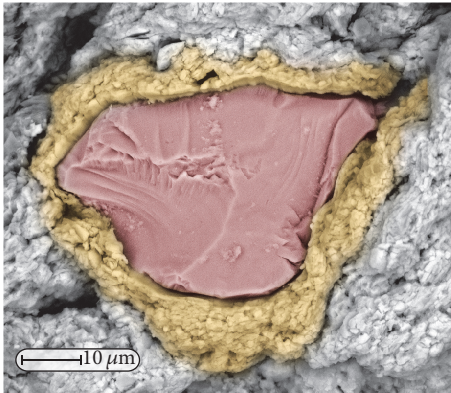


FIGURE 3: Kaolinite clay coating (in yellow) on the surface of the quartz grain (in red).

of kaolinite clay particles by means of shrinking the diffuse layer of water around the particles and sequential loss of their stability as a colloidal system [19]. Samples with aggregated clay microstructure were prepared by adding a brine solution so that clay platelets and their ultramicroaggregates (basic associations of few axially aligned individual clay platelets) combine together (Figure 2) and form the thick conforming coats on the surfaces of quartz grains (Figure 3).

It is important to note that initially untreated kaolinite powder resides in aggregated state. Thus, samples with dispersed clay microstructure were prepared by boiling mixtures with 25 ml of a dispersant – 4% sodium pyrophosphate tetrabasic, which separates existing clay aggregates into individual clay platelets and their smaller associations. This allows replacing exchangeable cations on the surfaces of clay particles with Na^+ ion so that its hydrate envelopes repulse and separate clay particles from each other.

Summary of all the prepared mixtures is shown in Table 1. Samples were named using a specific nomenclature where the first letter stands for either aggregated (A) or dispersed (D) clay microstructure; the following numbers indicate the weight ratio of quartz to kaolinite constituents in percentage, and the last number shows the salinity of a pore fluid in g/l.

2.2. Mechanical Compaction and Parallel Plate Dielectric Measurements. Samples were compacted in the high-pressure oedometer by applying uniaxial stress. Plastic pistons conduct the stress from the actuator that is manually operated with the hydraulic pump. Cell was designed to safely keep 80 MPa of the vertical stress that corresponds to ~ 3 km depth in a sedimentary basin. The oedometer was made of PEEK plastic; this material is strong enough to maintain zero lateral strain. Compacted shales were gently ejected from the oedometer, covered with thick layer of wax, and preserved in a low-temperature humid atmosphere to prevent desiccation. Further details on the mechanical compaction methodology can be found in Beloborodov et al. [16].

A subsample was cut from each of the compacted samples and its dielectric properties are measured in a parallel plate dielectric rig (Figure 4). Electrodes of the dielectric rig are made of brass and they can be changed to match the sample size. For this study, small electrodes of 1 cm in diameter were used due to the relatively small size of the subsamples ~ 2 cm in diameter. To ensure proper coupling between the electrodes of the measurement cell and maintain parallel electric field normal to the faces of the subsample disc, it was polished on a diamond surface grinder to achieve the parallel faces with $30 \mu\text{m}$ tolerance. Thickness of the

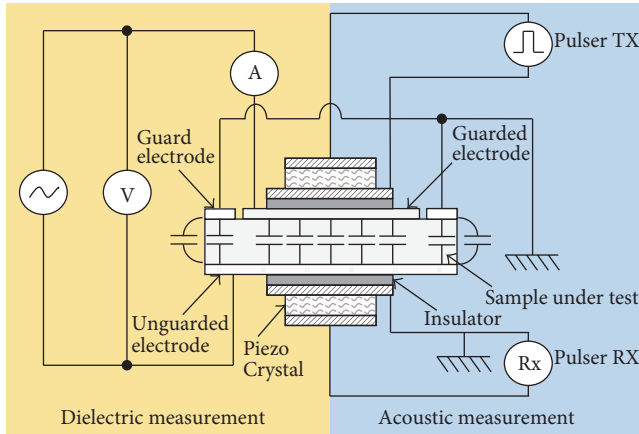


FIGURE 4: Principal scheme of the parallel plate measurement setup, modified from Josh [18].

average sample should not exceed one fifth of its diameter. The subsample discs were each placed in the parallel plate measurement cell where they were measured with an impedance analyser. The two following methods for running this device were employed. The bare coupling was used to measure the effective conductivity of the compacted samples. The disc subsample is simply placed between the parallel plate electrodes so they are in a direct contact with the bare faces of the subsample. For shales, this method provides a good conductive coupling between the rock surface and the electrodes. Coupling with insulating film was also used to block the current flow and enhance the relative contribution of polarization effects so that the frequency dispersion of real and imaginary parts of relative dielectric permittivity can be determined accurately.

Twelve artificial shale samples were prepared via the laboratory mechanical compaction. Dielectric analysis of the samples is conducted in two directions, normal (Figure 5(a)) and parallel to the bedding plane (Figure 5(b)), to investigate the dielectric anisotropy.

3. Results and Discussion

Dielectric properties are presented in Figures 6–13 for different parameters, namely, the salinity of pore fluid, its cation composition, clay content, and the type of initial clay microstructure. Figure 6 illustrates the positive linear trends of real dielectric permittivity versus porosity for the samples prepared with brine and fresh water separately. The dielectric response at frequencies of >1 GHz range is usually attributed to the dipole polarization of water molecules and might be used to estimate the amount of water in the pore space. Linear correlation decreases with a decrease in frequency from $R^2 = 0.95$ at 100 MHz to $R^2 = 0.70$ at 10 MHz due to contributions from other polarization mechanisms occurring at lower frequencies (e.g., surface-charge polarization). Although it is believed that the brine salinity has no effect on dielectric response of saturated rock samples at high frequencies, our experimental results show clearly separated trends for the

two groups of the artificial shale samples prepared with brine and fresh water. This difference is attributable to the changes occurring in the electric double layer of clays in the presence of electrolyte. In the samples saturated with highly concentrated brine the positive ions of Na and K compensate the free charges on the surfaces of clay particles. Therefore, the diffuse layer of weakly bound water around the clay particles significantly shrinks [20, 21] and leaves more free water molecules that are easily polarizable within the sample. On the other hand, the samples prepared with fresh water exhibit thick hydrate envelopes around the clay particles thereby hindering the large amount of water dipoles from polarization in the presence of an electric field. In our experimental results the described effect results in one order of magnitude difference between the samples saturated with brine and fresh water samples on a wide range of porosity at megahertz frequencies. It is also important to note that the number of active cations in brine saturated samples seems to have negligible effect on dielectric permittivity in the dipole polarization frequency range as all the samples prepared with different concentrations and compositions of brine follow the same linear trends. Using the linear trends described above, it is possible to compare different samples at the same porosity. These trends are used to investigate the effects of clay content, salinity, and microstructure.

Figure 7 shows that across the wide range of frequencies horizontal conductivity in different samples is almost always higher than the vertical one. Previously we showed that the particles of clay and silt tend to orient with compaction normal to the direction of an applied compaction stress [16, 22]. Therefore, the interconnected pore network in artificial shale samples is also more oriented in the bedding direction and provides an effective pathway for charge carriers, whereas in the direction normal to bedding the conductive pathways exhibit greater tortuosity and obstruct the movement of charges. The conductivity anisotropy also increases with porosity reduction as the microstructure becomes more oriented in horizontal direction. Both horizontal and vertical conductivities increase with increasing porosity. At high frequencies, the influence of fluid conductivity grows with increase of the pore volume occupied with water solution.

The frequency dependent dielectric anisotropy in eight artificial shale samples is shown in Figure 8. Dashed line on the plot corresponds to the isotropic system, while all the points above and below this line correspond to anisotropic system with polarization effects dominating in horizontal and vertical directions, respectively. It is important to note that the fresh water samples are always better polarized in horizontal direction and reside above the isotropy line, whereas the brine saturated samples are better polarized in vertical direction at lower frequencies and exhibit inversion of the anisotropy with crossover points in megahertz range.

The anisotropy curves for all the samples exhibit peak values in megahertz range and their maximum values and frequency distributions are determined by the type and concentration of salt ions in the saturating fluid. Thus, the samples prepared with fresh water or low concentration fluids show the highest anisotropy peaks located at the lower end of megahertz range and then follow the three peaks at the

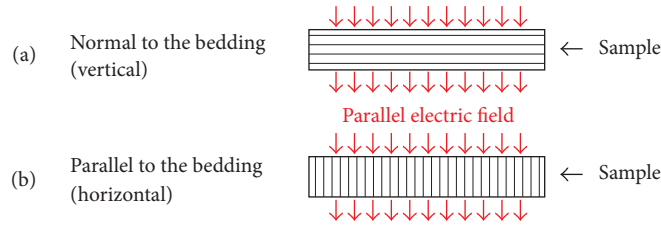


FIGURE 5: Parallel plate measurement schematics. Black lining illustrates the bedding of the sample.

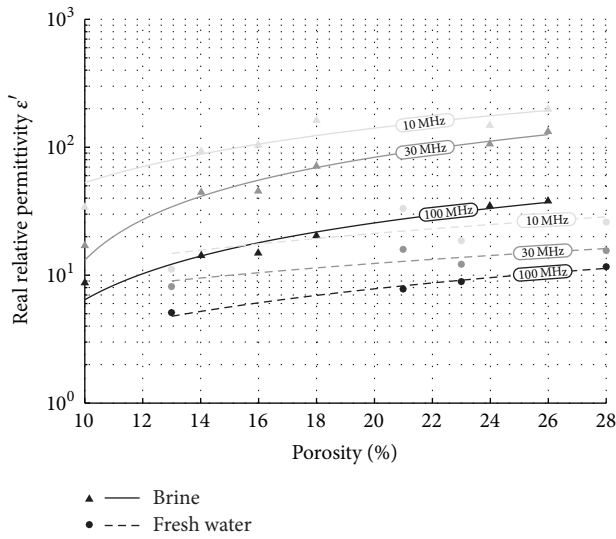


FIGURE 6: Dielectric response of brine saturated and fresh water samples at 100, 30, and 10 MHz.

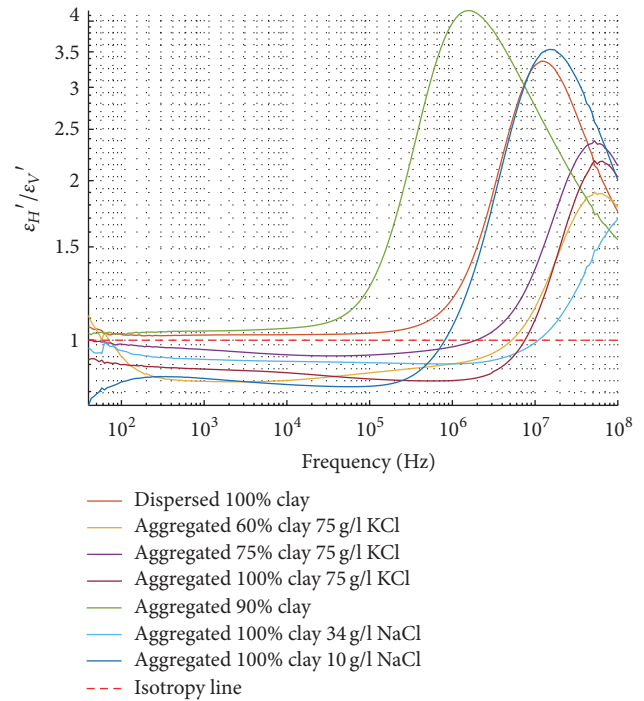


FIGURE 8: Dielectric anisotropy versus frequency in brine saturated and fresh water samples.

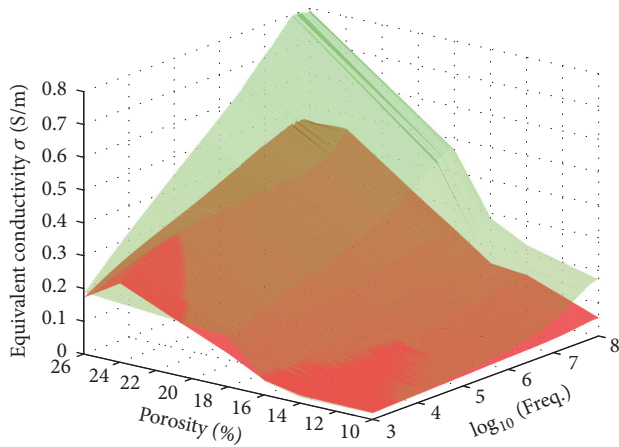


FIGURE 7: Surface plot of conductivity, measured parallel (in green) and normal (in red) to the bedding, versus porosity and frequency in 6 brine saturated artificial shale samples.

same frequency of ~60 MHz corresponding to the samples saturated with KCl brine. The lowest peak belonging to the sample saturated with NaCl brine occurs at frequencies above 100 MHz. The crossover points with isotropy line in brine saturated samples are also distributed across the

megahertz frequency, similarly to the peak values, but at lower frequencies.

This anisotropic behaviour may be explained with electric double layer theory. Given that the clay particles in fresh water samples have thick hydrate envelopes of weakly bound water, the dipole polarization of water molecules is achieved more easily in the parallel to bedding plane simply due to the fact that the clay particles in all the samples are mostly oriented in horizontal direction. Hence water molecules are oriented with their hydrogen atoms towards the surfaces of clay particles and are easily skewed sideways under the influence of electric field parallel to the bedding but resist the influence of normal electric field. In the brine saturated samples this effect is less pronounced across the wide frequency range due to the significantly thinner diffuse part of the double electric layers where the above phenomenon occurs. Therefore, considering the distinctive features of dielectric anisotropy in artificial samples, one might infer that the anisotropy analysis can help with understanding of composition and concentration of the saturating fluids in clay

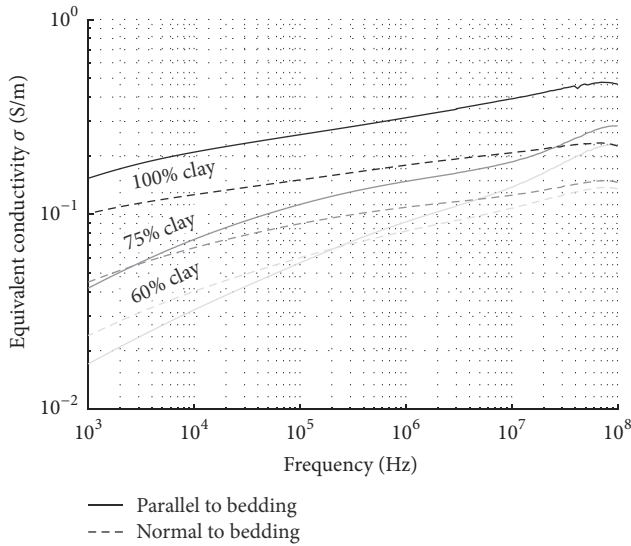


FIGURE 9: Effect of clay content on frequency dependent conductivity in samples measured parallel and normal to the bedding plane.

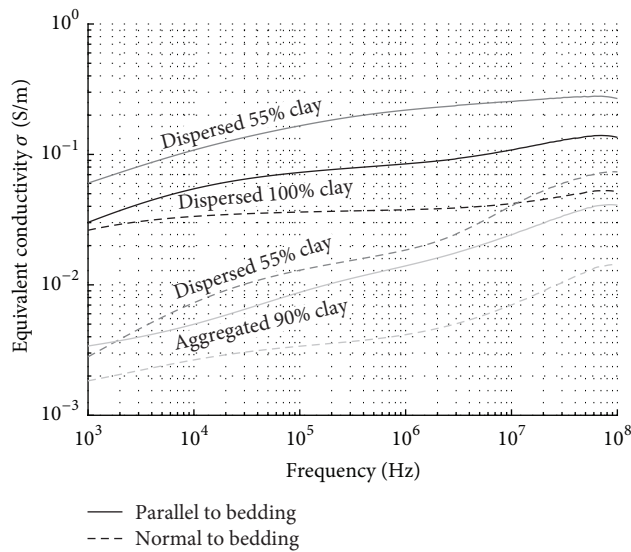


FIGURE 10: Effect of microstructure on conductivity of artificial shales measured parallel and normal to the bedding plane.

rocks. However, more data on artificial and natural rocks need to be analysed to confirm the discussed relationships.

Figure 9 shows that the increase of clay content at the same porosity results in greater conductivity in both vertical and horizontal directions. This behaviour is caused by the surface conduction mechanisms characteristic to clay particles. It has been shown that the counter ions located in the Stern layer of clay particles are the dominant contributors to surface conduction and in brine saturated rocks with salinity above 1 mol/l the mobility of K and Na ions develops 1/10 of that in the free fluid and is independent from the salinity [23]. Therefore, in our experiments replacing the fraction of quartz

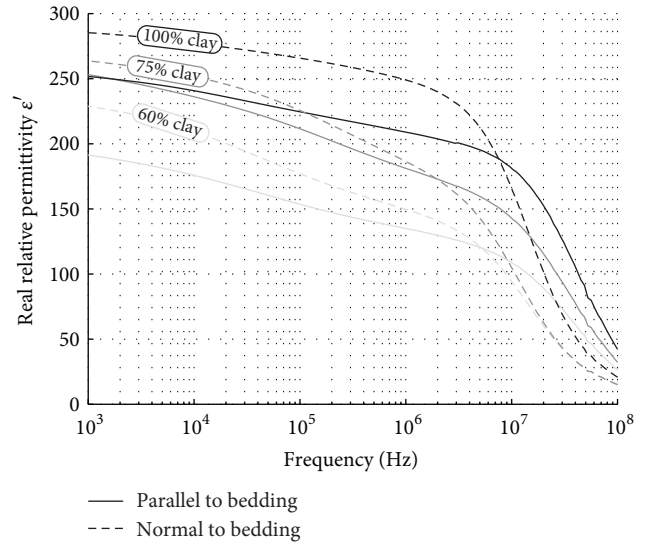


FIGURE 11: Dielectric response of the three brine-saturated artificial shale samples with clay contents of 60, 75, and 100 per cent.

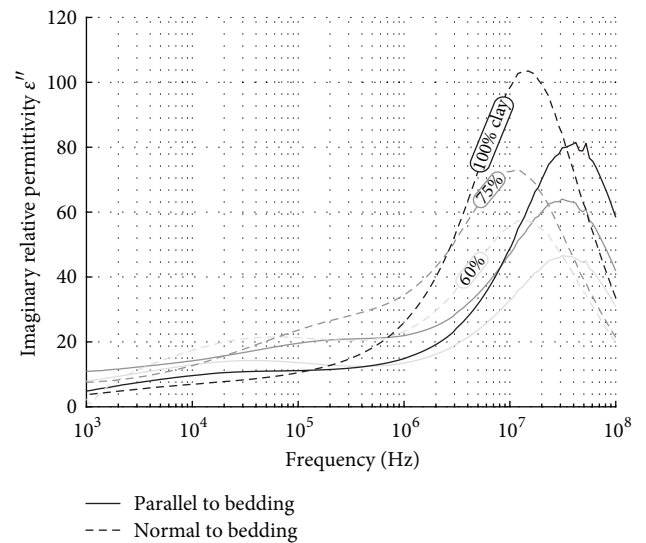


FIGURE 12: Frequency dependent dielectric loss in artificial shales with varying clay content.

with clay particles having much more uncompensated charge results in proportionally stronger surface conduction.

Figure 10 shows that the conductivity of the samples prepared with dispersed clay microstructure is always higher than that of the aggregated sample in both directions independently of the silt content and porosity. This is due to the greater surface conduction in the Stern layer of the dispersed samples where the clay particles are separated from each other and have greater free surface than their associations in aggregated sample.

At frequencies in the range of 1 kHz to 100 MHz the vertical polarization dominates in the brine saturated samples as shown in Figure 11. The main polarization mechanism in

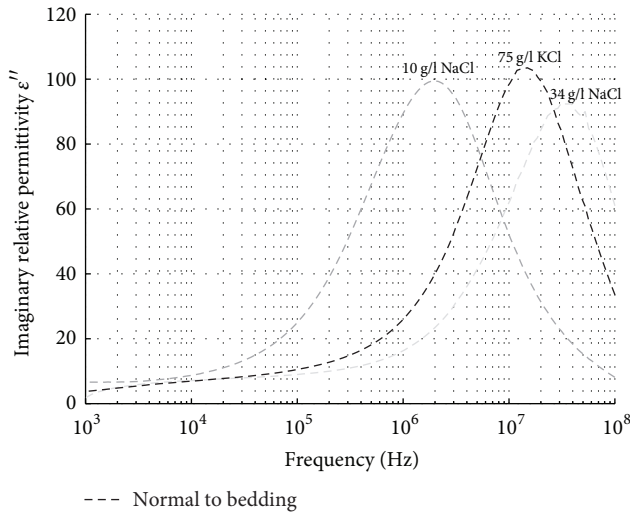


FIGURE 13: Frequency dependent dielectric loss in brine saturated artificial shales.

this frequency band is the Maxwell-Wagner polarization of counter ions. The movement of ions in the vertical direction is restricted due to the strong orientation of clay particles normal to the applied electric field and the force balance within their electric double layers. In this case each individual clay particle acts as a capacitor and the ensemble of such particles gives rise to strong polarization effects exceeding that of the individual fluid and mineral phases [3]. In contrast, the cations can be easily drawn along the surface of clay platelets and through the less tortuous pore network along the bedding. Thus, in the presence of a low frequency electric field (below megahertz) in the direction normal to the bedding hydrated counter ions are prone to polarization rather than to conduction and vice versa for the electric field in the bedding direction. Also, it is important to note that the higher the clay content is the more the polarization effects are pronounced in both directions due to the higher concentration and the better alignment of clay platelets given the same porosity level [16].

Figure 11 shows the rollover of real relative permittivity in the MHz range of frequencies for both the vertical and horizontal measurements. According to Kramers–Krönig relationship [24] these rollovers correspond to the peaks on the plots of imaginary relative permittivity in Figure 12. Peak values of dielectric loss-factor in vertical direction appear at approximately one order of magnitude lower frequencies and are ~20% higher than those measured in horizontal direction. One must take these effects into account designing the borehole heating antennas for effective hydrocarbon extraction in unconventional reservoirs. Also, samples with higher clay content show the higher values of loss-factor due to the sharper rollover in the real relative permittivity caused by the change in polarization mechanism from surface-charge to dipole polarization with increase of frequency.

Figure 13 illustrates the dielectric loss-factor for the three samples saturated with different brine cation composition and concentration. All the peaks are located at MHz range for the measured samples. Distribution of the peaks at different

frequencies depends on the salinity of a pore fluid and its cation composition. Hence, increasing the salinity from 10 to 34 g/l in pure kaolinite sample saturated with NaCl results in change of peak frequency from 2×10^6 to 3×10^7 Hz. Sample saturated with 75 g/l NaCl solution exhibits the peak frequency of 4×10^7 which highlights the effect of different salt ions on the dielectric loss-factor of clay rocks.

4. Conclusions

Artificial shales with simple mineral composition illustrate the broad frequency dispersion of dielectric effects. The variations in salinity of the connate water, its cation composition, clay content, and microstructure of artificial shales significantly affect complex dielectric permittivity and conductivity of artificial shales. These effects can be explained with the Maxwell-Wagner polarization effects at frequencies below megahertz range and the changes occurring in double electric layer of clay particles in the presence of electrolyte at higher frequencies.

It is shown that at high frequencies (above 10 MHz) real relative permittivity has different linear trends with porosity in fresh water and brine saturated samples. The salinity and cation composition of the pore fluid seem to have negligible effect on these high frequency dielectric trends.

Formation of anisotropic microstructure of artificial shales during mechanical compaction results in significant values of dielectric anisotropy between 2 and 4. The magnitude and characteristic frequency of the peak values in anisotropy curves as well as the crossover with isotropy point is dependent on salinity, cation composition of saturating fluid, and the clay content of the samples.

The absolute peak value of dielectric loss in shales and its characteristic frequency depends not only on the amount of connate fluid, but also on the cation composition of the saturating brine, its salinity, and the orientation of an applied electric field relative to the shale bedding. The peak values of the dielectric loss measured along and normal to bedding lay within the megahertz frequency range with significant separation of approximately 1 order of magnitude. The absolute values of these peaks are approximately 20 percent higher in the direction normal to the bedding.

Our simplistic models of natural shales illustrated the complex dielectric behaviour similar to that of the real rocks. The theoretical modelling of dielectric response is conducted in companion paper illustrating the use of artificial shales for design and calibration of the rock physics models.

Conflicts of Interest

The authors declare that they have no conflicts of interest.

Acknowledgments

The authors would like to thank the CSIRO Shale Rock Physics and Petrophysics (SHARPP) consortium sponsored by Total for financial support of this work. R. Beloborodov would like to acknowledge ASEG Research Foundation for sponsoring him with Grant RF16P05.

References

- [1] A. R. von Hippel, *Dielectrics and Waves*, Wiley, New York, NY, USA; Chapman & Hall, London, UK, 1954.
- [2] P. N. Sen, “Relation of certain geometrical features to the dielectric anomaly of rocks,” *Geophysics*, vol. 46, no. 12, pp. 1714–1720, 1981.
- [3] P. N. Sen and W. C. Chew, “The frequency dependent dielectric and conductivity response of sedimentary rocks,” *The Journal of Microwave Power and Electromagnetic Energy*, vol. 18, no. 1, pp. 95–105, 1983.
- [4] D. Freed, N. Seleznev, C.-Y. Hou et al., “A physics-based model for the dielectric response of shaly sands,” in *Proceedings of the 57th Annual Logging Symposium (SPWLA '16)*, Society of Petrophysicists and Well-Log Analysts, Reykjavik, Iceland, June 2016.
- [5] M. Hizem, H. Budan, B. Devillé, O. Faivre, L. Mossé, and M. Simon, “Dielectric dispersion: a new wireline petrophysical measurement,” in *Proceedings of the SPE Annual Technical Conference and Exhibition (ATCE '08)*, pp. 3230–3250, Society of Petroleum Engineers, Denver, Colo, USA, September 2008.
- [6] M. Josh, M. B. Clennell, M. D. Raven, and D. N. Dewhurst, “Factors controlling dielectric response of clays and shales,” in *Proceedings of the 2015 SEG Annual Meeting*, Society of Exploration Geophysicists, New Orleans, Louisiana, October 2015.
- [7] A. A. Garrouch and M. M. Sharma, “Influence of clay content, salinity, stress, and wettability on the dielectric properties of brine-saturated rocks: 10 Hz to 10 MHz,” *Geophysics*, vol. 59, no. 6, pp. 909–917, 1994.
- [8] P. N. Sen, “The dielectric and conductivity response of sedimentary rocks,” in *Proceedings of the SPE Annual Technical Conference and Exhibition*, Society of Petroleum Engineers, Dallas, Tex, USA, September 1980.
- [9] A. Mukhametshina and E. Martynova, “Electromagnetic heating of heavy oil and bitumen: a review of experimental studies and field applications,” *Journal of Petroleum Engineering*, vol. 2013, Article ID 476519, 7 pages, 2013.
- [10] T. Abraham, C. W. Van Neste, A. Afacan, and T. Thundat, “Dielectric relaxation-based capacitive heating of oil sands,” *ENERGY & FUELS*, vol. 30, no. 3, pp. 1987–1996, 2016.
- [11] M. Josh, “Dielectric permittivity: a petrophysical parameter for shales,” *Petrophysics*, vol. 55, pp. 319–332, 2014.
- [12] J. G. Berryman and G. M. Hoversten, “Modelling electrical conductivity for earth media with macroscopic fluid-filled fractures,” *Geophysical Prospecting*, vol. 61, no. 2, pp. 471–493, 2013.
- [13] M. Al-Harashsheh, S. Kingman, A. Saeid, J. Robinson, G. Dimitrakakis, and H. Alnawafleh, “Dielectric properties of Jordanian oil shales,” *Fuel Processing Technology*, vol. 90, no. 10, pp. 1259–1264, 2009.
- [14] J.-M. Donadille, “On the petrophysical analysis of dielectric anisotropy,” in *Proceedings of the 57th Annual Logging Symposium (SPWLA '16)*, Society of Petrophysicists and Well-Log Analysts, Reykjavik, Iceland, June 2016.
- [15] M. Josh, B. Clennell, and M. Cauchefert, “Dielectric permittivity and anisotropy of intact multi-saturated organic shales,” in *Proceedings of the 57th Annual Logging Symposium (SPWLA '16)*, Society of Petrophysicists and Well-Log Analysts, Reykjavik, Iceland, June 2016.
- [16] R. Beloborodov, M. Pervukhina, V. Luzin et al., “Compaction of quartz-kaolinite mixtures: the influence of the pore fluid composition on the development of their microstructure and elastic anisotropy,” *Marine and Petroleum Geology*, vol. 78, pp. 426–438, 2016.
- [17] X. Dong and Y.-H. Wang, “The effects of the pH-influenced structure on the dielectric properties of kaolinite-water mixtures,” *Soil Science Society of America Journal*, vol. 72, no. 6, pp. 1532–1541, 2008.
- [18] M. Josh, “A combination dielectric and acoustic laboratory instrument for petrophysics,” *Measurement Science and Technology*, vol. 28, no. 12, Article ID 125904, 2017.
- [19] V. I. Osipov, V. N. Sokolov, and V. V. Eremeev, *Clay Seals of Oil and Gas Deposits*, A. A. Balkema Publishers, Lisse, the Netherlands, 2004.
- [20] K. Bohinc, V. Kralj-Iglič, and A. Iglič, “Thickness of electrical double layer. Effect of ion size,” *Electrochimica Acta*, vol. 46, no. 19, pp. 3033–3040, 2001.
- [21] M. A. Brown, A. Goel, and Z. Abbas, “Effect of electrolyte concentration on the stern layer thickness at a charged interface,” *Angewandte Chemie International Edition*, vol. 55, no. 11, pp. 3790–3794, 2016.
- [22] R. Beloborodov, M. Pervukhina, L. Esteban, and M. Lebedev, “Compaction of quartz-kaolinite powders with aggregated initial microstructure—elastic properties and anisotropy,” in *Proceedings of the 77th EAGE Conference and Exhibition 2015—Earth Science for Energy and Environment*, Madrid, Spain, June 2015.
- [23] A. Revil and P. W. J. Glover, “Nature of surface electrical conductivity in natural sands, sandstones, and clays,” *Geophysical Research Letters*, vol. 25, no. 5, pp. 691–694, 1998.
- [24] F. Kremer and A. Schönhal, *Broadband Dielectric Spectroscopy*, Springer, Berlin, Germany, 2002.

Research Article

Impact of Petrophysical Properties on Hydraulic Fracturing and Development in Tight Volcanic Gas Reservoirs

Yinghao Shen,^{1,2} Mianmo Meng,¹ Tao Liu,³ Hongkui Ge,^{1,4} and Yuelel Zhang⁵

¹Unconventional Natural Gas Institute, China University of Petroleum-Beijing, Beijing, China

²Texas Tech University, Lubbock, TX, USA

³Oil & Gas Technology Research Institute, Changqing Oilfield Company, Xi'an, China

⁴China University of Petroleum-Beijing at Karamay, Xinjiang, China

⁵CNODC Brasil Petroleo E Gas Ltda, Rio de Janeiro, RJ, Brazil

Correspondence should be addressed to Yinghao Shen; shenyinhao@126.com and Mianmo Meng; mmmcup@163.com

Received 29 July 2017; Accepted 12 November 2017; Published 13 December 2017

Academic Editor: Ebrahim Fathi

Copyright © 2017 Yinghao Shen et al. This is an open access article distributed under the Creative Commons Attribution License, which permits unrestricted use, distribution, and reproduction in any medium, provided the original work is properly cited.

The volcanic reservoir is an important kind of unconventional reservoir. The aqueous phase trapping (APT) appears because of fracturing fluids filtration. However, APT can be autoremoved for some wells after certain shut-in time. But there is significant distinction for different reservoirs. Experiments were performed to study the petrophysical properties of a volcanic reservoir and the spontaneous imbibition is monitored by nuclear magnetic resonance (NMR) and pulse-decay permeability. Results showed that natural cracks appear in the samples as well as high irreducible water saturation. There is a quick decrease of rock permeability once the rock contacts water. The pores filled during spontaneous imbibition are mainly the nanopores from NMR spectra. Full understanding of the mineralogical effect and sample heterogeneity benefits the selection of segments to fracturing. The fast flow-back scheme is applicable in this reservoir to minimize the damage. Because lots of water imbibed into the nanopores, the main flow channels become larger, which are beneficial to the permeability recovery after flow-back of hydraulic fracturing. This is helpful in understanding the APT autoremoval after certain shut-in time. Also, Keeping the appropriate production differential pressure is very important in achieving the long term efficient development of volcanic gas reservoirs.

1. Introduction

Compared to the development of tight sand reservoirs, there is less research focused on the development of volcanic reservoirs. A volcanic reservoir is a type of low porosity and low permeability reservoir. At the same time, anisotropy is a typical characteristic of volcanic formation due to its complex diagenetic environment [1–3]. Thus, developing this type of reservoir is very challenging. Using a horizontal well with multistage hydraulic fracturing is an important technique for developing volcanic reservoirs. However, for prolific formations, lots of fracturing fluid is retained in the formation after flow-back. Thus, the permeability decreases, and aqueous phase trapping (APT) appears. APT occurs after drilling, hydraulic fracturing, and workover. APT is caused by fluid filtrating into the formation to reduce the formation permeability [4–6]. However, after the well has been shut-in for

some time, the permeability of volcanic reservoirs increases and the APT can be autoremoved to some extent, similar to gas shale [7, 8]. The combination of applying multilateral horizontal drilling and multistage hydraulic fracturing has successfully unlocked unconventionally tight hydrocarbon reservoirs. However, field data show that only a fraction of the large water volume used in hydraulic fracturing treatments is recovered during the flow-back operation. The spontaneous imbibition properties of tight sand and shale reservoirs have been investigated by many experts [9–14]. However, there is less research related to volcanic reservoirs.

Tight gas reservoirs have strong properties of stress sensitivity, which tremendously reduce production in quick-releasing pressure environments. Lowering the pore pressure as gas is produced increases the confining stresses on the reservoir rock, causing it to compact. This compaction causes a reduction in the effective pore diameter, resulting in a

TABLE 1: Dimensions, porosity, and permeability of various samples.

Sample	Diameter (mm)	Length (mm)	Porosity (%)	Dry samples pulse-decay permeability (mD)
L1	24.88	11.35	7.77	0.0078
L2	24.96	20.46	6.85	0.0018
L3	24.91	10.93	16.07	0.036
L4	24.88	10.05	16.12	0.0078
L5	24.84	25.69	16.41	0.010
L6	24.84	12.49	7.07	0.00056
L7	24.73	13.60	6.60	0.00049
L8	24.85	19.89	4.23	0.00083
L9	24.86	50.61	6.88	0.00041
L10	24.88	53.24	7.00	0.00027
L11	24.88	51.34	2.92	0.00019
L12	24.93	50.01	1.60	0.00038
L13	24.77	50.79	4.24	0.00013
L14	25.35	50.69	2.01	0.0020
L15	24.78	50.36	2.00	0.00015
L16	24.94	50.87	1.25	0.00067

decreased permeability. This effect has been studied by several authors [15–21]. In recent years, low-field nuclear magnetic resonance (NMR) has become a quick, lossless, and effective means of quantitative microstructural characterization of rock formations, and it has been widely used in fine reservoir descriptions of clastic rocks, carbonate, coal, and other conventional reservoirs in the laboratory and well logging. Thus, the nuclear magnetic resonance technique has become a useful tool to research varieties of rock types [22–27]. To obtain a high production of volcanic reservoirs, additional research on these formations should be carried out. This paper focuses on investigating some petrophysical properties of volcanic rocks in Songliao Basin, China, to provide some reservoir information for the efficient development.

The study area is located in Yingtai of Jilin, China. The volcanic rock in this region is extremely heterogeneous with low porosity and low permeability. The multistage horizontal well with hydraulic fracturing procedure is a necessary technique to develop the resources in this location.

This paper contributes to the understanding of APT autoremoval of the prolific volcanic reservoirs and is beneficial for determining the optimal production differential pressure for efficiently developing this type of reservoir.

2. Samples

The physical parameters of some samples are listed in Table 1. Volcanic rock samples are mainly taken from the Lower Cretaceous Yingcheng Formation in Yingtai of Jilin, China. The samples were dried at 65°C before the experiment, until the mass became constant. Sample porosities were measured with a helium porosimeter (KXD-III type). The sample pulse-decay permeability was determined by an ultra-low permeability measurement instrument (YRD-CP200 type).

Confining pressure was exerted by water, while pore pressure was exerted by helium. The test temperature was 25°C. The porosity and permeability of the volcanic rocks fluctuated greatly. Some samples have similar porosity, but their permeability differs tremendously. This characteristic may account for the heterogeneity of the volcanic reservoir complex. The samples of L1 and L2 were selected for the spontaneous imbibition test, monitored by nuclear magnetic resonance equipment. The main magnetic field had a frequency of 23 MHz, the signal superposition time was 64, the waiting time was 3000 ms, and the echo spacing was 0.116 ms. Samples L3–L8 were selected for one surface spontaneous imbibition test, monitored by a pulse-decay permeability apparatus under a confining pressure of 8 MPa and pore pressure of 5 MPa. Samples L9–L16 were selected for a stress sensitivity experiment under a confining pressure of 10–30 MPa and pore pressure of 6 MPa. All these experiments occurred at atmospheric conditions except for the special illustration.

3. Experimental Methods

Bulk mineralogical compositions were derived from XRD (X-ray diffraction) patterns, which were measured by a D/max 2500 diffractometer. This experiment was carried out at the State Key Laboratory of Petroleum Resources and Prospecting, in China University of Petroleum, Beijing.

Standard thin section preparation and analysis were carried out here to investigate the regular micropore structure and mineral distribution. In this experiment, the blue epoxy was injected into the rock pores under vacuum. Thin sections were obtained by polishing the bulk rock after the liquid glue was solidified. Due to the pores in the rock being occupied by color glue, the pores and cracks could be distinguished clearly by a microscope. This experiment was also carried out at the State Key Laboratory of Petroleum Resources and

Prospecting in China University of Petroleum, Beijing, using a LEICA DFC550 made in Germany.

Centrifuge analyses were conducted by a centrifuge machine with an arm radius of 17 cm. The samples were dried until the mass became constant. Subsequently, the samples were saturated with liquid after they were vacuumed and centrifuged again. The liquids used here were distilled water and anion water and the anion water consisted of sodium dodecyl sulfate (SDS) and distilled water. This experiment was performed at the Education Ministry Key Laboratory of Petroleum Engineering in China University of Petroleum, Beijing.

A nuclear magnetic resonance (NMR) experiment was performed while spontaneous imbibition was carried out using the MicroMR23-025V equipment in Shanghai Niumag Corporation. The principle of NMR is based on the difference in the transverse relaxation times of liquids with different pore sizes—the larger the pores, the longer the transverse relaxation time. The main magnetic field had a frequency of 23 MHz, the signal superposition time was 64 ms, the wait time was 3000 ms, and the echo spacing was 0.116 ms. The steps of testing are listed as follows. (1) The dry sample was measured by NMR and analytic balance. (2) The sample was soaked into the liquid for a period of time, 150 min for L1 and 120 min for L2, respectively. Then, it was taken out and dried with adsorbent paper, and the oncoming test time interval is about 30 min for both of them. (3) The wet sample was measured by NMR and analytic balance. (4) Steps (2) and (3) were repeated. After the experiment, the spectra as well as the liquid content as a function of imbibition time were obtained.

A pulse-decay permeability experiment in the process of spontaneous imbibition was conducted by the pulse-decay permeability measurement instrument (YRD-CP200 type) at the State Key Laboratory of Petroleum Resources and Prospecting in China University of Petroleum, Beijing. The measurement principle is based on the pressure-decay between the two ends of samples. The logarithm of deferential pressure is a linear function of time. Sample permeability is closely related to the linear slope. The main equations are listed as follows, which is consistent with Cui et al. 2009 [28].

Dimensionless differential pressure Δp_D ,

$$\Delta p_D = \frac{p_u(t) - p_d(t)}{p_u(0) - p_d(0)}. \quad (1)$$

At large experimental time, the Δp_D can be simplified [29, 30],

$$\ln(\Delta p_D) = \ln(f_0) + s_1 t. \quad (2)$$

f_0 is constant and s_1 is shown as

$$s_1 = \frac{k f_1 A (1/V_u - 1/V_d)}{\mu L c_g}, \quad (3)$$

where f_1 is

$$f_1 = \frac{\theta_1^2}{a} + b, \quad (4)$$

where a and b are

$$a = \frac{V_p (1 + f_a)}{V_u} \quad (5)$$

$$b = \frac{V_p (1 + f_a)}{V_d}.$$

θ_1 is the first root of the following equation:

$$\tan \theta = \frac{(a + b)\theta}{\theta^2 - ab}. \quad (6)$$

At last, the permeability can be expressed as

$$k = \frac{-s_1 \mu L c_g}{f_1 A (1/V_u + 1/V_d)}. \quad (7)$$

In this experiment, only one surface of the sample contacted the liquid to monitor the fracturing fluid filtrating into the formation through the surface of the hydraulic fractures. Our spontaneous imbibition testing was consistent with Ghanbari and Dehghanpour [31]. The detailed steps are listed as follows: (1) the permeability and weight of the sample were measured in dry state; (2) one surface of the sample contacted the liquid for a period of time, which is about 30~50 min in the work, and then it was taken out and dried with adsorbent paper; (3) the permeability and weight of the wet sample were measured; (4) steps (2) and (3) were repeated. After this experiment, the permeability change with imbibition time as well the liquid content as a function of imbibition time can be obtained.

A stress sensitivity experiment was performed by a pulse-decay permeability measurement instrument (YRD-CP200 type) at the State Key Laboratory of Petroleum Resources and Prospecting in China University of Petroleum, Beijing. In this experiment, the permeability was measured under different net confining pressure. In the experimental process, the sample was placed in the pulse-decay permeability equipment, until the entire stress sensitivity experiment was finished.

4. Results

4.1. Analysis of Mineral Components of Rock. Tight reservoirs usually have strong heterogeneity in mineral composition. The mineral composition may vary significantly through the rock column in the same formation [32–34].

The mineral contents of various volcanic rocks are listed in Table 2. The samples used for XRD tests were derived from fragments when cutting the standard samples. The quartz and total clays make up most of the content, but plagioclase and K-feldspars are also important constituents. The abundance of calcite, dolomite, and pyrite is nearly zero. Quartz is a mineral important in improving the efficiency of hydraulic fracturing [35]. Clays have a large effect on the adsorption of fracturing fluid in volcanic reservoirs [36].

The important mineralogy of volcanic rock with depth is presented in Figure 1. The samples were named according to their depth—the larger the sample number, the deeper the sample. The depth range is 3806.9 m~4101.2 m and sample

TABLE 2: Results of XRD mineralogy analyses.

Samples	L1	L2	L3	L4	L5	L6	L7	L8	L9	L10	L11	L12	L13	L14	L15	L16
Length	11.35	20.46	10.93	10.05	25.69	12.49	13.60	19.89	50.61	53.24	51.34	50.01	50.79	50.69	50.36	50.87
Type of analysis	Bulk & clay															
Weight%	100	100	100	100	100	100	100	100	100	100	100	100	100	100	100	100
Quartz	45.2	44	55.8	44.3	41.1	53.7	13.2	43.5	44.2	36.1	51.3	33.5	45.1	39.8	42.5	36.8
Potassium feldspar	4.9	4.7	3.9	1.9	6.4	2.3	1.9	3.1	1.2	1.3	3.4	1.4	2.8	3.3	1.8	16
Plagioclase feldspar	15.6	18.9	22.4	16.2	9.5	32.7	10	7.1	16	9	12.3	7.7	16.9	12.7	16.8	20.0
Calcite	0	0	3.7	0	0	1.4	0	0	0	0	0	0	0	0	0	1.6
Pyrite	0	1.2	0	0	0	0	0	0	0	0	0	0	0	0	0	0
Total clay	34.3	31.2	14.2	37.6	43	9.9	74.9	46.3	38.6	53.6	33	57.4	35.2	44.2	38.9	40.0

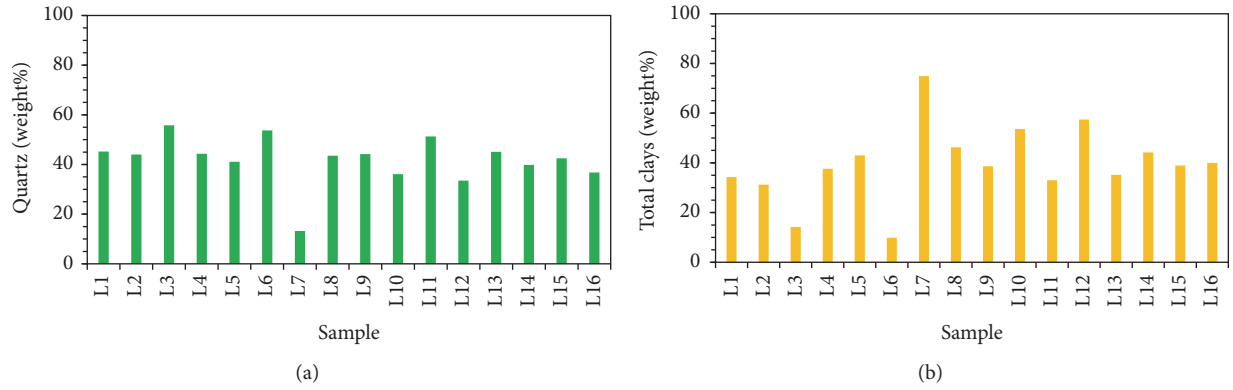


FIGURE 1: (a) Quartz on the left, (b) total clays on the right of various volcanic samples from various depths.

interval between two samples is about 12.5 m. As shown in Figure 1, the quartz content and clay content do not have clear tendency with depth. The minerals are usually used as an evaluation criterion for selecting the best segment for hydraulic fracturing. More brittle minerals, such as quartz, and less clays are usually better for hydraulic fracturing in unconventional reservoir [37], which is widely accepted as one important criterion. However, the trends with depth are not clear enough in the research area, which means that the segment choice of hydraulic fracturing needs more consideration by the mineral components evaluation. It is critical to get the whole formation mineral type and content to get the more favorable formation segment for developing fractures.

4.2. Casting Thin Sections. Three photomicrographs from thin section analysis of volcanic rock casts are shown in Figure 2. There are microfractures at different scales; the width of microfractures is 0.02~0.2 mm. The manufacturing operation of the thin sections follows the basic direction in the lab. The microfractures shown in Figure 2 are more likely the original microfractures of samples.

The potential influence of microfractures should be considered during hydraulic fracturing and gas production. Firstly, microfractures contribute to sample permeability stress sensitivity. The permeability is difficult to recover after confining pressure unloading while there are more microfractures. Thus, it needs further study on permeability

with effective pressure, which will be conducted later. Secondly, microfractures are beneficial to generation of hydraulic fracture network. At the same time, microfractures are important flow channels for gas production. If fractures connect to each other under the hydraulic pressure, formation permeability can be improved greatly.

4.3. Centrifuge Testing. Results of centrifuge testing on volcanic rock are presented in Figure 3. Samples with distilled water have a higher irreducible water saturation than samples with anion water, except for sample C. The average irreducible water saturation of samples with distilled water is 75.5%, while the average irreducible water saturation of samples with anion water is 62.6%. Experimentally, the reservoir damage caused by fracturing liquid filtration can be reduced by using the anion-water-based fluid.

4.4. Monitor Spontaneous Imbibition Using Nuclear Magnetic Resonance Technique. Nuclear magnetic resonance technique was used in the experiments to clearly distinguish the distribution of the imbibed liquid with the soaking time in volcanic rocks. X-ray CT imaging technique has been previously used to research the spontaneous imbibition of low permeability sandstones [38]. However, this method cannot distinguish the exact distribution of the imbibed liquid, that is, the liquid distribution in the different pore sizes. The NMR technique has been widely used in rock analysis [39, 40]. The NMR method involves the motion of protons (Hydrogen

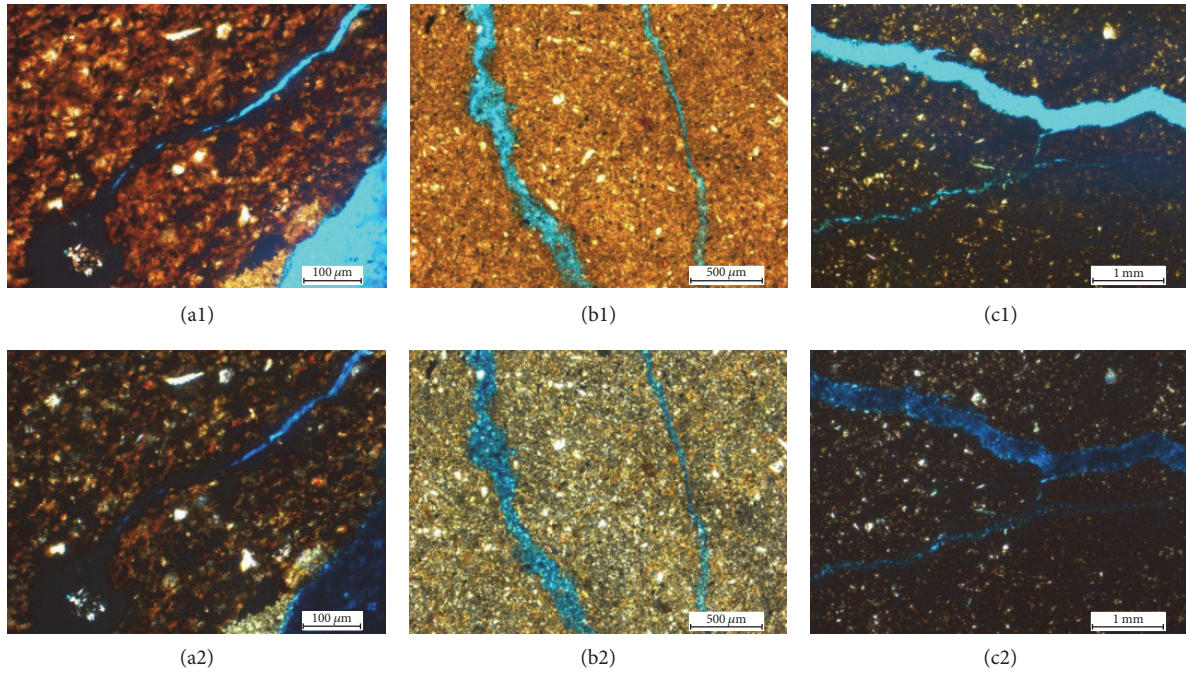


FIGURE 2: Casting film of three volcanic rock samples under plane polarized light (a1, b1, and c1) and perpendicular polarized light (a2, b2, and c2).

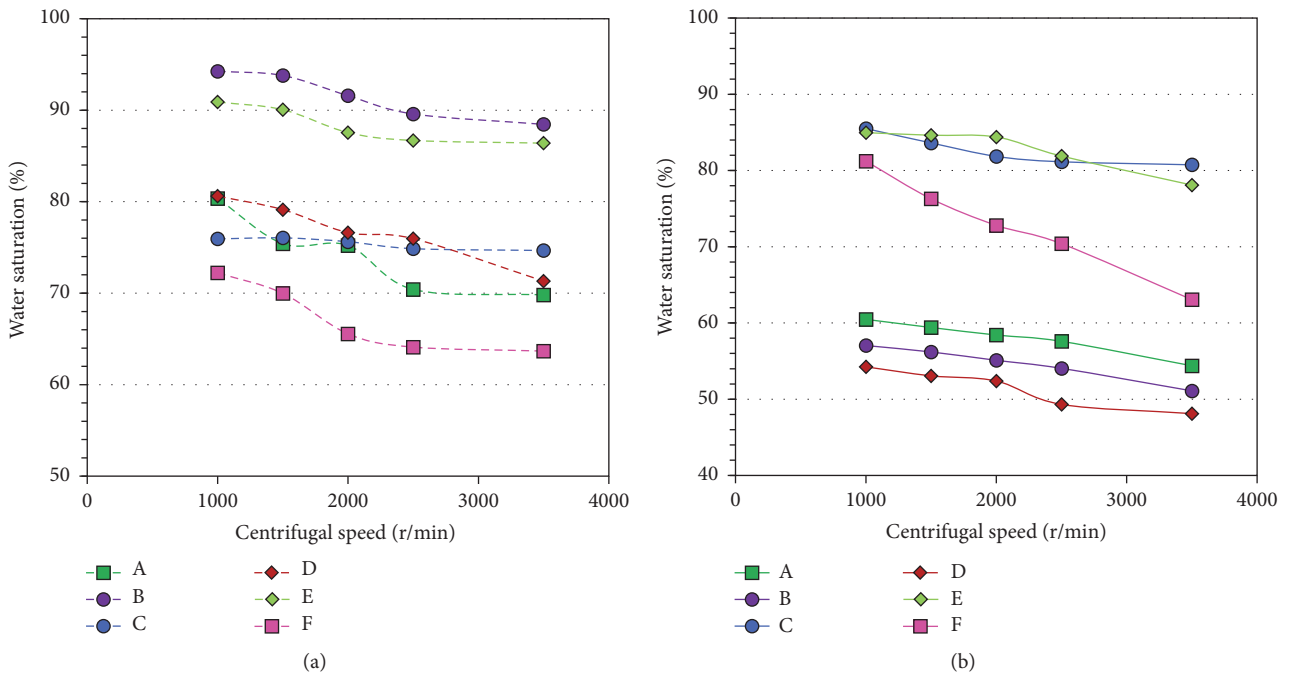


FIGURE 3: Centrifuge experiments for various volcanic samples: (a) distilled water and (b) anion water.

¹H) occurring in water and hydrocarbon fluids relative to the porous rock [41]. The fluid in large pores has a longer T2 value because more nuclei are available to exhibit the NMR effect, and the fluid in small pores has a short T2 value. The T2 relaxation time is inversely proportional to the specific surface of samples [42]. The T2 spectra as a function of spontaneous imbibition time is shown in Figure 4.

The sample L1 has three isolated peaks (left peak area \gg middle peak area \gg right peak area). Its T2 spectrum fluctuates to a certain degree according to the peak area change, where the area at 184 min is a little larger than that at 208 min. However, it is understandable because of the experiment error. The T2 spectrum area becomes stable in less than 151 min. Its right peak area is very small, which

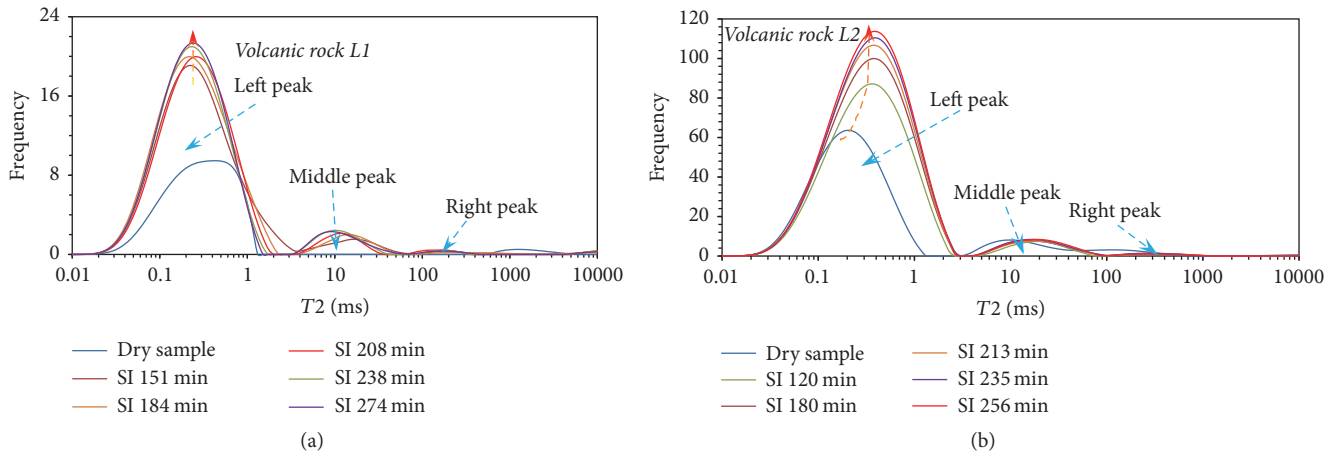


FIGURE 4: The T2 spectra of samples: L1 and L2 for various spontaneous imbibition times (SI is the acronym spontaneous imbibition).

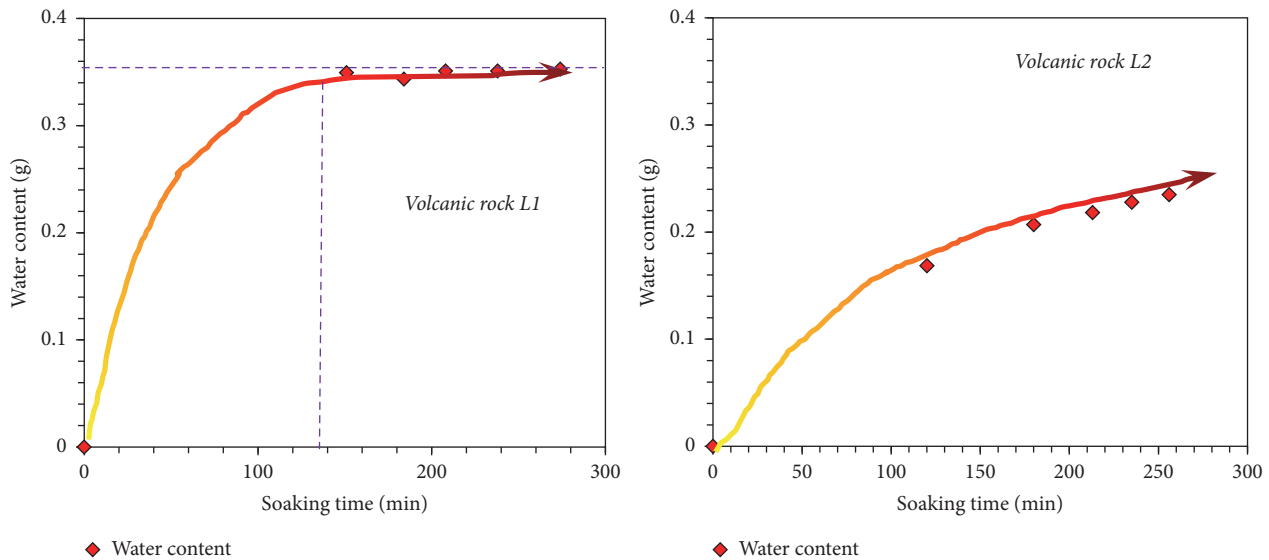


FIGURE 5: The water content as a function of soaking time: volcanic rocks L1 and L2. During imbibition the samples were soaked into the distilled liquid entirely. The trend curve represents the direction of water content change.

indicates that the number of large pores and fractures is small. The left peak area takes up the largest proportion, which shows that the micropores dominate the porosity of the main sample.

The sample L2 has three isolated peaks (left peak area \gg middle peak area \gg right peak area). Its right peak area is too small to be detected clearly. Its middle peak and right peak area become stable very quickly, but its left peak area increases gradually after the sample is soaked in water for 256 min, which indicates that its micropores have a slow imbibition rate. If the rate of fracturing fluid flow-back is fast, the reservoir will have less damage in this type of volcanic formation.

Figure 5 shows the water content of samples L1 and L2 as a function of spontaneous imbibition time. The sample weight is determined by analytic balance. As the sample is soaked in water, the water content of volcanic rock L1 becomes stable

by 120 min. However, the water content of volcanic rock L2 is still increasing by the same elapsed time. This phenomenon indicates that volcanic rocks have strong heterogeneity.

4.5. Monitor Spontaneous Imbibition Using Pulse-Decay Permeability Technique. The experiments concerning spontaneous imbibition have been performed with many types of rocks, especially sandstones and shales [43–47]. These studies have paid much attention to the damage caused by fracturing fluid filtration under the effect of spontaneous imbibition. At the same time, many types of additives have been added to the fracturing fluid to reduce the filtration rate and protect the target formation. Through reducing the fracturing fluid filtration, the formation permeability can be maintained. However, less research has focused on volcanic rocks. In this section, we used the pulse-decay permeability technique to monitor the rock permeability change with imbibition time.

TABLE 3: The permeability loss after rock imbibition.

Samples	Initial permeability [mD]	Final permeability [mD]	Permeability loss [%]
L3	0.0355	0.00418	88.2
L4	0.00773	0.000175	97.7
L5	0.01	0.00027	97.3
L6	0.000556	0.0000888	84.0
L7	0.000486	0.0000674	86.1
L8	0.000828	0.000306	63.0

The rocks contacted the liquid at only one surface to simulate the fracturing fluid filtrating into the formation from the fracture surface.

The volcanic rock permeability as well as the water content is shown in Figure 6 as a function of spontaneous imbibition time. The test condition is as follows: one surface of the sample contacts the distilled water to simulate the fracturing fluid filtrating into the formation through the fracture surface. The figure indicates that the permeability decreases quickly in the early period. The permeability of sample L3 reaches stability after the sample has been soaked for 100 min. At the same time, its water content approaches stability. However, the other five samples have different characteristics. Their water content continues to increase significantly while their permeability becomes stable. Thus, the water imbibed into the volcanic rock in the late period has little influence on the sample permeability based on L4 to L8; here the permeability change is the phenomenon of macro, where it is hard to distinguish the clay effect. However, in the micro scope the water is continually imbibed into micropores, which may be controlled by clay minerals and nanopores in the matrix. The fluids enters into the micropores by clay adsorption and capillary pressure. So the phenomenon that permeability does not change too much in the later period may occur because the fluid enters into the micropores, which have less contribution to the rock permeability than the main flowing channel.

The permeability change may have important influences to the flow-back scheme selection. The normal flow-back scheme includes fast flow-back, normal flow-back, and soaking back after fracturing. The basic consideration of the flow-back scheme is the balance between fracture propping and water invasion. The fast flow-back can be used to minimize the water invasion and permeability loss. According to Figure 6, the permeability of the six samples decreases significantly, which is about 80%~90% of original permeability and reaches stability very quickly, where the stable times range from 20 min to 150 min. Therefore, the quick flow-back of fracturing fluid is a better choice to improve the effect of hydraulic fracturing which is beneficial for minimizing the permeability loss by water invasion. The less the fracturing fluid retained in the reservoir, the higher the permeability that can be obtained.

APT autoremoval is based on the liquid migration among different pores after flow-back. In Figure 6, in the late imbibition period, it can be found that permeability keeps constant when imbibition mass still increases. It means that imbibition liquid at later period has no influence on rock

permeability. In reservoir condition, after flow-back, liquid can move in some pores which have no contribution to reservoir permeability. Therefore, the gas flowing channels increase. Leak-off can also damage the reservoir permeability. However, after flow-back, when these leak-off liquids filtrate into some pores, which have no influence on reservoir permeability, the damage will decrease.

In addition, we illustrated the permeability loss after rock imbibition which is shown in Table 3. The permeability loss is calculated as follows: $(\text{initial permeability} - \text{final permeability}) / \text{initial permeability}$, where the initial permeability refers to the dry sample permeability and the final permeability refers to the final time permeability during imbibition. From the table, we find that the permeability loss is very significant after imbibition. The permeability loss can be as high as 97.7% during the spontaneous imbibition process. Therefore, abundant fracturing liquid continuously imbibed into the formation damages the formation permeability. Because the water imbibed into formation increases with time, there will be more serious permeability loss; as is shown in Table 3 the permeability loss is in the range of 63%~97%. Combining the analysis, we concluded that a fast flow-back scheme after hydraulic fracturing is necessary, because the fast flow-back technique can decrease the interaction time between water and formation, and hence the water imbibed into formation.

4.6. Permeability Stress Sensitivity. The pulse-decay permeability measurement method has been widely recognized as a way to identify the ultra-low permeability rocks [28, 30, 48–53]. Because the conventional permeability measurement is based on recording the flow rate during the experiment, the flow rate through the ultra-low permeability rock is too small to be measured exactly under the precision of present equipment. The pulse-decay permeability measurement is based on the change in differential pressure with testing time. It can satisfy the requirements of the ultra-low permeability measurement well. Permeability stress sensitivity has been performed on various rocks, especially the sandstones and shales [54–56]. Pressure drawdown can produce stress sensitivity [57]. Sandstone has less stress sensitivity than shale, which will vary by two to three orders of magnitude when the confining pressure is changed from 3 MPa to 120 MPa and then returned to 3 MPa [58]. In this section, we studied the permeability stress sensitivity of volcanic rocks in detail and propose two formulas.

Results of the sample stress sensitivity are presented in Figure 7. The negative natural logarithmic permeability as a function of net confining pressure is shown in the y -axis.

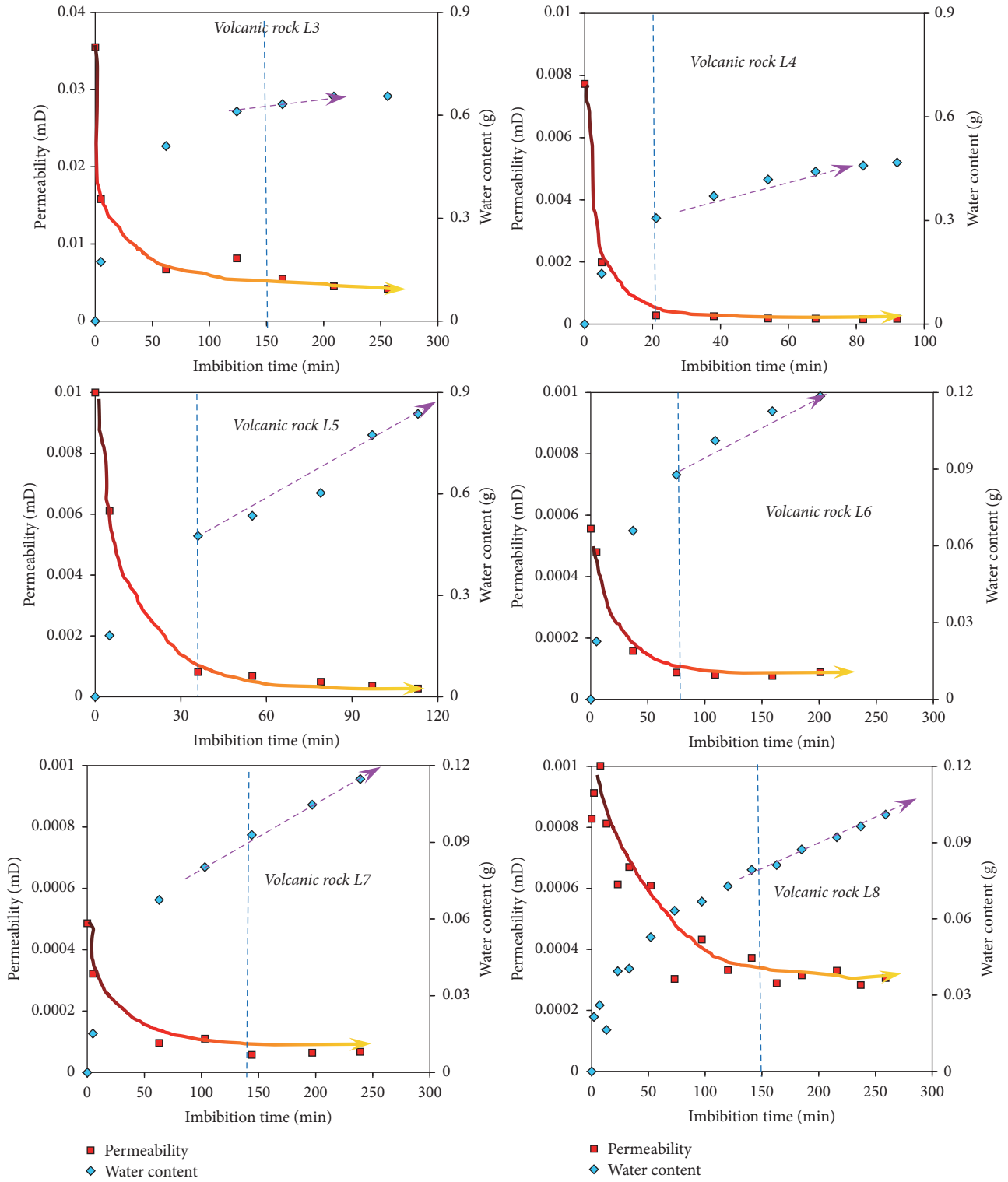


FIGURE 6: Permeability and water content as a function of imbibition time: volcanic rocks L3–L8. The rocks imbibition occurred with only one surface contacting the distilled liquid. The permeability refers to the pulse-decay permeability. The red trend line represents the direction of the permeability change.

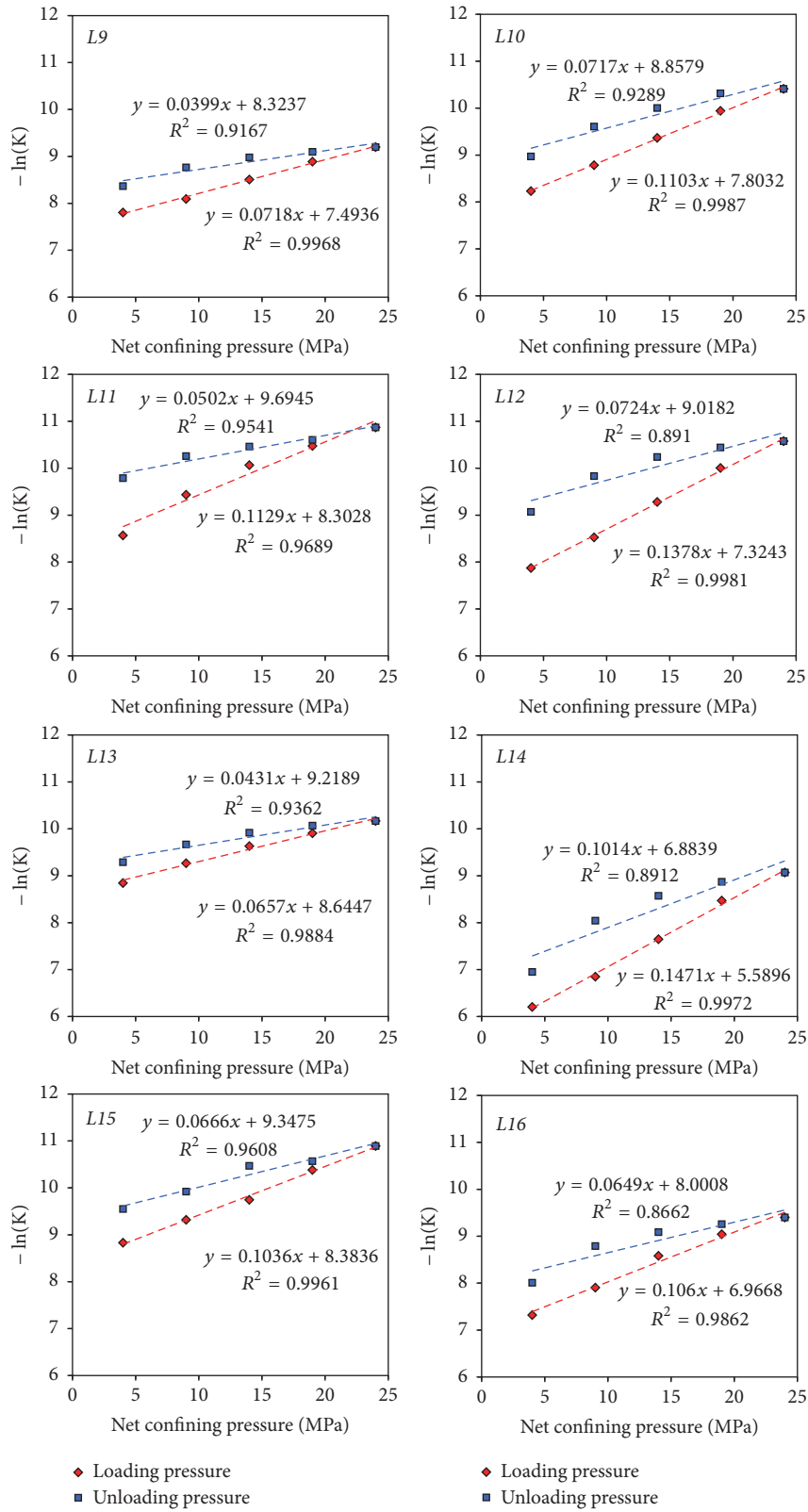


FIGURE 7: Negative log pulse-decay permeability as a function of net confining pressure: volcanic rocks L10–L16 for loading pressure and unloading pressure.

TABLE 4: The permeability change after the samples go through the process of loading pressure and unloading pressure.

Samples	K_0 (mD)	K_{01} (mD)	Loss ratio of permeability R_L (%)
L9	0.000408	0.000232	43.14
L10	0.000266	0.000127	52.26
L11	0.00019	0.000056	70.53
L12	0.000381	0.000115	69.82
L13	0.000134	0.0000924	31.04
L14	0.00202	0.000957	52.62
L15	0.000146	0.0000712	51.23
L16	0.000662	0.000332	49.85

Correlation coefficients of $R^2 = 0.9689\text{--}0.9987$ are computed for the loading process in each sample. The unloading process has correlation coefficients of $R^2 = 0.8662\text{--}0.9608$ generally lower than those observed for the loading process.

A fitted relation is presented for the permeability stress sensitivity of the loading pressure tests:

$$K = K_0 e^{-0.1069P+0.3964}, \quad (8)$$

$$R^2 = 0.8383,$$

where K is the rock pulse-decay permeability at different net confining pressures, K_0 is the lower net confining pressure permeability, and P is the net confining pressure. We can apply (1) to forecast the permeability of volcanic rock with increasing confining pressure.

Similarly, a fitted relation for the unloading pressure tests can be determined by calculating the volcanic rock permeability:

$$K = K_m e^{-0.0638P+1.4056}, \quad (9)$$

$$R^2 = 0.7804,$$

where K_m is the permeability under the maximum confining pressure and the other parameters are the same as in (1). Equation (2) provides us with a power law function to forecast the permeability change by injecting energy to recover the formation fluid pressure.

Here we need to clarify a point that the fitted relation is proposed to understand the permeability stress sensitivity characteristic. The formulas could not be treated as law because there are different relations between different samples. These are more likely fitting relations that help us comprehend the characteristics observed in tested samples.

In Table 4, where K_0 is the permeability at a net confining pressure of 6 MPa in the loading pressure process and K_{01} is the permeability after the sample completes the process of unloading pressure and the net confining pressure reaches 6 MPa, R_L is the loss rate of permeability, which is defined as

$$R_L = \frac{K_0 - K_{01}}{K_0} \times 100\%. \quad (10)$$

From the table, the value of R_L ranges from 31.04% to 70.53%. The R_L average value is 52.56%. Judging from the average value, the volcanic rock has high permeability

stress sensitivity. Usually the production pressure difference is enlarged to get higher production rate when developing the low permeability formation, which means that the bottomhole pressure needs to be much smaller. However, the results here show that a high-pressure difference may result in serious permeability loss, harmful to gas production. So, in the process of developing the volcanic gas reservoir, it is necessary to keep the pore pressure at a high value to reduce the damage caused by the permeability stress sensitivity.

5. Discussion

Based on the results of the above experiments, the volcanic rock reservoir in this study has some special characteristics. The quartz content and clay content of the target formation in the Yingtai region do not have clear tendency with depth. So, the segment choice of hydraulic fracturing needs more consideration by the mineral components evaluation. At the same time the average clay content is 39.5%, which is a relatively higher content. There might be formation damage while adopting hydraulic fracturing [59], where the degree is dependent on the clay content and water property injected.

There are some initial microfractures in volcanic reservoirs. When these initial fractures connect with the hydraulic fractures, the reservoir permeability can be improved greatly. However, these microfractures affect the volcanic rock permeability stress sensitivity. Furthermore, the fluid pressure decline has significant influence on the permeability stress sensitivity after hydraulic fracturing is performed. The strong permeability stress sensitivity requires measures for keeping the formation fluid pressure at a high value to realize long term development.

Centrifuge tests indicate that volcanic rocks have high irreducible water saturation. Combined with the field data, the initial water saturation is often far less than the irreducible water saturation, so the reservoirs have a strong capacity to absorb much fracturing liquid. Based on this characteristic, we should take the fracturing fluid imbibition property into consideration when choosing the low filtration fluid to exert hydraulic fracturing.

Volcanic rocks in this work are full of micropores as shown by nuclear magnetic resonance tests. Most micropores have less contribution to the formation permeability, which is presented by way of the pulse-decay permeability measurement in the process of spontaneous imbibition. In the late period of spontaneous imbibition, the sample permeability

maintains stability while the water content increases. From the nuclear magnetic resonance experiment, we can find that micropores make up most of the porosity. The large pores and quick fractures were filled by liquid. Micropores absorb water slowly. However, these micropores have a strong capacity to absorb a large amount of water, which is beneficial to the permeability recovery and autoremoving aqueous phase trapping after the volcanic reservoir is subjected to hydraulic fracturing.

A large amount of fracturing fluid retention becomes a common phenomenon after hydraulic fracturing is performed in a tight reservoir. However, the permeability can be improved by performing a well shut-in for a period of time. Because micropores have a strong capacity to absorb fracturing liquid from other pores ranging from large pores to micropores, larger pores have a greater contribution to reservoir permeability than micropores, which was demonstrated by the experiments. Under the effect of capillary force, the main gas flowing channel becomes very large, so the entire permeability of the formation increases.

Two equations were proposed to forecast the volcanic reservoir stress sensitivity in the process of loading pressure and unloading pressure. The volcanic rocks have strong permeability stress sensitivity. So, keeping the pore pressure at a high level is very important in efficiently developing volcanic reservoirs.

6. Conclusions

The volcanic reservoir is an important tight reservoir. Efficient hydraulic fracturing and development contribute to commercial production of this type of reservoir. The study was trying to get the factors influencing the hydraulic fracturing based on the petrophysical properties. The following conclusions can be made regarding the volcanic reservoir in Songliao Basin, China.

(1) Quartz and clays are the main components in rocks of the research formation. Natural cracks also appear in the samples. These characteristics indicate that, during hydraulic fracturing, abundant quartz and natural cracks promote the generation of network fractures. However, the lack of understanding of the mineralogical effect (i.e., clays) and the challenges on sample heterogeneity increase the difficulty of selection of segments to fracturing.

(2) There is a quick decrease of rock permeability once the rock contacts water, which indicates that aqueous phase trapping (APT) happens when the fracturing fluids are pumped into the formation. The high irreducible water saturation causes the formation to be accompanied by strong spontaneous imbibition due to the low initial water saturation of prolific unconventional reservoirs. Also, the nanopores have strong capillary force, causing the liquid to migrate into the formation, which significantly influences the permeability of the formation. Fast flow-back scheme is applicable in this situation to minimize the damage.

(3) The pores filled during spontaneous imbibition are mainly the nanopores from NMR spectra. Because lots of water imbibed into the nanopores, the main flow channels become larger, which is beneficial to the permeability

recovery after flow-back of hydraulic fracturing. This is helpful to understand the APT autoremoving of some volcanic reservoirs.

(4) Strong permeability sensitivity appears in volcanic rocks. Keeping the appropriate production differential pressure is very important in achieving the long term efficient development of volcanic gas reservoirs.

Conflicts of Interest

The authors declare that there are no conflicts of interest regarding the publication of paper.

Acknowledgments

This work was supported by the National Natural Science Foundation of China (51604287, 51490652), Science Foundation of China University of Petroleum-Beijing at Karamay (no. RCYJ2016B-01-001), SINOPEC Scientific Research Program "Micro-Nano Capillary Imbibition and Damage Mechanism of Unconventional Oil/Gas Reservoir," and National 973 Project "Control Mechanism for Productive Formations and Repeated Fracturing of Artificial Joint Networks of Low-Permeability Reservoirs" (no. 2015CB250903).

References

- [1] N. B. Tchumegnie Ngongang, P. Kamgang, G. Chazot, A. Agranier, H. Bellon, and P. Nonnotte, "Age, geochemical characteristics and petrogenesis of Cenozoic intraplate alkaline volcanic rocks in the Bafang region, West Cameroon," *Journal of African Earth Sciences*, vol. 102, pp. 218–232, 2015.
- [2] M. Kheirikhah, I. Neill, and M. B. Allen, "Petrogenesis of OIB-like basaltic volcanic rocks in a continental collision zone: Late Cenozoic magmatism of Eastern Iran," *Journal of Asian Earth Sciences*, vol. 106, pp. 19–33, 2015.
- [3] Y. Sun, J. Ying, B. Su, X. Zhou, and J. Shao, "Contribution of crustal materials to the mantle sources of Xiaogulihe ultrapotassic volcanic rocks, Northeast China: New constraints from mineral chemistry and oxygen isotopes of olivine," *Chemical Geology*, vol. 405, pp. 10–18, 2015.
- [4] A. M. Paiaman, J. Moghadasi, and M. Masihi, "Formation damage through aqueous phase trapping in gas reservoirs," in *Proceedings of the Deep Gas Conference and Exhibition 2010, DGAS 2010*, pp. 43–50, January 2010.
- [5] D. B. Bennion, F. B. Thomas, R. F. Bietz, and D. W. Bennion, "Remediation of water and hydrocarbon phase trapping problems in low permeability gas reservoirs," *Journal of Canadian Petroleum Technology*, vol. 38, no. 8, pp. 39–48, 1999.
- [6] L. You and Y. Kang, "Integrated evaluation of water phase trapping damage potential in tight gas reservoirs," in *Proceedings of the 8th European Formation Damage Conference*, Scheveningen, The Netherlands, 2009.
- [7] Y. Shen, H. Ge, C. Li et al., "Water imbibition of shale and its potential influence on shale gas recovery—a comparative study of marine and continental shale formations," *Journal of Natural Gas Science and Engineering*, vol. 35, pp. 1121–1128, 2016.
- [8] Y. Shen, H. Ge, S. Su, D. Liu, Z. Yang, and J. Liu, "Imbibition characteristic of shale gas formation and water-block removal capability," *Scientia Sinica Physica, Mechanica & Astronomica*, vol. 47, no. 11, article 114609, 2017.

- [9] S. Akin, J. M. Schembre, S. K. Bhat, and A. R. Kovscek, "Spontaneous imbibition characteristics of diatomite," *Journal of Petroleum Science and Engineering*, vol. 25, no. 3-4, pp. 149–165, 2000.
- [10] M. Chahardowli, A. Zholdybayeva, R. Farajzadeh, and H. Bruining, "Solvent-enhanced spontaneous imbibition in fractured reservoirs," in *Proceedings of the EAGE Annual Conference & Exhibition incorporating SPE Europe.*, Society of Petroleum Engineers, 2013.
- [11] N. R. Morrow and G. Mason, "Recovery of oil by spontaneous imbibition," *Current Opinion in Colloid & Interface Science*, vol. 6, no. 4, pp. 321–337, 2001.
- [12] Q. Lan, E. Ghanbari, H. Dehghanpour, and R. Hawkes, "Water Loss Versus Soaking Time: Spontaneous Imbibition in Tight Rocks," *Energy Technology*, vol. 2, no. 12, pp. 1033–1039, 2014.
- [13] J. Cai, L. Luo, R. Ye, X. Zeng, and X. Hu, "Recent advances on fractal modeling of permeability for fibrous porous media," *Fractals*, vol. 23, no. 1, Article ID 1540006, 2015.
- [14] J. Cai, X. Hu, B. Xiao, Y. Zhou, and W. Wei, "Recent developments on fractal-based approaches to nanofluids and nanoparticle aggregation," *International Journal of Heat and Mass Transfer*, vol. 105, pp. 623–637, 2017.
- [15] D. Lin, J. Wang, B. Yuan, and Y. Shen, "Review on gas flow and recovery in unconventional porous rocks," *Advances in Geo-Energy Research*, vol. 1, no. 1, pp. 39–53, 2017.
- [16] X. Dou, X. Liao, X. Zhao, H. Wang, and S. Lv, "Quantification of permeability stress-sensitivity in tight gas reservoir based on straight-line analysis," *Journal of Natural Gas Science and Engineering*, vol. 22, pp. 598–608, 2015.
- [17] J. Yang, R. Liu, and H. Liu, "A universal model of stress sensitive coefficient in low permeability reservoir," in *Proceedings of the 2011 SREE Conference on Engineering Modelling and Simulation, CEMS 2011*, pp. 177–183, August 2011.
- [18] Y. Tian, "Experimental study on stress sensitivity of naturally fractured reservoirs," in *Proceedings of the SPE Annual Technical Conference and Exhibition*, Amsterdam, The Netherlands, 2014.
- [19] I. Fatt and D. Davis, "Reduction in Permeability With Overburden Pressure," *Journal of Petroleum Technology*, vol. 4, no. 12, pp. 16–16, 2013.
- [20] A. McLatchie, R. Hemstock, and J. Young, "The Effective Compressibility of Reservoir Rock and Its Effects on Permeability," *Journal of Petroleum Technology*, vol. 10, no. 06, pp. 49–51, 2013.
- [21] D. H. Gray and I. Fatt, "The Effect of Stress on Permeability of Sandstone Cores," *SPE Journal*, vol. 3, no. 02, pp. 95–100, 2013.
- [22] H. Xu, D. Tang, J. Zhao, and S. Li, "A precise measurement method for shale porosity with low-field nuclear magnetic resonance: A case study of the Carboniferous-Permian strata in the Linxing area, eastern Ordos Basin, China," *Fuel*, vol. 143, pp. 47–54, 2015.
- [23] K. E. Washburn and J. E. Birdwell, "Application of binomial-edited CPMG to shale characterization," *Journal of Magnetic Resonance*, vol. 246, pp. 72–78, 2014.
- [24] J. Mitchell, T. C. Chandrasekera, D. J. Holland, L. F. Gladden, and E. J. Fordham, "Magnetic resonance imaging in laboratory petrophysical core analysis," *Physics Reports*, vol. 526, no. 3, pp. 165–225, 2013.
- [25] R. Lewis, P. Singer, T. Jiang, E. Rylander, S. Sinclair, and R. H. McClain, "NMR T2 distributions in the eagle ford shale: reflections on pore size," in *Proceedings of the SPE Unconventional Resources Conference*, Society of Petroleum Engineers, 2013.
- [26] K. Munn and D. M. Smith, "A NMR technique for the analysis of pore structure: Numerical inversion of relaxation measurements," *Journal of Colloid and Interface Science*, vol. 119, no. 1, pp. 117–126, 1987.
- [27] W. E. Kenyon, "Nuclear magnetic resonance as a petrophysical measurement. The International journal of radiation applications and instrumentation," *Part E. Nuclear Geophysics*, vol. 6, no. 2, pp. 153–171, 1992.
- [28] X. Cui, A. M. M. Bustin, and R. M. Bustin, "Measurements of gas permeability and diffusivity of tight reservoir rocks: Different approaches and their applications," *Geofluids*, vol. 9, no. 3, pp. 208–223, 2009.
- [29] A. I. Dicker and R. M. Smits, "Practical approach for determining permeability from laboratory pressure-pulse decay measurements," in *Proceedings of the International Meeting on Petroleum Engineering*, Society of Petroleum Engineers, November 1988.
- [30] S. C. Jones, "A technique for faster pulse-decay permeability measurements in tight rocks," *SPE Formation Evaluation*, vol. 12, no. 1, pp. 19–24, 1997.
- [31] E. Ghanbari and H. Dehghanpour, "Impact of rock fabric on water imbibition and salt diffusion in gas shales," *International Journal of Coal Geology*, vol. 138, pp. 55–67, 2015.
- [32] S. Kale, C. Rai, and C. Sondergeld, "Rock typing in gas shales," in *Proceedings of the SPE Annual Technical Conference and Exhibition*, Society of Petroleum Engineers.
- [33] Z.-Q. Feng, "Volcanic rocks as prolific gas reservoir: A case study from the Qingshen gas field in the Songliao Basin, NE China," *Marine and Petroleum Geology*, vol. 25, no. 4-5, pp. 416–432, 2008.
- [34] T. Kawamoto and K. Sato, "Geological modelling of a heterogeneous volcanic reservoir by the petrological method," in *Proceedings of the SPE Asia Pacific Conference on Integrated Modelling for Asset Management "Rising to the Challenges of Enhancing our Assets"*, pp. 97–104, Society of Petroleum Engineers, April 2000.
- [35] D. Weng, Q. Lei, Y. Ding et al., "Case Study: Massive hydraulic fracturing in volcanic gas, China," in *Proceedings of the SPE Production and Operations Symposium*, Society of Petroleum Engineers.
- [36] C. M. Fuller and J. M. Sharp Jr., "Permeability and fracture patterns in extrusive volcanic rocks: implications from the welded Santana Tuff, Trans-Pecos Texas," *Geological Society of America Bulletin*, vol. 104, no. 11, pp. 1485–1496, 1992.
- [37] C. H. Sondergeld, K. E. Newsham, J. T. Comisky, M. C. Rice, and C. S. Rai, "Petrophysical considerations in evaluating and producing shale gas resources," in *Proceedings of the SPE Unconventional Gas Conference 2010*, pp. 99–132, Society of Petroleum Engineers, February 2010.
- [38] R. Dutta, C.-H. Lee, S. Odumabo et al., "Experimental investigation of fracturing-fluid migration caused by spontaneous imbibition in fractured low-permeability sands," *SPE Reservoir Evaluation and Engineering*, vol. 17, no. 1, pp. 74–81, 2014.
- [39] R. F. Sigal, "Pore-Size distributions for organic-Shale- Reservoir rocks from nuclear-magnetic- resonance spectra combined with adsorption measurements," *SPE Journal*, vol. 20, no. 4, pp. 824–830, 2015.
- [40] M. Meng, H. Ge, W. Ji, and X. Wang, "Research on the auto-removal mechanism of shale aqueous phase trapping using low field nuclear magnetic resonance technique," *Journal of Petroleum Science and Engineering*, vol. 137, pp. 63–73, 2016.

- [41] G. R. Coates, L. Xiao, and M. G. Prammer, *NMR Logging: Principles and Applications*, Gulf Professional Publishing, 1999.
- [42] M. Appel, "Nuclear magnetic resonance and formation porosity," *Petrophysics*, vol. 45, no. 3, pp. 296–307, 2004.
- [43] B. Roychoudhuri, T. T. Tsotsis, and K. Jessen, "An experimental investigation of spontaneous imbibition in gas shales," *Journal of Petroleum Science and Engineering*, vol. 111, pp. 87–97, 2013.
- [44] J. M. Schembre, S. Akin, L. M. Castanier, and A. R. Kavscek, "Spontaneous water imbibition into diatomite," in *Proceedings of the 1998 68th Annual Western Regional Meeting*, May 1998.
- [45] A. Javaheri, H. Dehghanpour, and J. M. Wood, "Tight rock wettability and its relationship to other petrophysical properties: a Montney case study," *Journal of Earth Science*, vol. 28, no. 2, pp. 381–390, 2017.
- [46] M. Akbarabadi, "Nanotomography of Spontaneous Imbibition in Shale," in *Proceedings of the Unconventional Resources Technology Conference (URTEC)*, 2014.
- [47] M. Meng, H. Ge, W. Ji, X. Wang, and L. Chen, "Investigation on the variation of shale permeability with spontaneous imbibition time: Sandstones and volcanic rocks as comparative study," *Journal of Natural Gas Science and Engineering*, vol. 27, pp. 1546–1554, 2015.
- [48] E. Fathi and I. Y. Akkutlu, "Multi-component gas transport and adsorption effects during CO₂ injection and enhanced shale gas recovery," *International Journal of Coal Geology*, vol. 123, pp. 52–61, 2014.
- [49] A. Ghanizadeh, S. Bhowmik, O. Haeri-Ardakani, H. Sanei, and C. R. Clarkson, "A comparison of shale permeability coefficients derived using multiple non-steady-state measurement techniques: examples from the Duvernay Formation, Alberta (Canada)," *Fuel*, vol. 140, pp. 371–387, 2015.
- [50] A. Sakhaee-Pour and S. Bryant, "Gas Permeability of Shale," *SPE Reservoir Evaluation & Engineering*, vol. 15, no. 04, pp. 401–409, 2013.
- [51] M. Zamirian, K. Aminian, S. Ameri, and E. Fathi, "New steady-state technique for measuring shale core plug permeability," in *Proceedings of the SPE Canadian Unconventional Resources Conference 2014*, pp. 598–608, October 2014.
- [52] I. Yucel Akkutlu and E. Fathi, "Multiscale gas transport in shales with local kerogen heterogeneities," *SPE Journal*, vol. 17, no. 4, pp. 1002–1011, 2012.
- [53] S. M. Kang, E. Fathi, R. J. Ambrose, I. Y. Akkutlu, and R. F. Sigal, "Carbon dioxide storage capacity of organic-rich shales," *SPE Journal*, vol. 16, no. 4, pp. 842–855, 2011.
- [54] X. Fu, F. Agostini, F. Skoczylas, and L. Jeannin, "Experimental study of the stress dependence of the absolute and relative permeabilities of some tight gas sandstones," *International Journal of Rock Mechanics and Mining Sciences*, vol. 77, pp. 36–43, 2015.
- [55] Q. Lei, W. Xiong, J. Yuang, Y. Cui, and Y. Wu, "Analysis of stress sensitivity and its influence on oil production from tight reservoirs," in *Proceedings of the Eastern Regional Meeting*, 2007.
- [56] R. A. Farquhar, B. G. D. Smart, A. C. Todd, D. E. Tompkins, and A. J. Tweedie, "Stress sensitivity of low petroleum sandstones from the rotliegendes sandstone," in *Proceedings of the SPE Annual Technical Conference and Exhibition*, pp. 851–861, Society of Petroleum Engineers, October 1993.
- [57] H. Belyadi, E. Fathi, and F. Belyadi, "Managed pressure drawdown in Utica/Point Pleasant with case studies," in *Proceedings of the 2016 SPE Eastern Regional Meeting, ERM 2016*, September 2016.
- [58] J.-J. Dong, J.-Y. Hsu, W.-J. Wu et al., "Stress-dependence of the permeability and porosity of sandstone and shale from TCDDP Hole-A," *International Journal of Rock Mechanics and Mining Sciences*, vol. 47, no. 7, pp. 1141–1157, 2010.
- [59] F. Civan, *Reservoir Formation Damage*, 2nd edition, 2007.

Research Article

A Semianalytical Model for Multiple-Fractured Horizontal Wells with SRV in Tight Oil Reservoirs

Jiahang Wang,^{1,2,3} Xiaodong Wang,^{1,2} and Wenxiu Dong^{1,3}

¹School of Energy Resource, China University of Geosciences (Beijing), Beijing 100083, China

²Key Laboratory of Strategy Evaluation for Shale Gas, Ministry of Land and Resources, Beijing 100083, China

³Beijing Key Laboratory of Unconventional Natural Gas Geological Evaluation and Development Engineering, Beijing 100083, China

Correspondence should be addressed to Xiaodong Wang; wangxd_cugb@126.com

Received 20 June 2017; Revised 4 September 2017; Accepted 17 October 2017; Published 29 November 2017

Academic Editor: Ebrahim Fathi

Copyright © 2017 Jiahang Wang et al. This is an open access article distributed under the Creative Commons Attribution License, which permits unrestricted use, distribution, and reproduction in any medium, provided the original work is properly cited.

The paper developed a new semianalytical model for multiple-fractured horizontal wells (MFHWs) with stimulated reservoir volume (SRV) in tight oil reservoirs by combining source function theory with boundary element idea. The model is first validated by both analytical and numerical model. Then new type curves are established. Finally, the effects of SRV shape, SRV size, SRV permeability, and parameters of hydraulic fractures are discussed. Results show that SRV has great influence on the pressure response of MFHWs; the parameters of fractures, such as fracture distribution, length, and conductivity, also can affect the transient pressure of MFHWs. One novelty of this model is to consider the nonlinear flow around hydraulic fracture tips. The other novelty is the ability to model the shape of the SRV, production behavior of different fractures, and interfaces. Compared to numerical and analytic methods, this model can not only reduce extensive computing processing but also show high accuracy.

1. Introduction

With the increasing demand of energy market and great progress of hydraulic fracturing technology, the exploration of unconventional resources such as tight oil, tight gas, and shale gas becomes more and more important [1–5]. Compared to the conventional hydraulic fracturing and horizontal wells, multiple-fractured horizontal wells technology can form a certain enhanced region with induced fractures near the hydraulic fractures, which changes the flow pattern, reduces the flow resistance, and improves the production of a single well [6, 7]. However, establishing a dynamic analysis model of MFHWs with stimulated reservoir volume (SRV) under such complex geological conditions is difficult. One of the difficulties is that it is hard to describe the degree and shape of the SRV accurately. The other one is that it is difficult to deal with the coupling between the enhanced region and unstimulated region.

Many scholars have done a lot of researches on SRV characterization and its effects on well performance. Various analytical and detailed numerical models have been proposed. Among these models, multilinear models are the most

widely used. Ozkan et al. [8, 9] utilized a trilinear flow model to investigate the MFHWs performance in unconventional reservoirs. Brown et al. [10] proposed an analytical trilinear flow model to describe the pressure distribution for a system, where the enhanced region occupies entire spaces near the fractures. Stalgorova and Mattar [11] improved the trilinear flow model by simplifying the SRV into an enhanced region with limited width. Five regions are defined to simulate the SRV and all the flow in these regions is linear. Guo et al. [12] presented an analytical model for the multistage fractured shale reservoir, considering heterogeneity, typical seepage characters, and fluids flow from upper/lower reservoir. The model is similar to five-region-flow model but subdivides the reservoir into seven parts.

Many other researchers try to replace the shape of SRV with other methods. Ketinen and Ertekin [13] generated a composite natural fractured system solution in elliptical flow geometry. The enhanced region is simulated by the elliptical flow model. Like other elliptical studies, the reservoir pressure with a series of Mathieu functions is obtained. The model is complex and cannot describe the geometry of the main fracture. Zhao et al. [14] simplified the model

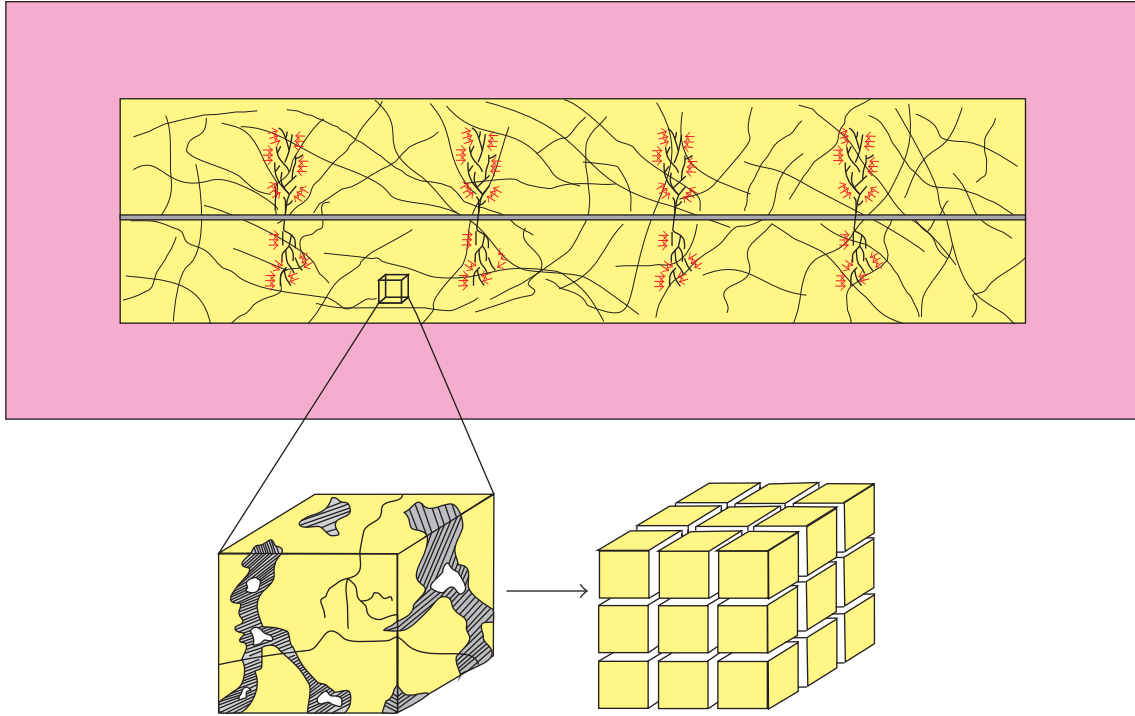


FIGURE 1: Schematic of MFHW with SRV in a rectangular reservoir.

by describing the shape of enhanced region as circle. Ozcan et al. [15] and Wang [16] combined linear flow with fractal theory and provided alternative method to simulate well performance in fractured reservoir. Although the fractal model can well describe the spatial distribution of fractures, it cannot optimize the parameters of hydraulic fracture.

Despite the efforts presented in the literature, all above models are limited by two assumptions. One assumption is that the fluid flow in all regions is linear. In fact, innovative fracturing techniques such as “Simulfrac” and “Zipperfrac” can create an enhanced region with high density network of fractures [17]. The flow in the enhanced region near hydraulic fracture tips may no longer behave like linear flow, but, instead, radial flow. Existing multilinear models become inapplicable. The other deficient assumption is that both the shapes of unstimulated and enhanced region are simplified as circles. In fact, due to the long length of the horizontal wellbore, the shape of enhanced region should be approximately ellipse or rectangle rather than circle.

The object of this paper is to establish a semianalytical model for MFHWs with SRV in tight reservoirs. To overcome the limitations, this study combines the point source/sink theory with boundary element idea to solve the seepage flow. The reservoir is divided into several subsystems. The subsystems in the enhanced region are modeled by Warren-Root [18] dual-porosity model. The fluid flow near the fracture tips includes both linear flow and radial flow. The transient pressure responses of MFHWs with considering the effect of SRV are investigated and the influence of relevant parameters on type curves is also analyzed.

2. Methodology

2.1. Physical Model and Assumptions. The schematic diagram for a MFHW in a tight oil reservoir is shown in Figure 1. Propagation of fractures can create branch patterns [19]. Fracture branching creates a stimulated reservoir volume around each artificial hydraulic fracture, which can be modeled by introducing a region of higher permeability. According to the reservoir physical conditions, the whole reservoir is subdivided into inner and outer regions. The inner region is composed of matrix, natural fractures, and induced fractures, which can be simulated by Warren-Root [18] dual-porosity model. The outer region is an unstimulated homogeneous media which is not influenced by hydraulic fractures. The basic assumptions of the model are as follows:

- (1) The MFHW is located in the center of a rectangular tight oil reservoir with impermeable outer boundaries and produces at a constant rate q . n_f artificial hydraulic fractures distribute evenly along the horizontal wellbore.
- (2) The thickness of reservoir is h and uniform initial pressure is p_i .
- (3) The formation is fully penetrated by the artificial hydraulic fractures.
- (4) Isothermal single phase fluid flow is assumed.
- (5) The influence of gravity and capillary forces on fluid flow in both regions is ignored.

2.2. Mathematical Model and Solution

2.2.1. Mathematical Model. In order to describe the complex flow model stated above accurately, we combine the

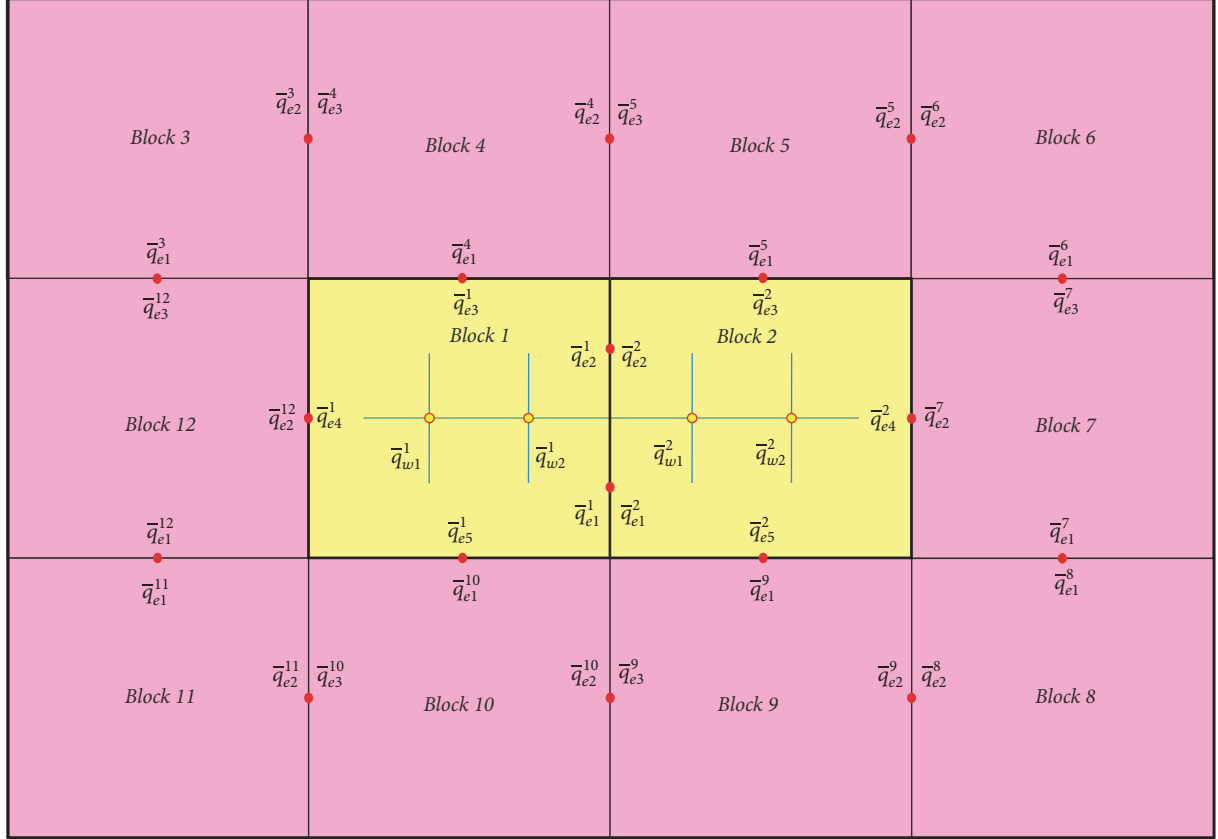


FIGURE 2: The grid model for MFHW with SRV in a rectangular reservoir.

source/sink theory with boundary element idea. The whole reservoir is subdivided into 12 discrete blocks based on the reservoir properties. Due to the fully penetration of the fractures, the issue can be studied in two dimensions (Figure 2). For convenience, the solutions of this model are founded on dimensionless variables. These dimensionless parameters are defined as follows:

$$p_{jD} = \frac{\alpha_p \lambda_{\text{ref}} h (p_i - p_j)}{qB};$$

$$t_D = \frac{\alpha_t \eta_{\text{ref}} t}{L_f^2};$$

$$c_{fiD} = \frac{k_{fi} w_{fi}}{k_i L_{fi}};$$

$$q_{wiD} = \frac{q_{wi}(t) 2 y_{fi} h}{qB};$$

$$q_{ejD} = \frac{q_{ej}(t) 2 \delta_{pj} h}{qB}, \quad \delta = x, y,$$

$$\lambda_{\text{in-out}j} = \frac{(k/\mu)_j}{(k/\mu)_{\text{ref}}};$$

$$\omega_{\text{in-out}j} = \frac{(\phi c_t)_j}{(\phi c_t)_{\text{ref}}};$$

$$\eta_{jD} = \frac{\eta_j}{\eta_{\text{ref}}} = \frac{\lambda_{\text{in-out}j}}{\omega_{\text{in-out}j}},$$

$$y_{fiD} = \frac{y_{fi}}{L_f};$$

$$y_D = \frac{y}{L_f};$$

$$y_{wiD} = \frac{y_{wi}}{L_f};$$

$$y_{eDj} = \frac{y_{ej}}{L_f},$$

$$x_D = \frac{x}{L_f};$$

$$x_{wiD} = \frac{x_{wi}}{L_f};$$

$$x_{eDj} = \frac{x_{ej}}{L_f}.$$

The dimensionless pressure of horizontal well is p_{wD} . The dimensionless flux and pressure at the center of i th fracture in block k are $\bar{q}_{wDi}^k, \bar{p}_{wDi}^k, i = 1, 2, \dots, nf/2; k = 1, 2$, respectively. The dimensionless flux and pressure at the center of j th interface segment in block k are $\bar{q}_{eDj}^k, \bar{p}_{eDj}^k, j = 1, 2, \dots, 5, k = 1, 2, \dots, 12$, respectively.

2.2.2. Solution. When $n + m$ sources/sinks in a reservoir produce simultaneously, the dimensionless pressure drop at any location (x_D, y_D) in the reservoir is equal to the sum of the dimensionless pressure drop caused by every single sources/sink [6]. Since the flux of each source/sink is a function of time, according to the Duhamel convolution, the pressure distribution in Laplace transform domain can be expressed as

$$\Delta \bar{p}_D = \left[\sum_{i=1}^n \bar{q}_{wDi} \cdot \bar{S}_{wi} \right] + \left[\sum_{j=1}^m \bar{q}_{eDj} \cdot \bar{S}_{ej} \right]. \quad (2)$$

Due to the full penetration of the fractures, both the source functions for hydraulic fractures and interface segments are line source function. $\bar{S}_\alpha, \alpha = wDi$ (hydraulic fracture) and $\alpha = eDj$ (interface segment), can be expressed as follows [20]:

$$\begin{aligned} \bar{S}_{wDi} &= \frac{\omega_{in-outi}}{\lambda_{in-outi}} \left\{ \frac{\pi}{y_{eDi}} \bar{H}_{y0} \right. \\ &\quad \left. + \frac{2}{y_{pi}} \sum_{n=1}^{\infty} \frac{1}{n} \bar{H}_{yn} \cos \frac{n\pi y_{wDi}}{y_{eDi}} \cos \frac{n\pi y_D}{y_{eDi}} \sin \frac{n\pi y_{pi}}{y_{eDi}} \right\}, \end{aligned} \quad (3)$$

$$\begin{aligned} \bar{S}_{eDj} &= \frac{\omega_{in-outj}}{\lambda_{in-outj}} \left\{ \frac{\pi}{\delta_{eDj}} \bar{H}_{\delta 0} \right. \\ &\quad \left. + \frac{2}{\delta_{pj}} \sum_{n=1}^{\infty} \frac{1}{n} \bar{H}_{\delta n} \cos \frac{n\pi \delta_{wDj}}{\delta_{eDj}} \cos \frac{n\pi \delta_D}{\delta_{eDj}} \sin \frac{n\pi \delta_{pj}}{\delta_{eDj}} \right\}, \end{aligned}$$

where

$$\begin{aligned} \bar{H}_{\delta n} &= \begin{cases} \frac{\cosh \varepsilon_{an} (y_{eDj} - |y_D \pm y_{wjD}|)}{\varepsilon_{an} \sinh \varepsilon_{an} y_{eDj}} & \delta = x \\ \frac{\cosh \varepsilon_{an} (x_{eDi} - |x_D \pm x_{wiD}|)}{\varepsilon_{an} \sinh \varepsilon_{an} x_{eDi}} & \delta = y, \end{cases} \quad (4) \\ \varepsilon_{an} &= \begin{cases} \sqrt{u_\delta + \frac{n^2 \pi^2}{y_{eDi}^2}} & \alpha = wDi \\ \sqrt{u_\delta + \frac{n^2 \pi^2}{\delta_{eDj}^2}} & \alpha = eDj; \end{cases} \end{aligned}$$

$$u_\delta = \begin{cases} \frac{u}{\lambda_{in-outi}} & \delta = y, \alpha = wDi \\ \frac{u}{\lambda_{in-outj}} & \delta = x, y, \alpha = eDj \end{cases}$$

$$u = \begin{cases} s \\ sf(s); \end{cases}$$

$$f(s) = \frac{s\omega_{m-f}(1 - \omega_{m-f}) + \lambda_{m-f}}{s(1 - \omega_{m-f}) + \lambda_{m-f}}. \quad (5)$$

δ_{pj} is the half length of the j th source/sink for the inner/outer boundary; s is for homogeneous reservoirs and $sf(s)$ is for naturally fractured reservoirs.

In order to consider the fracture conductivity, we use the results of Riley [21] here. The source function for the hydraulic fracture considering the fracture conductivity can be written by

$$\begin{aligned} \bar{S}_{wDi} &= \frac{\omega_{in-outi}}{\lambda_{in-outi}} \left\{ \frac{\pi}{y_{eDi}} \bar{H}_{x0} \right. \\ &\quad \left. + \frac{2}{y_{pi}} \sum_{n=1}^{\infty} \frac{1}{n} \bar{H}_{yn} \cos \frac{n\pi y_{wDi}}{y_{eDi}} \cos \frac{n\pi y_D}{y_{eDi}} \sin \frac{n\pi y_{pi}}{y_{eDi}} \right. \\ &\quad \left. + u_y \bar{f}(c_{fiD}) \right\}, \end{aligned} \quad (6)$$

$$\begin{aligned} u_y \bar{f}(c_{fiD}) &= 2\pi \sum_{n=1}^{\infty} \frac{1}{n^2 \pi^2 c_{fiD} + 2\sqrt{n^2 \pi^2 + u_x}} \\ &\quad + \frac{0.4063\pi}{\pi(c_{fiD} + 0.8997) + 1.6252u_x}, \end{aligned}$$

where $u_y \bar{f}(c_{fiD})$ is the finite-conductivity function for the i th fracture.

Here we consider a MFHW with nf hydraulic fractures. Both block 1 and block 2 have $nf/2$ hydraulic fractures. Writing (2) at the center of all fractures and interface segments shown in Figure 2 yields the following set of $18 \times 2 + nf$ linear equations which contain $2 \times (18 \times 2 + nf)$ unknowns, $\bar{p}_{wDi}^k, \bar{p}_{eDj}^k, \bar{q}_{wDi}^k, \bar{q}_{eDj}^k$;

$$\begin{aligned} \bar{p}_{wDi}^k &= \left[\sum_{n=1}^{nf/2} \bar{q}_{wDn}^k \cdot \bar{S}_{wDiwDn}^k \right] \\ &\quad + \left[\sum_{m=1}^5 \bar{q}_{eDm}^k \cdot \bar{S}_{wDieDm}^k \right], \end{aligned} \quad (7)$$

$$k = 1, 2, \quad i = 1, 2, \dots, \frac{nf}{2},$$

$$\begin{aligned} \bar{p}_{eDj}^k = & \left[\sum_{n=1}^{nf/2} \bar{q}_{wDn}^k \cdot \bar{S}_{eDjwDn}^k \right] \\ & + \left[\sum_{m=1}^5 \bar{q}_{eDm}^k \cdot \bar{S}_{eDjeDm}^k \right], \end{aligned} \quad (8)$$

$$k = 1, 2, \quad j = 1, 2, \dots, 5,$$

$$\bar{p}_{eDj}^k = \sum_{m=1}^3 \bar{q}_{eDm}^k \cdot \bar{S}_{eDjeDm}^k \quad (9)$$

$$k = 4, 5, 7, 9, 10, 12, \quad j = 1, 2, 3,$$

$$\bar{p}_{eDj}^k = \sum_{m=1}^2 \bar{q}_{eDm}^k \cdot \bar{S}_{eDjeDm}^k = 0, \quad (10)$$

$$k = 3, 6, 8, 11, \quad j = 1, 2.$$

The pressure of different blocks for the same interfaces is equal and the flux of interfaces is continuous. Taking block 1 and block 2 as an example,

$$\begin{aligned} \bar{p}_{eD1}^1 &= \bar{p}_{eD1}^2; \\ \bar{q}_{eD1}^1 &= -\bar{q}_{eD1}^2; \\ \bar{p}_{eD2}^1 &= \bar{p}_{eD2}^2; \\ \bar{q}_{eD2}^1 &= -\bar{q}_{eD2}^2; \\ \bar{p}_{eD3}^1 &= \bar{p}_{eD1}^4; \\ \bar{q}_{eD3}^1 &= -\bar{q}_{eD1}^4; \\ \bar{p}_{eD4}^1 &= \bar{p}_{eD2}^{12}; \\ \bar{q}_{eD4}^1 &= -\bar{q}_{eD2}^{12}; \\ \bar{p}_{eD5}^1 &= \bar{p}_{eD1}^{10}; \\ \bar{q}_{eD5}^1 &= -\bar{q}_{eD1}^{10}; \end{aligned} \quad (11)$$

$$\begin{aligned} \bar{p}_{eD1}^1 - \bar{p}_{eD1}^2 &= \left\{ \left[\sum_{n=1}^{nf/2} \bar{q}_{wDn}^1 \cdot \bar{S}_{eD1wDn}^1 \right] \right. \\ &+ \left. \left[\sum_{m=1}^5 \bar{q}_{eDm}^1 \cdot \bar{S}_{eD1eDm}^1 \right] \right\} \\ &- \left\{ \left[\sum_{n=1}^{nf/2} \bar{q}_{wDn}^2 \cdot \bar{S}_{eD1wDn}^2 \right] \right. \\ &+ \left. \left[\sum_{m=1}^5 \bar{q}_{eDm}^2 \cdot \bar{S}_{eD1eDm}^2 \right] \right\} = \left[\sum_{n=1}^{nf/2} \bar{q}_{wDn}^1 \cdot \bar{S}_{eD1wDn}^1 \right] \\ &- \left[\sum_{n=1}^{nf/2} \bar{q}_{wDn}^2 \cdot \bar{S}_{eD1wDn}^2 \right] \end{aligned}$$

$$\begin{aligned} &+ \sum_{m=1}^2 \left[\bar{S}_{eD1eDm}^1 + \bar{S}_{eD1eDm}^2 \right] \cdot \bar{q}_{eDm}^1 + \left[\sum_{m=3}^5 \bar{q}_{eDm}^1 \right. \\ &\cdot \bar{S}_{eD1eDm}^1 \left. \right] - \left[\sum_{m=3}^5 \bar{q}_{eDm}^2 \cdot \bar{S}_{eD1eDm}^2 \right] = 0. \end{aligned} \quad (12)$$

Ignoring the pressure depletion along the horizontal wellbore, the pressure of each fracture is approximately the same which is equal to the pressure of horizontal wellbore. Then we can have nf additional equations:

$$\bar{p}_{wD1}^k = \bar{p}_{wD2}^k = \dots = \bar{p}_{wDnf/2}^k = \bar{p}_{wD}, \quad (13)$$

$$\text{for } k = 1, 2,$$

$$\bar{p}_{wDi}^1 - \bar{p}_{wDi}^2 = 0, \quad \text{for } i = 1, 2, \dots, \frac{nf}{2}. \quad (14)$$

The sum of the flux of each fracture is equal to the well production rate:

$$\sum_{k=1}^2 \sum_{i=1}^{nf/2} s \bar{q}_{wDi}^k = 1. \quad (15)$$

The linear system defined by (7)–(15) now has $18 + nf + 1$ equations with $18 + nf + 1$ unknowns.

$$AX = b. \quad (16)$$

Eq. (16) can be solved by Gaussian elimination method. By solving (16), the instantaneous flux of each fracture and the wellbore pressure of MFHW with SRV in a rectangular tight oil reservoir with constant rate condition can be obtained. The whole workflow is shown in Figure 3. Here we take a MFHW with four fractures as an example and A , X , b are shown in Appendix.

3. Comparison and Validation

In order to verify the accuracy of proposed model, we compare the results of semianalytical model with that of analytical model and trilinear flow model. Wang et al. [6] presented an analytical model for a MFHW in rectangular reservoirs by using the source function method and the principle of superposition. Ozkan et al. [8] utilized a trilinear flow model to study the MFHWs performance in unconventional reservoirs. Restricted by the models, neither analytical model nor trilinear flow model can simulate the SRV region accurately. For convenience of presentation and brevity, a relatively simple case which consists of a MFHW in a homogeneous rectangular reservoir is considered. By letting the properties of SRV and unstimulated region be equal, the model can be simplified. The calculated results are shown in Table 1 and plotted in Figure 4. From Figure 4 we can see that the results of semianalytical solution show a good fitting performance with the analytical solution for the same problem. The comparison between semianalytical

TABLE 1: Comparison between analytical, trilinear flow model and semianalytical model results.

t_D	Analytical model		Trilinear flow model		Semianalytical model	
	\bar{p}_{wD}	$dp_{wD}/d \ln t_D$	\bar{p}_{wD}	$dp_{wD}/d \ln t_D$	\bar{p}_{wD}	$dp_{wD}/d \ln t_D$
0.001	0.061	0.015	0.065	0.016	0.061	0.015
0.01	0.110	0.029	0.116	0.030	0.111	0.029
0.1	0.209	0.060	0.222	0.067	0.209	0.060
1	0.397	0.103	0.443	0.129	0.397	0.103
10	0.663	0.122	0.836	0.219	0.662	0.122
100	1.006	0.231	1.583	0.562	1.006	0.231
1000	2.787	1.982	4.407	2.328	2.787	1.981
10000	20.464	19.811	23.356	21.150	21.150	19.811
100000	197.184	198.075	212.037	211.506	197.185	198.075

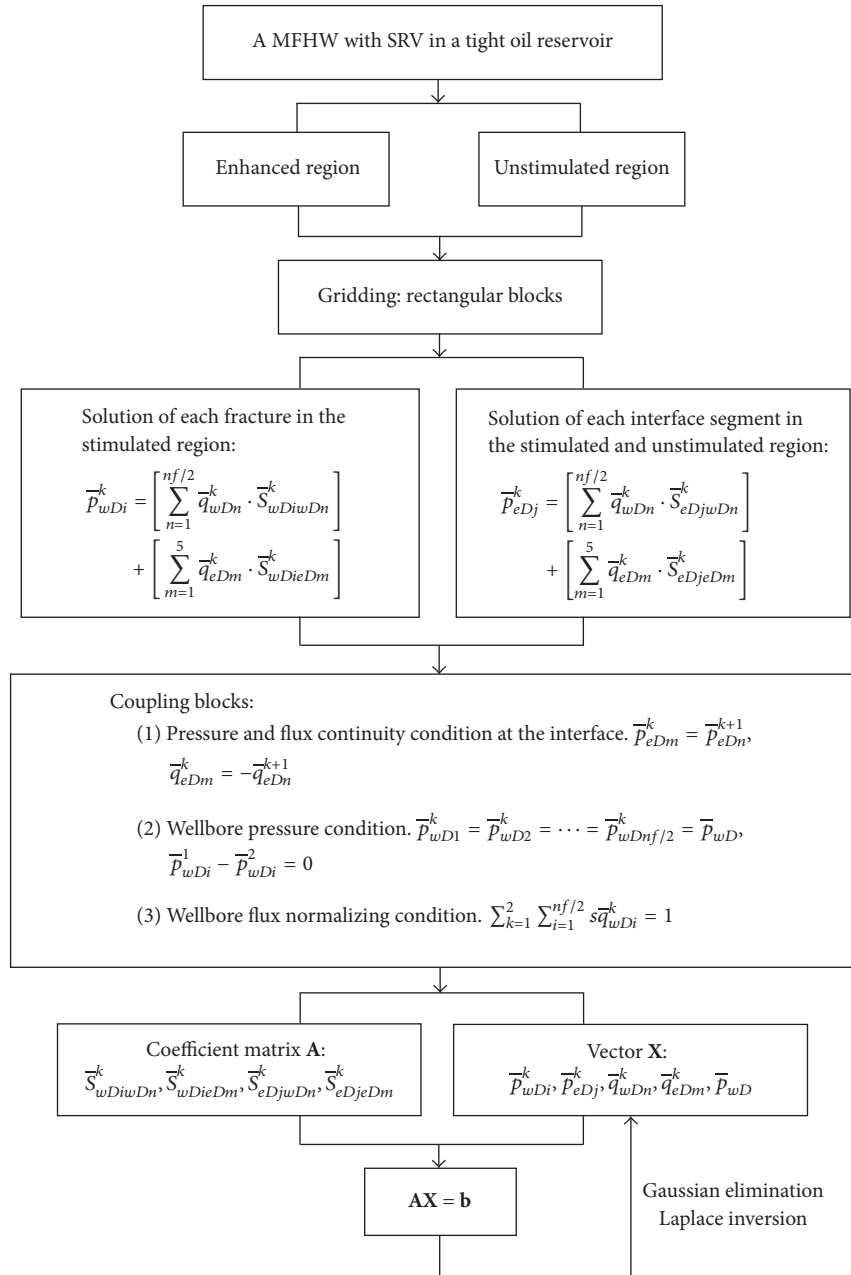


FIGURE 3: The work flow for modeling and solving process.

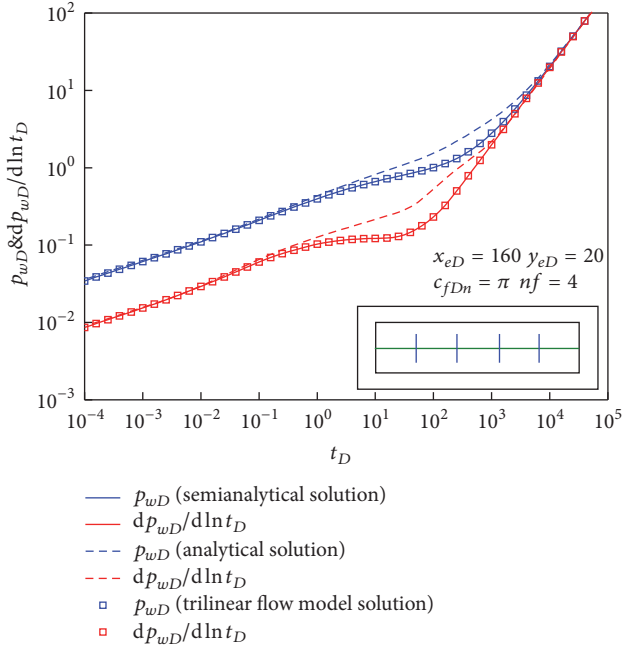


FIGURE 4: Calculation comparison between semianalytical model, analytical model, and trilinear flow model.

solution and trilinear flow model solution shows a good fitting performance in the early stage (linear flow). However, radial flow could not be seen by using trilinear flow model. MFHWs exhibit radial flow from beginning till the end which is usually misinterpreted as linear flow due to existence of linear flow as part of the radial flow. Thus, it is necessary to take nonlinear flow into account.

To access the accuracy of semianalytical model of MFHW with SRV in tight oil reservoir, a case is evaluated to investigate the pressure responses by using the commercial software Eclipse. The basic parameters are presented in Table 2. The reservoir block of $90 \times 21 \times 1$ is simulated with no flow boundaries. The enhanced region contains $44 \times 13 \times 1$ blocks which is shown in Figure 5. The horizontal well is located in center of reservoir horizontally and vertically to produce the oil effectively. Four hydraulic fractures are modeled with LGR technique to formulate thin blocks assigned with the properties of hydraulic fractures. Reservoir is fully penetrated by hydraulic fractures. Hydraulic fracture properties are assumed to be constant along the fracture. The flowing fluid is assumed to be single phase oil. Reservoir simulator is computed for 40 years of production with constant oil rate $30 \text{ m}^3/\text{D}$. The comparison results are shown in Figure 6. From the comparison results, it is shown that the agreements of the semianalytical solution and numerical solution are excellent.

4. Results and Discussion

4.1. Flow Regimes. The dimensionless pressure and pressure derivative type curves for a MFHW with SRV are plotted in Figure 7. As shown in Figure 7, seven flow stages can be identified.

TABLE 2: Input information for the case.

Reservoir lateral length (m)	933
Initial pressure (MPa)	20.29
Wellbore radius (m)	0.1
Reservoir compressibility (MPa^{-1})	0.02
Matrix porosity	0.125
Oil viscosity (mPa-s)	4
Fracture spacing (m)	59.25
Fracture half-length (m)	50
Fracture permeability (μm^2)	2.5
Enhanced region permeability (μm^2)	0.06
Unstimulated region permeability (μm^2)	0.01

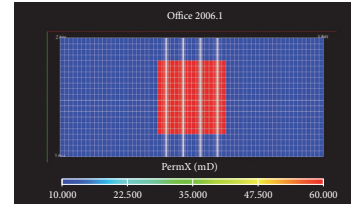


FIGURE 5: Numerical model of a multiple-fractured horizontal well with SRV.

(1) Bilinear flow between the hydraulic fractures and induced fractures: In this stage, the pressure derivative curve has a straight line with slope equal to $1/4$. Fluid flows through hydraulic fractures to wellbore and from induced fractures to hydraulic fractures simultaneously. This stage could be identified only if the fracture conductivity is relatively low.

(2) Linear flow near the hydraulic fractures: During this period, each fracture produces independently. The pressure and pressure derivative curves are both straight lines with slope equal to $1/2$.

(3) Interporosity flow between the induced fractures and matrix: In this stage, the fluid flows from the matrix system to the induced fractures system. The pressure derivative curves show “U” shape.

(4) Radial flow around the hydraulic fractures: If the pressure derivative curve shows the $1/2nf$ (nf is the number of fractures), the radial flow region will be observed. In this stage, radial flow occurs directly from the enhanced region to individual fractures.

(5) Transition flow near the enhanced region boundaries (Interporosity flow between the enhanced region and unstimulated region): In this region, the permeability of enhanced region is higher than that of the unstimulated region. The fluid in the enhanced region can reach the wellbore quickly; however, the formation in the unstimulated region can not provide enough fluid supply. The pressure derivative curves rise up which shows the similar characteristics of the weak supply or closed boundary flow.

(6) Mid-linear flow around the horizontal well: Compared to the transition flow, the slopes of both pressure and pressure derivative curves are relatively small. Fluid flows from the unstimulated region to the enhanced region.

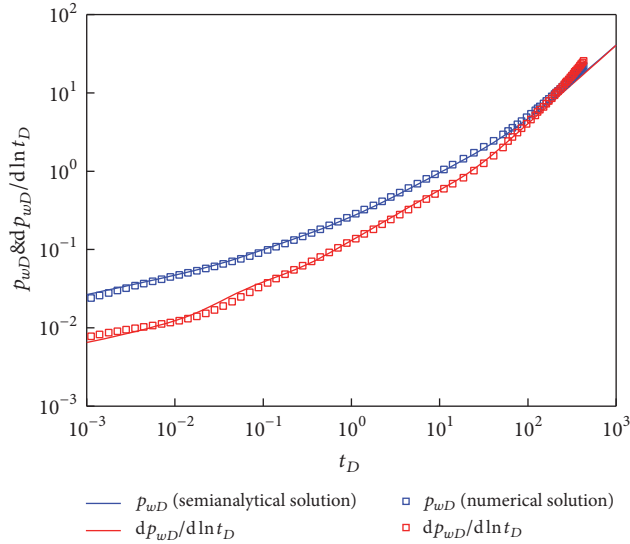


FIGURE 6: Calculation comparison between semianalytical model and numerical model.

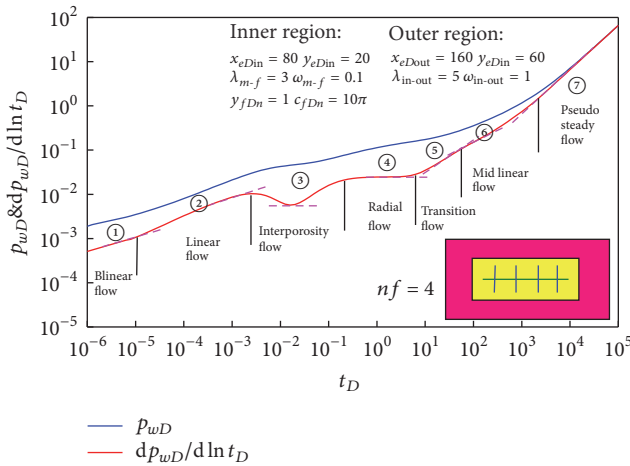


FIGURE 7: The dimensionless pressure and pressure derivative curves of a MFHW with SRV in a tight oil reservoir.

(7) Pseudo steady flow: The segment has a unit slope straight line on both pressure and pressure derivative curves. This flow period occurs when the pressure wave reaches the reservoir boundary.

4.2. Effect of Sensitive Parameters on Type Curves

4.2.1. Interporosity Flow Factor between the Inner and Outer Region (λ_{in-out}). Figure 8 shows the effect of interporosity flow factor between the inner and outer region λ_{in-out} on the type curves. λ_{in-out} is the mobility ratio between the inner and outer region. In Figure 8(a) we can see that the interporosity flow factor between the inner and outer region can affect all the flow regimes. With the increase of λ_{in-out} , the dimensionless pressure and pressure derivative decrease as a whole. It can be seen from the dimensionless pressure derivative curves that when the mobility between the inner

and outer region is the same ($\lambda_{in-out} = 1$) it will not create transition flow, but, instead, mid-linear flow. When the effect of hydraulic fracturing is good, the permeability of induced fractures system in the inner region is far higher than that of the formation in the outer region. The fluid in the inner region can reach the wellbore quickly; however, the formation in the outer region can not provide enough fluid supply. The pressure derivative curves rise up which shows the similar characteristics of the weak supply or closed boundary flow. The time of radial flow period in the region with higher mobility is shorter than that with lower mobility. It is known that radial flow can cause large pressure depletion under the same rate, and thus it is better to increase the scale of hydraulic fracturing as much as possible to improve the mobility of the inner region. Figures 8(b) and 8(c) show that the flux of fracture at the edge is higher than that at the center. This is because the fracture at the edge has a bigger drainage area. The time of transition flow in the region with higher mobility is shorter than that with lower mobility and the time of mid-linear flow in the region with higher mobility is longer than that with lower mobility. The larger the λ_{in-out} , the greater the differences between the flux of fracture at the edge and center and between the flux of different interfaces.

4.2.2. Hydraulic Fracturing Degree (Storage Ratio ω_{m-f} and Interporosity Flow Factor λ_{m-f}). Figure 9 shows that the storage ratio ω_{m-f} and interporosity flow factor λ_{m-f} affect the degree and time of interporosity flow between induced fractures system and matrix, respectively. Small ω_{m-f} means that the difference between the storage capacity of induced fractures system and matrix is great. Most of the fluid is stored in the matrix rather than the induced fractures system and the interporosity flow behaves more obviously. The dimensionless pressure derivative curve sinks down at the intermediate time. λ_{m-f} reflects the ability of the fluid to flow from the matrix to the induced fractures system. The larger the λ_{m-f} is, the earlier the interporosity flow will happen. Therefore, increasing the degree of hydraulic fracturing is beneficial to the production.

4.2.3. The Size and Shape of Stimulated Reservoir Volume. Figures 10-11 show the effects of size and shape of SRV on type curves. It can be seen from Figures 10-11 that both the size and shape of SRV will affect the radial flow and transition flow. A small size of SRV will shorten the time of radial flow and make transition flow occur early. Comparing with the three models presented in Figure 10(a), we can see that with the size of SRV increasing, the increasing trend of dimensionless pressure gradually slows down. This is mainly because the reserves controlled by a single well are very limited, and there is no sense in increasing the stimulated reservoir volume without limitation. At the same time, increasing the size of SRV will also increase the difficulty and cost of fracturing. From Figure 10(b) we can see that the larger the size of SRV, the greater the fracture flux difference between the edge and center. As shown in Figure 11, the dimensionless pressure with square shape of SRV is higher than that with rectangular one, which means that the square shape of SRV will cause a small pressure depletion under the same rate. In addition, with the

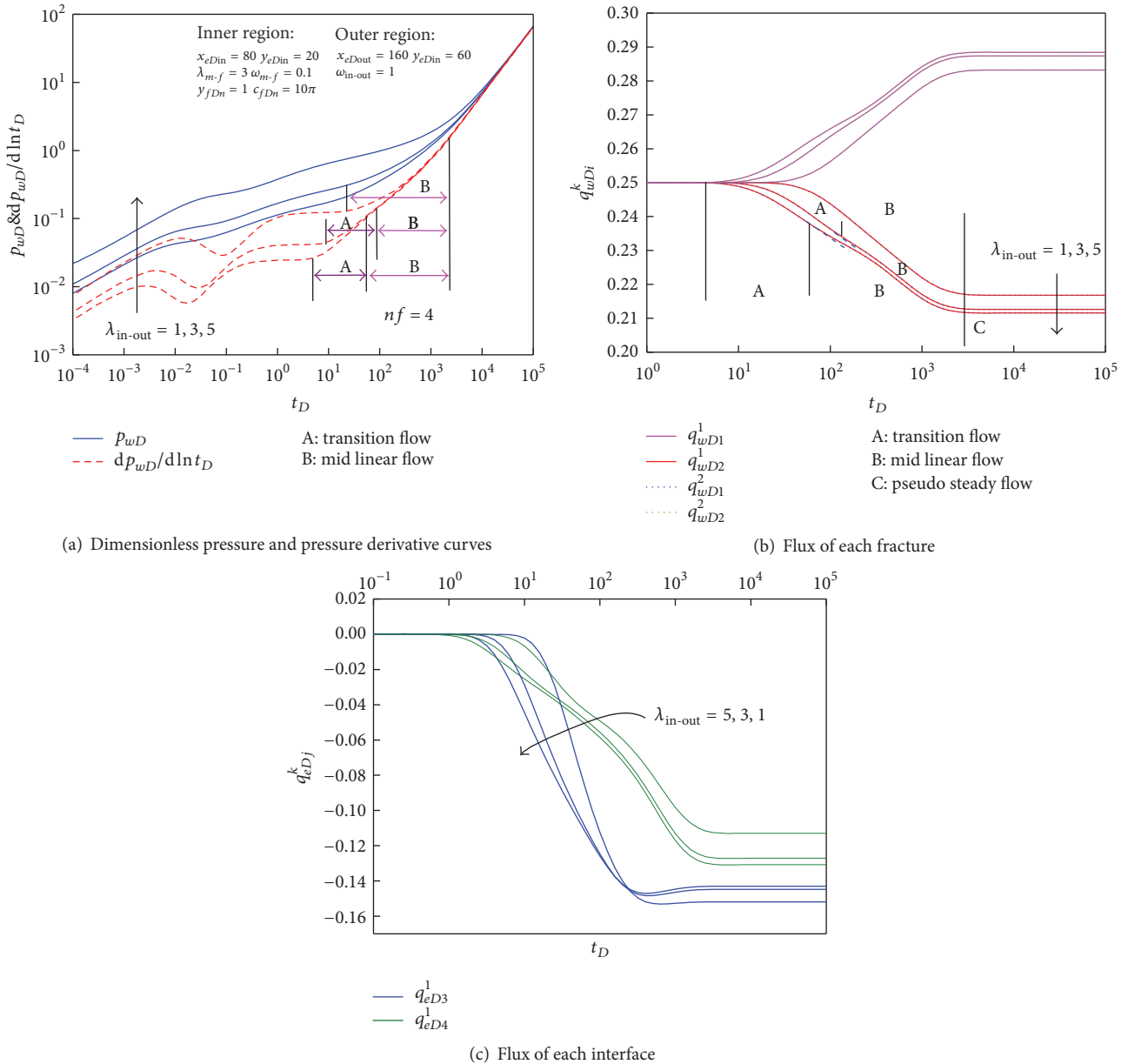


FIGURE 8: The effect of interporosity flow factor on type curves (inner and outer region).

increase of length-width ratio of SRV, both the dimensionless pressure and the fracture flux difference between the edge and center increase. It is because in the early period the flow only occurs in the hydraulic fractures and induced fractures near the horizontal wellbore which is not influenced by the shape of SRV. With the process of production, the pressure wave spreads to the edges of enhanced region, and the producing degree of formation with larger effective stimulated reservoir volume is much higher. Therefore, not only the size but also the shape of SRV should be taken into account in the fracturing design.

4.2.4. Fracture Distribution. Figure 12 shows the effect of fracture distribution on type curves. As shown in Figure 12, the fracture distribution can mainly affect the flow

characteristics of radial flow and transition flow. With the increase of fracture distribution heterogeneity, the pressure depletion becomes large. This is because the drainage area of each fracture is relatively small. If the fractures are very close to the enhanced region boundaries, second radial flow will occur once the pressure wave spreads to the nearest boundaries, and second transition flow will happen after the pressure wave spreads to the far boundaries. Therefore, it is necessary to make the hydraulic fractures distribute uniformly as far as possible.

4.2.5. Fracture Conductivity. Figure 13 shows the effect of fracture conductivity on type curves. From the pressure derivative curves we can see that the fracture conductivity mainly affects flow characteristics of bilinear flow, linear flow,

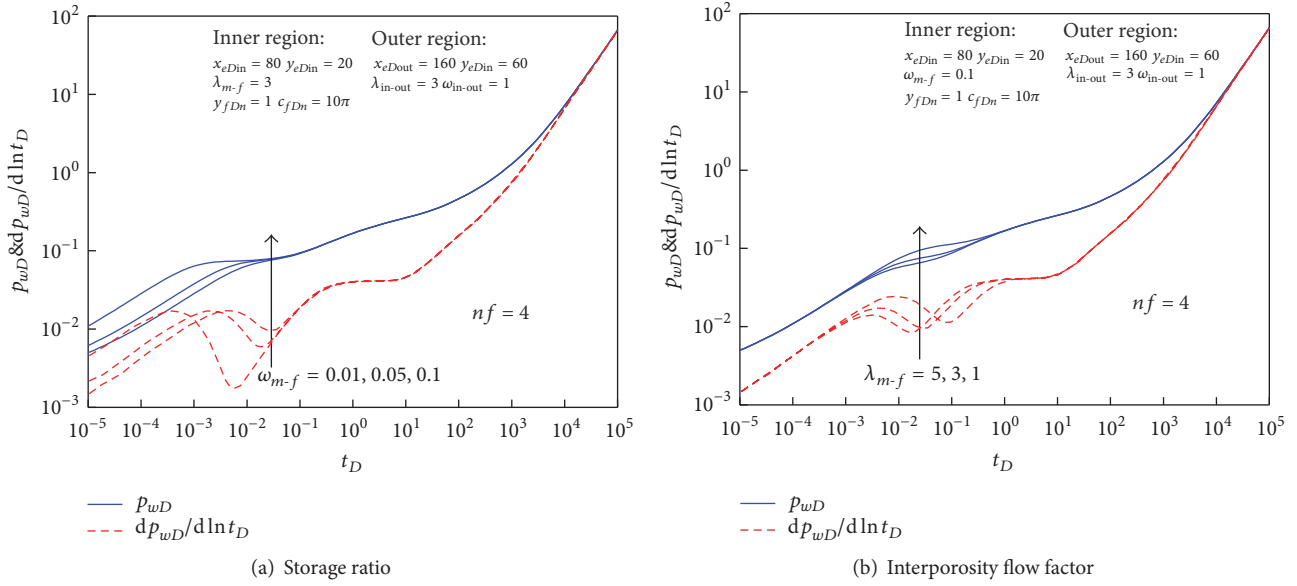


FIGURE 9: The effect of hydraulic fracturing degree on type curves.

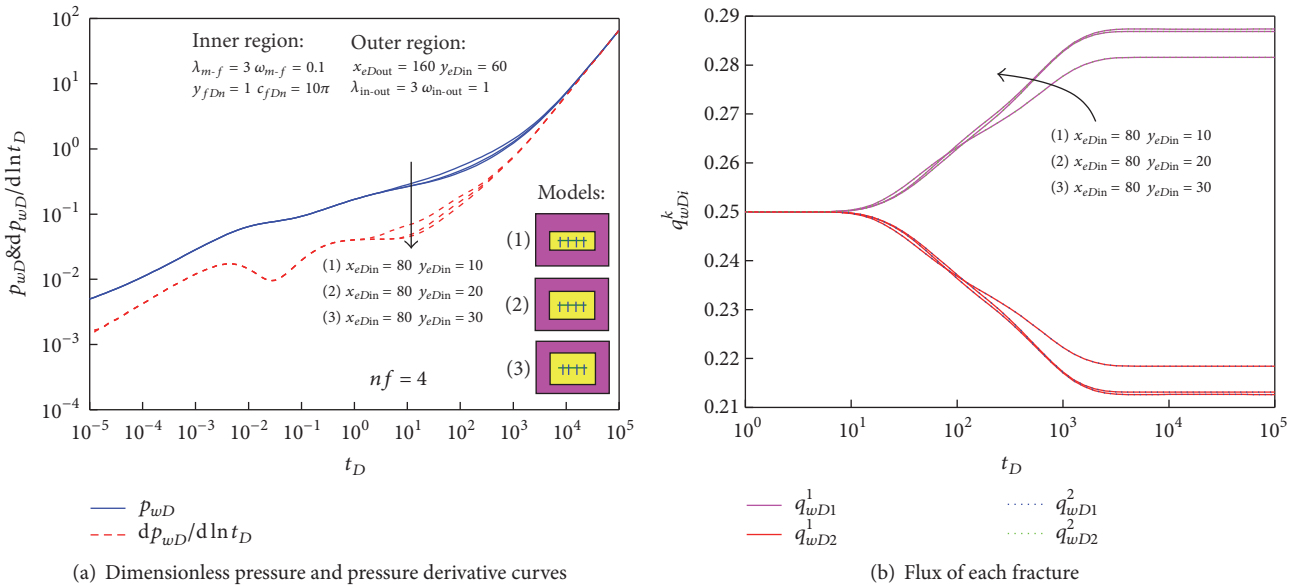


FIGURE 10: The effect of size of SRV on type curves.

and interporosity flow. Due to the high fracture conductivity, the pressure gradient near the hydraulic fracture is high. Fluid flows quickly from the induced fractures into the hydraulic fractures, which makes the linear flow and interporosity flow occur early.

4.2.6. Fracture Length. As shown in Figure 14, the fracture length can affect bilinear flow, linear flow, interporosity flow, and radial flow. With the increase of fracture length, the dimensionless pressure and pressure derivative decrease gradually. On the contrary to the conventional reservoirs, the effect of fracture length is greater than that of fracture

conductivity on the MFHWs with SRV in tight oil reservoirs. As the fracture length increases, more and more induced fractures in the enhanced region are connected with hydraulic fractures effectively, which can form a larger supply area and improve the overall yield. Longer fracture length will increase the time of interporosity flow and shorten the time of radial flow. In conventional fractured reservoirs, the fracture conductivity is dominant, whereas in volume fractured tight oil reservoirs the effect of fracture length is contrary to normal expectation. Therefore, in order to achieve the desired effect of volume fracturing design, a suitable length of the artificial hydraulic fractures should also be ensured.

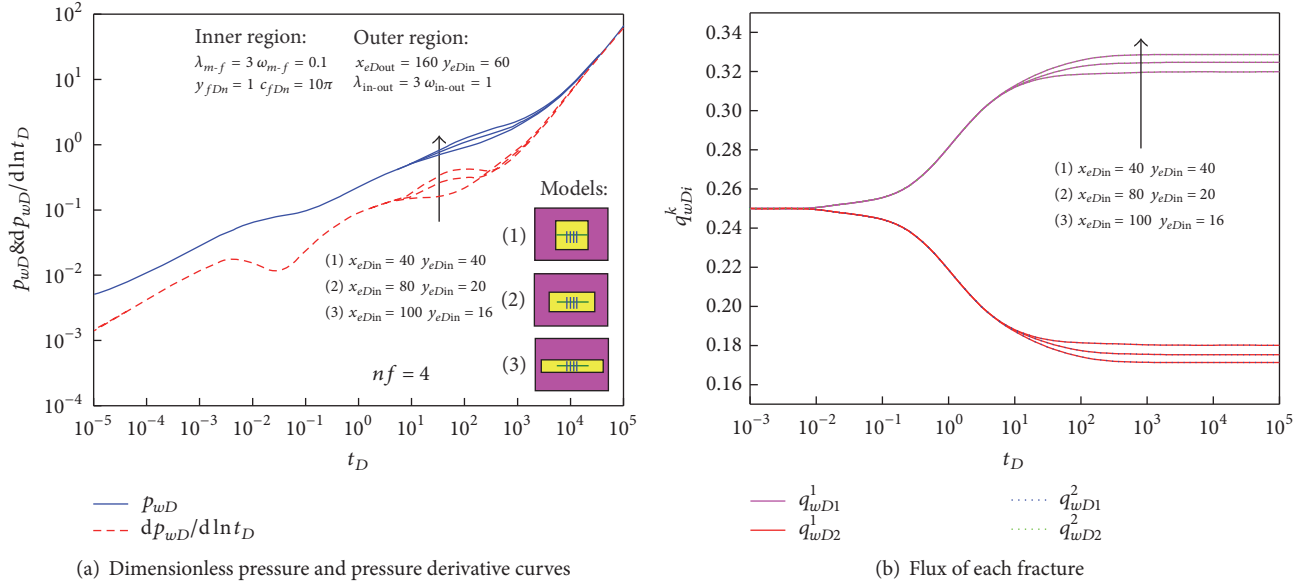


FIGURE 11: The effect of shape of SRV on type curves.

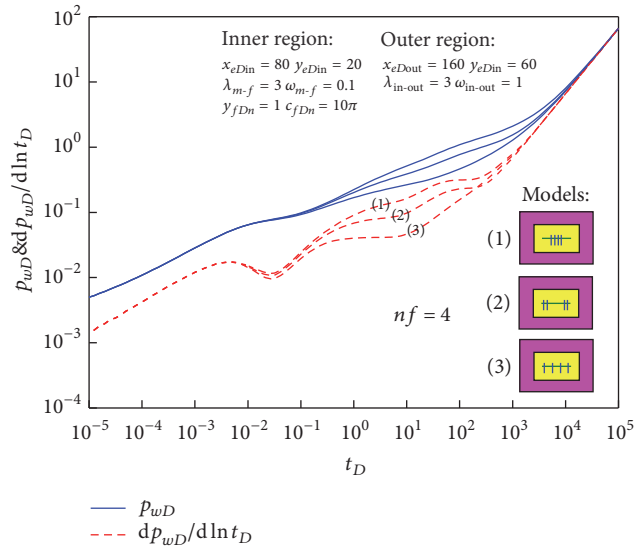


FIGURE 12: The effect of fracture distribution on type curves.

5. Field Applications

Type curve matching is an effective way to evaluate the parameters of reservoir and fracture. The specific processes are presented as follows.

Step 1. Plot the curve of dimensionless pressure (p_{wD}) values versus test time (t_D) on a log-log graph.

Step 2. Obtain the best match of the data with one of type curves.

Step 3. Read a point (e.g., t_D , p_{wD} , c_{fD}) from the matched type curve. By using the defined equations of dimensionless

parameter in (17)–(20), the reservoir and fracture parameters can be calculated.

$$k = \frac{1.842 \times 10^{-3} P_{wD} q \mu B}{(p_i - p_j) h}, \quad (17)$$

$$L_f = \sqrt{\frac{3.6kt}{\phi \mu c_f t_D}}, \quad (18)$$

$$k_f = \frac{k L_f c_{fD}}{w_f}, \quad (19)$$

$$\lambda_{in-outj} = \frac{(k/\mu)_j}{(k/\mu)_{ref}}. \quad (20)$$

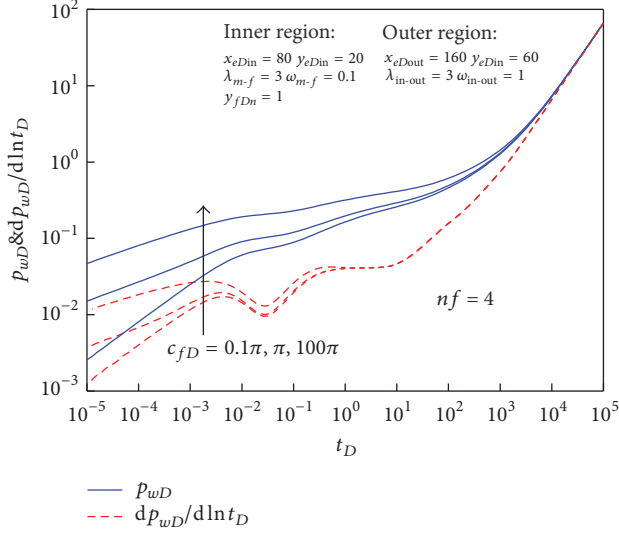


FIGURE 13: The effect of fracture conductivity on type curves.

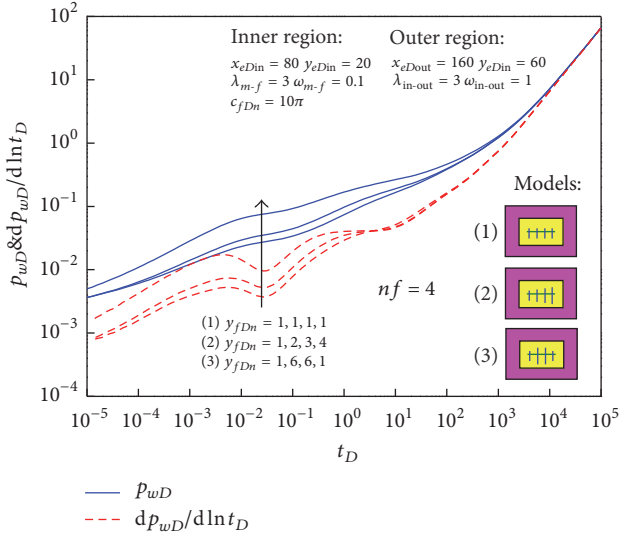


FIGURE 14: The effect of fracture length on type curves.

Well A is a horizontal well with 38 hydraulic fractures in Bakken formation in the Williston Basin. The length of well is approximately 2926.08 m. Since hydraulic fracturing methods with a high number of stages have not been widely used so far, the production history of well A is shorter than two years. The type curve matching plot is shown in Figure 15. From Figure 15 we can see that the pressure derivative curve starts to bend in the transition flow period; however, it could not be seen by using the traditional model without SRV. The calculation processes are presented as follows:

Reservoir Data

$$\phi \mu c_t = 9.80841 \times 10^{-2} \text{ mpa} \cdot \text{s/Mpa},$$

$$\frac{\mu B}{h} = 0.935369 \text{ mpa} \cdot \text{s/m},$$

$$t = 55 \text{ days},$$

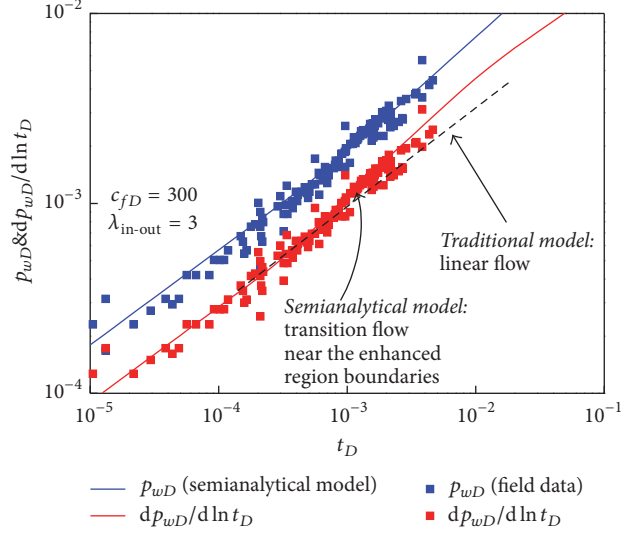


FIGURE 15: Type curve matching plot for field data.

$$w_f = 0.003 \text{ m},$$

$$\frac{P_i - P_w}{q} = 0.246036 \text{ Mpa} / (\text{m}^3 \cdot \text{day}^{-1}).$$

(21)

Match Point

$$t_D = 1.97459 \times 10^{-4},$$

$$P_wD = 6.71136 \times 10^{-4},$$

(22)

$$c_{fD} = 300.$$

Step 1. Calculate k_{in} (the permeability of enhanced region) from (17):

$$k_{in} = \frac{1.842 \times 10^{-3} \times 6.71136 \times 10^{-4} \times 0.935369}{0.246036}$$

(23)

$$= 0.0047 \times 10^{-3} \mu\text{m}^2.$$

Step 2. Calculate L_f (the half length of hydraulic fracture) from (18):

$$L_f = \sqrt{\frac{3.6 \times 0.0047 \times 10^{-3} \times 55 \times 24}{9.80841 \times 10^{-2} \times 1.97459 \times 10^{-4}}}$$

(24)

$$= 33.9587 \text{ m}.$$

Step 3. Calculate k_f (the permeability of hydraulic fracture) from (19):

$$k_f = \frac{0.0047 \times 10^{-3} \times 33.9587 \times 300}{0.003} = 15.9606 \mu\text{m}^2. \quad (25)$$

Step 4. Calculate k_{out} (the permeability of unstimulated region) from (20):

$$k_{out} = \frac{k_{in}}{\lambda_{in-out}} = \frac{0.0047 \times 10^{-3}}{3} = 0.0016 \times 10^{-3} \mu\text{m}^2. \quad (26)$$

- [8] E. Ozkan, M. Brown, R. Raghavan, and H. Kazemi, "Comparison of fractured horizontal-well performance in conventional and unconventional reservoirs," in *Proceedings of the SPE Western Regional Meeting*, pp. 345–360, Society of Petroleum Engineers, March 2009.
- [9] E. Ozkan, M. Brown, R. Raghavan, and H. Kazemi, "Comparison of fractured-horizontal-well performance in tight sand and shale reservoirs," *SPE Reservoir Evaluation and Engineering*, vol. 14, no. 2, pp. 248–259, 2011.
- [10] M. Brown, E. Ozkan, R. Raghavan, and H. Kazemi, "Practical solutions for pressure- transient responses of fractured horizontal wells in unconventional shale reservoirs," *SPE Res Eval & Eng*, vol. 14, no. 6, Article ID 125043, pp. 663–676, 2011.
- [11] E. Stalgorova and L. Mattar, "Practical analytical model to simulate production of horizontal wells with branch fractures," in *Proceedings of the SPE Canadian Unconventional Resources Conference*, Calgary, Canada, November 2012.
- [12] C. J. Guo, J. Zeng, X. Z. Wang, and F. H. Zeng, "Analytical model for multifractured horizontal wells in heterogeneous shale reservoirs," in *Proceedings of the Presented at the SPE Asia Pacific Oil & Gas Conference and Exhibition*, SPE-182422-MS, Perth, Australia, 2016.
- [13] S. P. Ketineni and T. Ertekin, "Analysis of production decline characteristics of a multistage hydraulically fractured horizontal well in a naturally fractured reservoir," in *Proceedings of the SPE Eastern Regional Meeting*, Society of Petroleum Engineers, Lexington, Ky, USA, October 2012.
- [14] Y.-L. Zhao, L.-H. Zhang, J.-X. Luo, and B.-N. Zhang, "Performance of fractured horizontal well with stimulated reservoir volume in unconventional gas reservoir," *Journal of Hydrology*, vol. 512, pp. 447–456, 2014.
- [15] O. Ozcan, H. Sarak, E. Ozkan, and R. Raghavan, "A trilinear flow model for a fractured horizontal well in a fractal unconventional reservoir," in *Proceedings of the SPE Annual Technical Conference and Exhibition (ATCE '14)*, SPE-170971-MS, pp. 5180–5198, October 2014.
- [16] H.-T. Wang, "Performance of multiple fractured horizontal wells in shale gas reservoirs with consideration of multiple mechanisms," *Journal of Hydrology*, vol. 510, pp. 299–312, 2014.
- [17] V. Sesetty and A. Ghassemi, "A numerical study of sequential and simultaneous hydraulic fracturing in single and multi-lateral horizontal wells," *Journal of Petroleum Science and Engineering*, vol. 132, pp. 65–76, 2015.
- [18] J. Warren and P. Root, "The behavior of naturally fractured reservoirs," *SPE Journal*, vol. 3, no. 3, pp. 245–255, 2013.
- [19] A. A. Daneshy, "Off-balance growth: a new concept in hydraulic fracturing," *Journal of Petroleum Technology*, vol. 55, no. 4, pp. 78–85, 2003.
- [20] E. Ozkan and R. Raghavan, "New solutions for well-test-analysis problems. Part 2. Computational considerations and applications," *SPE Formation Evaluation*, vol. 6, no. 3, pp. 369–378, 1991.
- [21] M. F. Riley, "Analytical solutions for elliptical finite-conductivity fractures," in *Proceedings of the 66th Annual Technical Conference and E14*, Paper SPE 22656, pp. 31–36, Dallas, Tex, USA, 1991.
- [22] L. Chu, P. Ye., I. S. Harmawan, L. Du, and L. R. Shepard, *Characterizing and Simulating The Nonstationariness and Nonlinearity in Unconventional Oil Reservoirs: Bakken Application/SPE Canadian Unconventional Resources Conference*, Society of Petroleum Engineers, 2012.